Eindhoven University of Technology

Eindhoven University of Technology

MASTER

Passive components for a GaN based high-power amplifier

van Straaten, B.C.L.

Award date:
2000

Link to publication

TU/e technische universiteit eindhoven Faculty of Electrical Engineering

Passive components for a GaN based high-power amplifier

by

Bram van Straaten

August 1999 - August 2000

This research is part of the GaN project at the Eindhoven University of Technology.
This project is performed in co-operation with the MMIC group at TNO-FEL at The Hague.

Supervisors: ir. B. Jacobs
prof. dr. ing. L.M.F. Kaufmann
dr. F. Karouta

Place : August 1999 – April 2000 and July 200 – August 2000
Eindhoven University of Technology
Faculty of Electrical Engineering
Telecommunication Technology and Electromagnetism
Opto-Electronic Devices group

April 2000 – July 2000
TNO-FEL
MMIC group

Acknowledgements

Summary

The characterisation of passive components for a monolithic high-power amplifier (HPA) based on gallium nitride (GaN) high electron-mobility transistors (HEMT) was the subject of this master thesis. This work was partially carried out at the Eindhoven University of technology (TU/e) and partially at the monolithic microwave integrated circuit (MMIC) group of TNO-FEL, The Hague. This work was part of the GaN research conducted at the TU/e, which focuses on the processing of GaN HEMTs and on an investigation into the possibilities of a monolithic, GaN HPA.

The work presented in this report will focus on the passive components required for a GaN based HPA. Although GaN can be grown on GaN, silicon carbide (SiC) and sapphire are the more common substrates. A monolithic solution based on SiC and a hybrid solution based on either aluminium nitride (AlN) or sapphire should be supported by this work. This means that the common microstrip design has to be replaced by a coplanar waveguide design, due to the fact that no via hole process is available for all three substrates. Since models for coplanar structure are not available for common circuit simulators, they should be created based on measurements or simulations.

The main obstacle to be overcome in case the models are to based on measurements is the fact that a set of contact pads needs to be added to the structure under test. These contact pads should not be included in the extracted model. The removal of the pads is called de-embedding. The measurements are performed using scattering parameters, which are normalised to the impedance of the measurement system. After de-embedding the scattering parameters of the structure under test are normalised to the characteristic impedance of the unknown transmission line connecting this structure to the pads. Hence, the behaviour of the pads and transmission line is not fully known and additional measurements are necessary. A capacitance measurement on the transmission line provides the remaining information for complete de-embedding.

A maskset was designed which contains all structures required for the extraction of a scalable model for the coplanar waveguide and the de-embedding of these transmission lines. Three numerical methods have been implemented, which are able to extract the pad structure using two lines with different lengths. These methods also allow direct extraction of the propagation constant. Finally, the characteristic impedance of the transmission line is obtained using the propagation constant and the capacitance measurement.

The measurements show distortion at the higher frequencies for laterally large structures. It has been verified that this distortion is not caused by probing or flawed calibration, but is related to parallel plate modes, which become dominant if the lateral dimensions become large compared to the substrate thickness. To verify the relation of this distortion to the substrate thickness a series of tests were performed which confirmed the expected behaviour.

The extracted propagation constants are shown to agree well with conformal mapping algorithms and a commercial transmission line calculator. The measured capacitance shows acceptable agreement with two conformal mapping algorithms, which implies that the experimental measurement set-up can be used to estimate the transmission line capacitance.

To be able to assess the possibility of model extraction based on simulations a series of simulations was run using three electromagnetic simulators. The simulators that were used are HP Momentum, Sonnet EM Suite and HP high-frequency structure simulator (HFSS). Due to the limited amount of time that was spent using the three simulators, no conclusive results could be obtained. The preliminary results obtained with both HP Momentum and Sonnet indicate, that these simulators have difficulties reproducing the measurements. HP HFSS has indicated the presence of higher-order parallel plate modes.

Contents

List of symbols

Symbol	relation	unit	Description
a_I		$V^{0.5}A^{0.5}$	incident travelling voltage wave at port I
b_I		$V^{0.5}A^{0.5}$	scattered travelling wave voltage at port I
ω	$2\pi f$	rad/s	angular frequency
f		Hz	frequency
μ_r	$\mu_r' \text{-} j\mu_r''$		complex relative permeability
ε_r	$\varepsilon_r' \text{-} j\varepsilon_r''$		complex relative permittivity
σ		S/m	conductivity
γ	$\alpha + j\beta$		complex propagation constant of a wave
α			attenuation constant of a wave
β			propagation constant of a wave
k_0	$\omega\sqrt{\mu_0 \varepsilon_0}$		complex free space propagation constant
δ	$\sqrt{\dfrac{2}{\omega\sigma\mu_0}}$	m	skin depth
E		V/m	electric field
H		A/m	magnetic field
Q			quality factor
S		m	distance between signal lead and ground plane
W		m	width of the signal lead
t		m	metalisation thickness
H		m	substrate thickness

List of constants

Symbol	value	unit	Description
ε_0	$8.854\ 10^{-12}$	F/m	permittivity of free space
ε_{rGaN}	9.9		relative permittivity of GaN
ε_{rAlN}	8.8		relative permittivity of AlN
μ_0	$4\pi\ 10^{-7}$	F/m	permeability of free space
μ_r	1.0		relative permeability of free space
σ_{AlN}	$<1\ 10^{-16}$	S/m	bulk conductivity of AlN
σ_{GaN}			bulk conductivity of GaN
σ_{gold}	$4.09\ 10^7$	S/m	bulk conductivity of gold
η_0	377	Ω	free space characteristic impedance

List of acronyms

ADS	Advanced Design System
AlN	Aluminium Nitride
BCL	Bram Capacitance Line
BCLe	Optimised BCL algorithm
BCLo	Original BCL algorithm
EM	Electromagnetic
GaAs	Gallium Arsenide
GaN	Gallium Nitride
HEMT	High Electron Mobility Transistor
HFSS	High-Frequency Structure Simulator
HMIC	Hybrid Microwave Integrated Circuit
HPA	High-Power Amplifier
HVPE	hydride vapour phase epitaxy
LRL	Line-Reflect-Line
LRLe	Optimised LRL algorithm
LRLo	Original LRL algorithm
NiCr	Nickel Chromium
MDS	Microwave Design System
MIM	Metal-Isolator-Metal
MMIC	Monolithic Microwave Integrated Circuit
SiC	Silicon Carbide
SiO_xN_y	Silicon Oxy-Nitride
S-Parameters	Scattering Parameters
TEM	Transverse Electromagnetic
TE	Transverse Electric
TM	Transverse Magnetic
TRL	Through-Reflect-Line
TSD	Through-Short-Delay
TSDe	Optimised TSD algorithm
TSDo	Original TSD algorithm
TU/e	Eindhoven university of Technology

1 Introduction

1.1 General introduction

This research is part of the Gallium Nitride (GaN) project at the Eindhoven University of Technology (TU/e). The GaN project focuses on the processing of GaN high electron mobility transistors (HEMT) and on the investigation into the possibilities for a monolithic, GaN based high-power amplifier (HPA) working at X-band frequencies. The GaN research at the TU/e is performed in co-operation with the monolithic microwave integrated circuits (MMIC) group at TNO-FEL in The Hague.

The work presented in this report will focus on the passive components required to realise a monolithic, GaN based high-power amplifier (HPA). Before the required components can be identified an approximate design for the HPA has to be determined. This design can be used to identify the passive components and provide and estimate of the constraints placed on these elements.

The past few years research towards wide bandgap materials, like GaN, aiming for high power and high frequency applications has increased dramatically. The reason for this interest becomes clear when some of the material properties are compared to the more main stream materials like Silicon and GaAs.

Table 1.1 Material properties of silicon, gallium arsenide and gallium nitride.

property	units	Silicon	GaAs	GaN
bandgap	eV	1.11	1.43	3.4
relative dielectric constant		11.8	12.8	9.0
breakdown field @ $N_d = 10^{17}$ cm^{-3}	V/cm	$6.0\ 10^5$	$6.5\ 10^5$	$3.5\ 10^6$
electron mobility @ $N_d = 10^{16}$ cm^{-3}	cm^{2}V^{-1}s^{-1}	1350	6000	1000
hole mobility @ $N_d = 10^{16}$ cm^{-3}	cm^{2}V^{-1}s^{-1}	450	330	300
saturated electron velocity	cms^{-1}	$1.0\ 10^7$	$1.0\ 10^7$	$1.5\ 10^7$
thermal conductivity	Wcm^{-1}K^{-1}	1.5	0.5	1.3

Wide bandgap materials will show better high voltage performance due to the higher breakdown field. This means that identical devices fabricated on GaN and GaAs can be operated at higher voltages for the GaN device increasing power potential for equal currents.

One problem that remains is heat-dissipation. GaN is grown on a sapphire or on a silicon carbide (SiC) substrate[1]. Although SiC has a better thermal conductivity it is much more expensive than sapphire.

It has been established that the heat-sinking capability of sapphire is insufficient for high-power operation. This problem can be overcome by using a flip-chip technique that connects the GaN active elements to a carrier substrate that is capable of sinking the heat generated by these active elements. In case a monolithic solution is required SiC substrates should be used. The research in this work will enable both possibilities, which means that any passive component supports both a hybrid flip-chip solution on a host substrate and a monolithic solution on a SiC substrate.

---

[1] We will not consider hydride vapour phase epitaxy (HVPE) substrates, as these are not yet readily available.

Often MMICs are based on microstrip transmission lines, figure 1.1 shows a microstrip line.
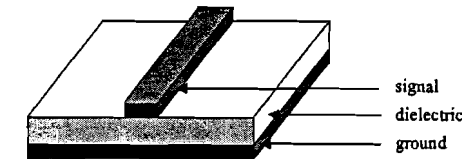
Figure 1.1 Layout of a microstrip transmission line.

Microstrip circuits consist of tracks printed on a dielectric slab, the substrate, which is covered with metal, which acts as a ground plane. Microstrip circuits require a via hole, a metallic connection through the substrate, to contact the ground plane from the top of the substrate.

In case a monolithic solution based on sapphire is pursued via holes are not a viable option. For this reason coplanar waveguides, as illustrated below, will be used.
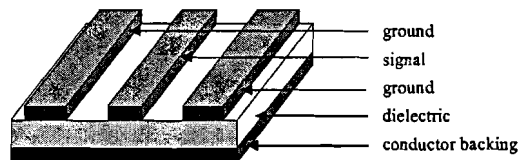
Figure 1.2 Layout of a conductor backed coplanar waveguide with finite ground planes.

Again the basis is a dielectric slab, however the conductor backing is not desired but rather an effect caused by the metal mounting likely to be used for the power amplifier. All signal tracks are printed on top of the substrate, the centre track carries the signal while the two outer tracks act as ground planes.

If coplanar waveguides are used, models will have to be extracted for the passive components. This will require an investigation into the possibilities of modelling passive components based on measurements and or simulations.

1.2 The objectives of this work

The aim of this research is to investigate the passive components required for realising a monolithic or hybrid HPA. This means that both passive and active elements need to be realised on the same substrate. Since no via holes can be etched into the sapphire substrate, a microstrip solution cannot be realised and the main effort should be placed on the development of a library of coplanar circuit element models.

These circuit element models can either be based on simulations or measurements. Each method has its specific advantages and disadvantages and a study needs to be performed into the possibilities of success using either one of these two methods.

This report has the following set of goals:

1. To provide an overview of the passive components required for the HPA MMIC
2. To investigate the possibility of a measurement based approach for the modelling of passive components
3. To investigate the possibility of a simulation based approach for the modelling of passive components
4. To characterise a set of coplanar waveguide transmission lines
5. To assess the possibilities for realising a high-power amplifier based on coplanar waveguide elements

1.3 The structure of this report

Chapter two introduces some general transmission line theory leading to a comparison of the coplanar waveguide and the microstrip transmission line. Finally several modes supported by coplanar waveguides are briefly reviewed.

Chapter three introduces a possible equivalent circuit of a power amplifier based on GaN HEMTs resulting in an approximate solution for the required matching networks. After this a brief overview of the most commonly used passive components is presented, leading to a choice concerning the final amplifier layout.

Chapter four presents the problems that can be expected in case a measurement-based approach is used. The chapter concludes by introducing the set of masks, which can be used for the characterisation of coplanar waveguide structures. After the measurement related problems have been identified solutions are proposed. Where possible several alternative solutions are implemented and the best solution is identified.

Chapter five presents the results of the measurements that have been performed on samples fabricated using the masks from chapter four. Where possible the results of the measurements will be explained using the conformal mapping technique described in chapter three. For the cases where problems were expected additional measurements will be used to verify the expected problem sources.

Chapter six starts out with introducing the three simulators used to study the possibilities of a simulation based approach. Next the limitations of the simulators will be reviewed together with, where possible, work around approaches. The results of the simulations will be compared to the results obtained from the measurements presented in chapter five.

Finally chapter seven presents a brief review, introducing some general conclusions with respect to the goals of this report and some recommendations for future work.

2 Transmission line theory

2.1 Introduction

As mentioned in the general introduction, the goal of the GaN project is to demonstrate an X-band HPA. This means that it will operate at frequencies ranging from 8 up to 12 GHz. At these frequencies special attention has to be paid to the interconnections which are used to connect active and passive components. At microwave frequencies, these interconnects are called transmission lines.

This chapter will start by introducing some general theory with respect to these types of transmission lines in section 2. A large amount of literature is available with respect to transmission line theory [37-41]. For this reason this section will be limited to the most essential theory and some especially interesting items.

Section 3 will take a closer look into two commonly used transmission lines, i.e. microstrip and coplanar waveguides. The advantages and disadvantages of the two types of transmission lines will be compared.

Finally, section 4 will discuss the electromagnetic modes that can propagate through a coplanar waveguide.

2.2 Lumped element transmission line model

The main difference between transmission line theory and common circuit theory is formed by the electrical length of the interconnect under consideration. As mentioned earlier, circuit theory assumes an instantaneous connection between both ends of a transmission line. This point of view is valid as long as the physical length of the transmission line is much smaller than the electrical wavelength. At microwave frequencies this assumption no longer holds, which means that voltage and currents are no longer constant but vary in phase and magnitude along the line.

Transmission line theory uses a distributed parameter network to describe transmission lines. This means that a transmission line is divided into an infinite number of sections of length Δz, as presented below. In this case the length of any section is a fraction of the electrical wavelength and a lumped-element equivalent circuit can be used to describe the behaviour of the single section.
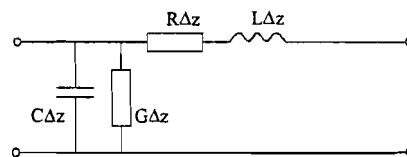
Figure 2.1 Equivalent circuit of a transmission line section.

The elements of the equivalent circuit are defined per unit length:

$R\ [\Omega m^{-1}]$ series resistance per unit length, for both conductors.
$L\ [Hm^{-1}]$ series inductance per unit length, for both conductors.
$G\ [Sm^{-1}]$ shunt conductance per unit length.
$C\ [Fm^{-1}]$ shunt capacitance per unit length.

The inductance represents the total inductance of the two wires, while the capacitance represents the coupling between the two wires. The series resistance models the finite conductivity of the wires while the conductance models the losses in the dielectric, which is used to separate the two wires.

2.2.1 Wave propagation and characteristic impedance

In case Kirchhoff's voltage and current laws are applied to the equivalent circuit of the transmission line, and a sinusoidal steady-state condition is assumed, the so-called telegrapher equations are obtained [41].

$$\frac{dV(z)}{dz} = -(R + j\omega L)I(z) \tag{2.1}$$

$$\frac{dI(z)}{dz} = -(G + j\omega C)V(z) \tag{2.2}$$

Combining [2.1] and [2.2] gives travelling wave equations, which describe the voltage and current phasors along the length of the transmission line:

$$\frac{d^2V(z)}{dz^2} - \gamma^2 V(z) = 0 \tag{2.3}$$

$$\frac{d^2I(z)}{dz^2} - \gamma^2 I(z) = 0 \tag{2.4}$$

Where γ is called the complex propagation constant, which is made up of a real part that describes the attenuation of the wave along the line and an imaginary part, which describes the propagation along the line:

$$\gamma = \alpha + j\beta = \sqrt{(j\omega L + R)(j\omega C + G)} \tag{2.5}$$

These equations result in the definition of the following travelling wave solutions:

$$V(z) = V_0^+ e^{-\gamma z} + V_0^- e^{\gamma z} \tag{2.6}$$

$$I(z) = I_0^+ e^{-\gamma z} + I_0^- e^{\gamma z} \tag{2.7}$$

Where the term with $e^{-\gamma z}$ represent the wave travelling in the +z direction and the term with $e^{\gamma z}$ represents the wave travelling in the –z direction.

Combining equations [2.1], [2.5] and [2.6] results in expressions which can be used to define a characteristic impedance for the transmission line.

$$Z_0 = \sqrt{\frac{(j\omega L + R)}{(j\omega C + G)}} \tag{2.8}$$

Which relates the currents and voltages on the transmission line according to:

$$Z_0 = \frac{V_0^+}{I_0^+} = -\frac{V_0^-}{I_0^-} \tag{2.9}$$

The propagation constant and characteristic impedance can describe the properties of the transmission line, and unlike lumped-element equivalent circuits, these properties are able to describe lines, which are long compared to the electrical wavelength.

2.2.2 Terminating a transmission line

A picture showing the position of the voltage and current phasors, used to describe the behaviour of a terminated transmission line with characteristic impedance Z_0 is presented below:
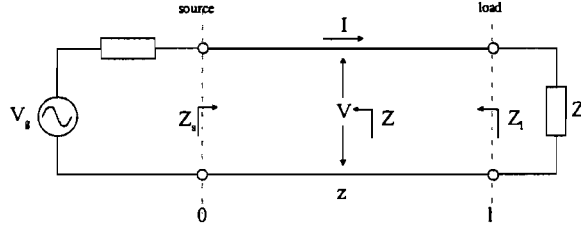
Figure 2.2 Definition of the notations for the terminated transmission line.

The transmission line contains both incident waves from the source and reflected waves caused by a non-ideal matched load, the voltage and current caused by these two voltage waves can be represented by:

$$V = V_{incident} + V_{reflected} = V_0^+ e^{-\gamma z} + V_0^- e^{\gamma z} \qquad [2.10]$$

$$I = I_{incident} + I_{reflected} = \frac{1}{Z_o}\left(V_0^+ e^{-\gamma z} - V_0^- e^{\gamma z}\right) \qquad [2.11]$$

At the load V_0^+ and V_0^- are given by:

$$V_0^+ = \tfrac{1}{2}I_1\left(Z_1 + Z_0\right)e^{\gamma l} \qquad [2.12]$$

$$V_0^- = \tfrac{1}{2}I_1\left(Z_1 - Z_0\right)e^{-\gamma l} \qquad [2.13]$$

Which in turn can be used to express the impedance of a transmission line at a random point z along the line, as the ratio between the voltage and current phasor at that point.

$$Z(z) = \frac{V(z)}{I(z)} = Z_0 \frac{Z_1 + Z_0 \tanh(\gamma d)}{Z_0 + Z_1 \tanh(\gamma d)} \qquad [2.14]$$

Where d equals the distance from the load. Due to the fact that the propagation constant varies with frequency the impedance that is seen on a certain position of the transmission line will also vary with frequency. Next the reflection coefficient and transmission coefficient are defined.

$$\Gamma = \frac{V_{reflected}}{V_{incident}} = \frac{Z_1 - Z_0}{Z_1 + Z_0} \qquad [2.15]$$

$$T = \frac{V_{transmitted}}{V_{incident}} = \frac{2Z_1}{Z_1 + Z_0} \qquad [2.16]$$

Where $V_{transmitted}$ can be obtained by rewriting equations [2.12] and [2.13].

$$V_0^+ e^{-\gamma l} + V_0^- e^{\gamma l} = V_{transmitted}e^{-\gamma l} \qquad [2.17]$$

$$V_0^+ e^{-\gamma l} - V_0^- e^{\gamma l} = \frac{Z_0}{Z_1}V_{transmitted}e^{-\gamma l} \qquad [2.18]$$

2.2.3   Relation between scattering parameters and transmission line parameters

All measurements performed on the transmission lines will be performed using scattering parameters. For this reason the relation between the transmission line parameters and the scattering parameters is presented. For readers, which are unfamiliar with S-parameters a short description can be found in appendix A.
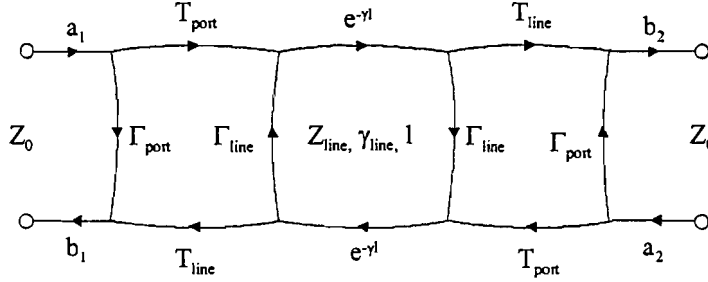
Figure 2.3 Definition of the notations for the transmission line inserted between two measurement ports.

It can be observed that the entire set-up is symmetric which means that S_{11} will equal S_{22} and S_{12} will equal S_{21}. For this same reason only two sets of reflection and transmission coefficients have to be determined. The first set, Γ_{port} and T_{port}, describes the reflection and transmission for waves travelling from the port into the transmission line while the second set, Γ_{line} and T_{line}, describes the reflection and transmission for waves travelling in the opposite direction.

$$\Gamma_{port} = \frac{Z_{line} - Z_0}{Z_{line} + Z_0} \qquad\qquad [2.19]$$

$$T_{port} = \frac{2Z_{line}}{Z_{line} + Z_0} \qquad\qquad [2.20]$$

$$\Gamma_{line} = -\frac{Z_{line} - Z_0}{Z_{line} + Z_0} \qquad\qquad [2.21]$$

$$T_{line} = \frac{2Z_0}{Z_{line} + Z_0} \qquad\qquad [2.22]$$

The relation between the transmission line parameters and the scattering parameters now follows from the definitions of the individual scattering parameters as presented below:

$$S_{11} = \left.\frac{V_1^-}{V_1^+}\right|_{V_2^+=0} = \Gamma_{port} + \frac{T_{port}T_{line}\Gamma_{line}e^{-2\gamma l}}{1 - \Gamma_{line}^2 e^{-2\gamma l}} \qquad\qquad [2.23]$$

$$S_{12} = \left.\frac{V_2^-}{V_1^+}\right|_{V_2^+=0} = \frac{T_{line}T_{port}e^{-\gamma l}}{1 - \Gamma_{line}^2 e^{-2\gamma l}} \qquad\qquad [2.24]$$

Where V_1 and V_2 are voltage waves travelling towards and from port 1 and port 2. These equations can be obtained by writing out the path followed by the incident wave a_1. For the reflection coefficient S_{11}, this results in a direct reflection Γ_{port} followed by a series of reflections in a loop formed by the transmission line. Any part of the wave that flows out of the transmission line at port 2 is lost while any part flowing out of the transmission line at port 1 is added to the total reflected wave. Each loop through the transmission line adds a phase shift of $e^{-2\gamma l}$ to the reflected wave at that point.

The reflection coefficient S_{11} can be obtained using an alternative approach, based on [2.15], since the reflection coefficient S_{11} equals Γ_{port} when the impedance from [2.14] is taken as load impedance.

If expressions [2.23] and [2.24] are used to plot the behaviour of a fictional transmission line as a function of frequency the plots presented below can be obtained:

Reflection
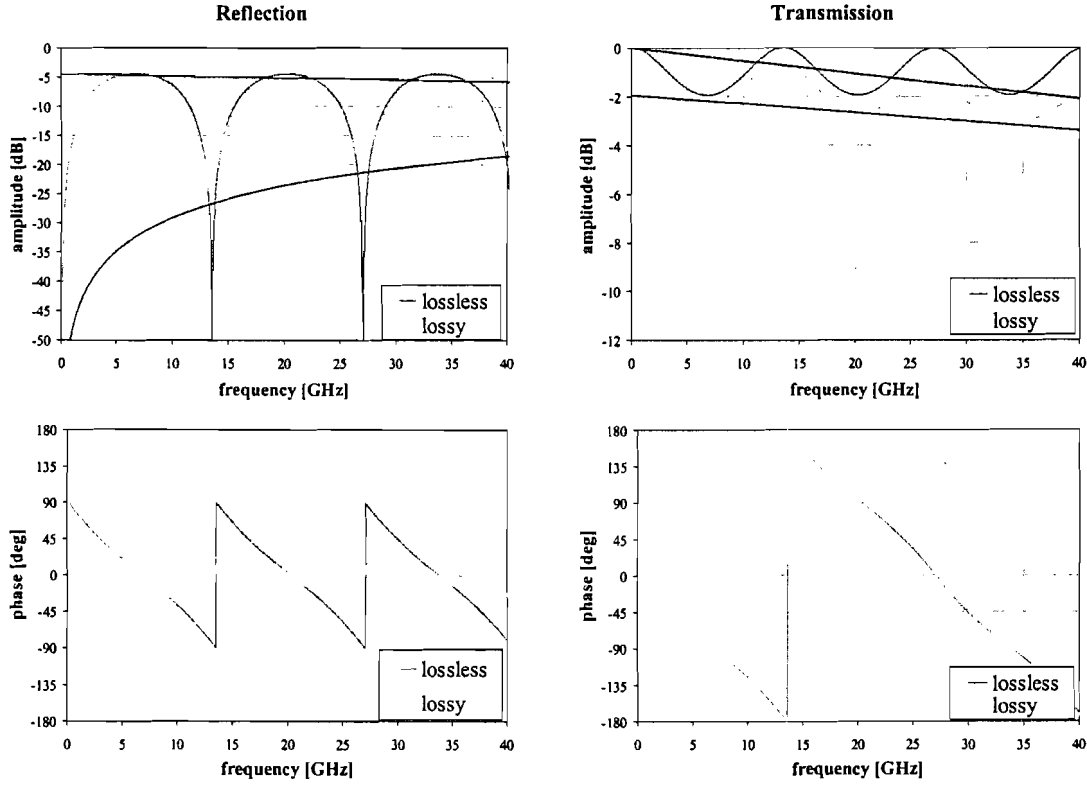
Transmission

Figure 2.4 Transmission and reflection of a lossless and a lossy transmission line.

This transmission line used for this example has characteristic impedance of 100 Ω and a length of 5 mm. The lossless transmission line has a propagation constant of 46.5 at 1 GHz, this is kept equal for the lossy line expect that an attenuation was added, which increases linear with frequency from 0 up to 50.

The ideal curves show the behaviour, including periodicity, which follows directly from the formulas presented on the previous page. The differences that are introduced by the losses will be discussed briefly. The first difference is that the amplitude of the reflection coefficient decreases, the expressions below present information on the bounding envelope of the reflection coefficient, represented by the dotted lines:

$$S_{11max} = \Gamma_{port} + \frac{T_{port}T_{line}\Gamma_{line}e^{-2\alpha l}}{1 - \Gamma_{line}^2 e^{-2\alpha l}}$$ [2.25]

$$S_{11min} = \Gamma_{port} - \frac{T_{port}T_{line}\Gamma_{line}e^{-2\alpha l}}{1 + \Gamma_{line}^2 e^{-2\alpha l}}$$ [2.26]

Where $e^{-\alpha l}$ denotes the real, frequency dependent attenuation constant, causing a gradual fade with increasing frequency. Similar expression are found for the transmission coefficient as presented below:

$$S_{12max} = \frac{T_{line}T_{port}e^{-\alpha l}}{1 - \Gamma_{line}^2 e^{-2\alpha l}}$$ [2.27]

$$S_{12min} = -\frac{T_{line}T_{port}e^{-\alpha l}}{1 - \Gamma_{line}^2 e^{-2\alpha l}}$$ [2.28]

2.3 Two commonly used transmission lines

This section introduces the microstrip transmission line, which is often used to design MMICs, and the coplanar waveguides, which will be used due to the fact that microstrip circuits can not be produced on a sapphire substrate. To gain more insight into the advantages of using either microstrip transmission lines or coplanar waveguides a comparison is presented between the two types of transmission lines.

2.3.1 Microstrip

The microstrip transmission line is the most commonly used type of transmission line. It consists of a metal plane on the bottom of the substrate, which acts as ground plane, and a single track on top, which acts as signal lead. A schematic representation of a microstrip transmission line is presented in the picture below:
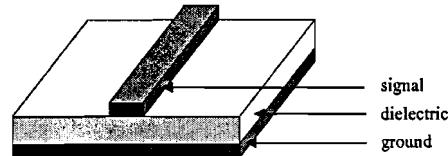
Figure 2.5 Layout of a microstrip transmission line.

The characteristic impedance of a microstrip transmission line is determined by the ratio of the track width over the substrate thickness. Since the substrate thickness is fixed the characteristic impedance and the track width are directly related. This means that downscaling of the circuit is limited by the substrate thickness.

2.3.2 Coplanar waveguide

A schematic representation of a coplanar waveguide is presented below. The three tracks on top of the substrate form a ground-signal-ground system, which means that the ground plane is accessible on top of the substrate. In practical situations a metal plane will be located beneath the substrate. This situation is called a conductor backed coplanar waveguide.
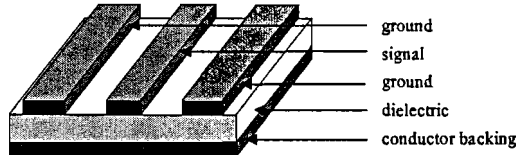
Figure 2.6 Layout of a conductor backed coplanar waveguide with finite ground planes.

The characteristic impedance of a coplanar waveguide with infinite ground and substrate thickness is presented below [40]. Elliptic integrals are included in MATLAB eliminating the need for approximations:

$$Z_0 = \frac{30\pi}{\sqrt{\varepsilon_{eff}}} \frac{K\left(\sqrt{1-k^2}\right)}{K(k)}$$

[2.29]

$$\varepsilon_{eff} = \frac{\varepsilon_r + 1}{2}$$

[2.30]

$$k = \frac{W}{W + 2S}$$

[2.31]

This means that the circuit scaling is only limited by the losses in the metal and the limits posed by the lithography used. The characteristic impedance increases with a decreasing spacing and for increasing width.

2.3.3 Coplanar waveguide versus microstrip

This section compares microstrip transmission lines with coplanar waveguide transmission lines [3]. Finally a conclusion is drawn about which solution should be chosen.

Advantages of coplanar waveguides compared to microstrip:

- No backside metalisation is required, which increases process yield and reduces processing costs.
- CPW allows smaller designs at high frequencies due to the fact that the characteristic impedance scales with width over ground-to-ground spacing instead of width over substrate thickness.
- Shunt elements suffer less parasitics, microstrip shunt elements require via holes.
- Less dispersion, which in term should yield better broad band performance.
- Ground planes act as shield, thus reducing the coupling between adjacent lines.
- Ground planes can be contacted at the top of the chip, which is convenient for flip-chip.
- Via hole etching is not supported for sapphire substrates, since coplanar waveguides do not require via holes, a monolithic GaN HPAs should be based on the coplanar waveguide solution.

Disadvantages of coplanar waveguides compared to microstrip:

- Lower effective dielectric constant, this results in slightly larger distributed elements.
- Higher losses, coplanar waveguides show higher losses than microstrip transmission lines with a comparable geometry
- Higher loss, coplanar waveguide lines show slightly higher loss than microstrip lines with the same lateral dimensions.
- Slotline mode, the coplanar waveguide can just as easily carry the coplanar mode as a slotline mode, this effect can be overcome by using airbridges. See section 2.4.
- Parallel plate mode, if a backside metalisation is present, which is normally the case since the chips will be mounted in a metal casing, a parallel plate mode can be excited. See section 2.4.
- Quasi-TEM behaviour, the field in microstrip lines is substrate oriented while the field in coplanar waveguides is surface oriented, which means the TEM assumption is not valid.
- Coplanar waveguide elements are not supported by the common circuit simulators, which means that MMIC design is complicated since models need to be generated before a circuit can be designed.

This set of advantages and disadvantages of coplanar waveguides over microstrip transmission lines leads to the conclusion presented below:

Microstrip circuits require via holes to realise connections with the ground plane, in case sapphire is used no via hole processing is available. Essentially this indicates that any power amplifier based on GaN HEMTs fabricated on a sapphire substrate can not be based on microstrip transmission lines.

This in combination with the fact that a coplanar waveguide design can be used for both monolithic and hybrid amplifier designs, a coplanar waveguide based solution should be chosen.

However, coplanar waveguide elements are not supported by the common circuit simulators, this means that design is complicated since models need to be generated before a circuit can be designed. Therefore special attention has to be paid to how these models can be extracted from either measurement or simulation.

2.4 Modes supported by the coplanar waveguide

The coplanar waveguide supports a series of modes. This section will briefly discuss which modes can be supported. Due to the fact that propagation constants and characteristic impedance of these modes differ, mixing the modes will lead to signal distortion, which is undesired. For this reason the coplanar waveguide mode is regarded as the desired mode while all other modes are regarded as undesired.

Coplanar waveguide mode

As mentioned earlier the coplanar mode is the mode that is desired for the operation of the coplanar waveguide. The picture below presents a schematic representation of the E-field for the coplanar mode.
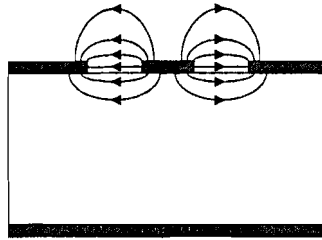
Figure 2.7 Schematic orientation of the E-field for a coplanar mode.

The transmission line theory in the previous section assumed a TEM-transmission line structure. The TEM assumption means that both the E-field and H-field are transverse to the direction of propagation.

$$E_z = H_z = 0 \qquad\qquad [2.32]$$

Due to the fact that the fields are substrate oriented the TEM assumption is inherently incorrect, since the propagation constant of the field through the air region is larger than the propagation constant of the fields travelling through the substrate. However, this effect remains small in case the dimensions of the coplanar waveguide remain moderate and a quasi-TEM description can be introduced [7].

Slotline mode

Another mode, which resembles the coplanar mode, is the slotline mode. In this case the voltage of one of the ground planes exceeds the voltage of the signal lead, and the field at this gap is inverted. Again a schematic representation of the E-field is presented below.

Figure 2.8 Schematic orientation of the E-field for a slotline mode.

The slotline mode is excited at discontinuities in the coplanar waveguide, for example corners. The slotline mode can be cancelled by tagging the two ground planes together at strategic points, for example at corners. Tagging the ground planes together requires airbridge technology.

Parallel plate mode

Another mode, which can propagate through the coplanar waveguide structure, is called a parallel plate mode.

The picture below presents a schematic representation of the orientation of the E-field for this mode.

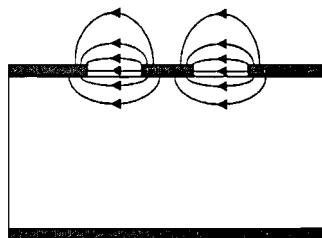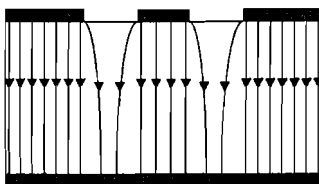Figure 2.9 Schematic orientation of the E-field for a parallel plate mode.

The basic TEM mode shows no cut-off frequency [37], a first estimate of the cut-off frequency for the higher order TM_x and TE_x modes is presented below:

$$f_{cut-off} = \frac{nc}{2H\sqrt{\varepsilon_{re}}}$$

[2.33]

Where H represents the substrate thickness, c equals the speed of light and n indicates the mode number.

Assuming a 400 μm thick AlN substrate, this formula would indicate that the higher-order parallel plate modes will not occur. It should be noted that the top plate is slotted and this may influence the behaviour of the parallel plate mode. The influence of the backside metalisation can be relaxed by increasing the substrate height, which in turn decreases the heat sinking capability of the substrate.

Transverse microstrip resonance [37]

Basic transmission line theory predicts another mode, which should be considered. The mode originates from the fact that open-circuit planes which are spaced at $\lambda/2$ can form a resonant structure. This situation could be valid for the transverse plane of the coplanar waveguide and hence the mode could be excited.

The propagation direction of this resonant mode is orthogonal to the dominant mode in the coplanar waveguide but at discontinuities this mode could couple to the normal propagating mode.

The formula presented below can be used to get a first estimate for the resonance frequency:

$$f_{resonance} = \frac{c}{2\sqrt{\varepsilon_{re}}\left(W + 2\Delta W\right)}$$

[2.34]

With

$$\varepsilon_{re} = \frac{\varepsilon_r + 1}{2}$$

[2.35]

$$2\Delta W \approx H$$

[2.36]

Where H represents the substrate thickness and c is the speed of light. W represents the lateral dimension of the line, which is equal to the width of the total line structure measured from ground plane to ground plane.

This mode can be suppressed by inserting small longitudinal slots into the ground planes, which should have little effect on the normal propagating mode.

3 Matching theory

3.1 Introduction

This chapter will present some basic considerations with respect to impedance matching [41], which is a part of amplifier design. The principle of impedance matching is presented below. A matching network is inserted between the transmission line, connecting the source to the load, and the load.
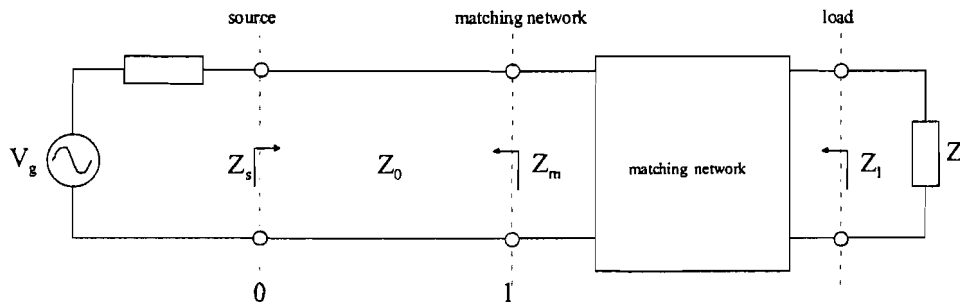
Figure 3.1 Definition of the notations for the terminated transmission line.

Ideally this matching network is lossless and is designed such that the load impedance transformed through the matching network equals the characteristic impedance, Z_0, of the transmission line. By doing this the matching network cancels any reflection between the load and the source, although multiple reflections will exist between the matching network and the load. From literature [41] it can be stated that there are several reasons for impedance matching:

* Impedance matching in a source can optimise power gain and power transfer to the load.
* Impedance matching in a power distribution network can reduce amplitude and phase errors.
* Impedance matching in receiver elements can improve the signal-to-noise ratio of the system.

The matching networks should pay attention to aspects like complexity, bandwidth and implementation. The matching network should be as simple as possible to reduce chip size, thus cost, and minimise the losses of the matching network. Any type of matching network can result in a perfect match on a single frequency, however a certain frequency band should be covered, which will result in an increase in complexity of the matching network. Finally matching networks can be divided into three basic categories:

* Lumped element, in this case a series of lumped element components, i.e. capacitors, inductors and resistors, are used as matching elements. This method is useable for the lower frequency range due to the limited frequency range in which the lumped elements can be used.
* Transmission lines, this category uses transmission line sections to match a source to a load. The most common types of matching networks are single and double stub tuning, and a quarter-wave transformer.
* Finally a hybrid can be used, normally this means that a transmission line replaces the inductance of the lumped element matching network, this is the most common type for MMIC HPA designs.

This chapter will start by introducing a simple model and an approximate solution for the matching network. Next a closer look at the lumped element solution is presented, together with an assessment on its usability, leading to a conclusion about which type of matching network should be used.

3.2 Approximate solution to the matching problem

Before a matching scheme can be derived, a model for the GaN HEMTs needs to be established. At present the GaN HEMTs are still under investigation, which means no large-signal model has been extracted. Since the amplifier design discussed here is only meant to get some insight into the required passive components a simple large-signal model will be used, as presented below.
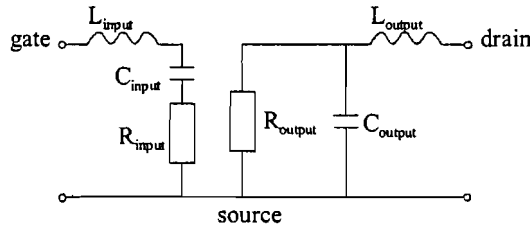
Figure 3.2 Simple large-signal GaN HEMT equivalent input and output impedance circuit.

Based on the performance of GaN HEMTs a breakdown voltage of 100 V combined with a current of 1 A could be obtained, leading to an output resistance of 100 Ohms. The other element values are derived from GaAs power HEMTs. The input inductance, capacitance and resistance have values of 70 pH, 5 pF and 1 Ω, while the output inductance, capacitance have values of 50 pH, 0.8 pF respectively.

The model of the GaN HEMT can be used to generate an approximate topology for the GaN power amplifier. The difference in impedance level should remain moderate, since large difference in source and load impedance cause a decrease in bandwidth. The picture below shows a GaN power amplifier lay-out based on four GaN HEMTs, the blocks identify the source and load impedance for each of the matching networks:
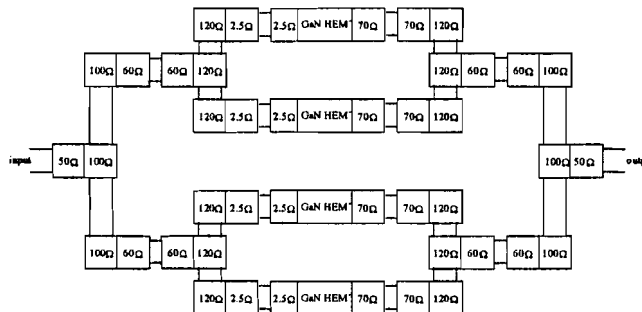
Figure 3.3 Impedance topology for a single stage amplifier using four GaN HEMTs .

After using a shunt inductance, as will be discussed later, the GaN HEMT has an output impedance of approximately 70 Ω at 10 GHz, the first step matches this impedance to an impedance of 120 Ω. After the matching networks these outputs are paired by 120 Ω transmission lines, the resulting output of this pairs result in an impedance of 60 Ω. The second matching network matches this 60 Ω to a 100 Ω transmission line, which result in a 50 Ω output impedance after the two 100 Ω transmission lines have been paired.

Using this general topology of the amplifier, a closer inspection of the required matching networks is performed. The result of which is presented on the next page.

Using the simple large-signal equivalent circuit combined with the chosen impedance levels at different points of the amplifier matching scheme an approximate matching network lay-out can be established. A simple method, which can be used to determine the capacitance and inductance values required for these matching networks, is presented below.

The routine used to match the FETs to 50 Ohms consists of two main steps, the method will be described using the output of the FET as an example. First the complex output impedance of the FET is converted to another real impedance by using a complex conjugate match, every step after this only has to match a real impedance to another real impedance. Theoretically this method only functions at a single point but in practice this method can produce reasonable results over a small frequency band.

First the output admittance needs to be calculated for a specific frequency, for instance 10 GHz. This in turn can be used to calculate a shunt inductance, L_{real}, to make the admittance real, using the known values for C_{out}, L_{out} and R_{out}, 0.8 pF, 50 pH and 100 Ω respectively, a shunt inductance of 0.27 nH can be used to transform the complex output impedance to a real impedance. Furthermore the shunt inductance can also be used to feed the power HEMT with a DC power supply.

The next steps transforms the remaining real impedance to another impedance using a LC-combination. A resistor could also be used but that would lead to losses, while the inductor and capacitor, in the ideal case, do not introduce any losses in the matching networks. The relations that relate the impedance differential to the inductance and capacitance values are presented below:

$$L_{series} = \frac{Z_{source}}{\omega} \sqrt{n-1}$$ [3.1]

$$C_{shunt} = \frac{1}{\omega Z_{source}} \sqrt{\frac{n-1}{n^2}}$$ [3.2]

Where n is the transformation ratio, which is defined as:

$$n = \frac{Z_{goal}}{Z_{source}}$$ [3.3]

These equations are valid if the transformation ratio is greater than unity, otherwise similar equations can be derived. One branch of the amplifier design, obtained using equation [3.2] and [3.3], is shown below:
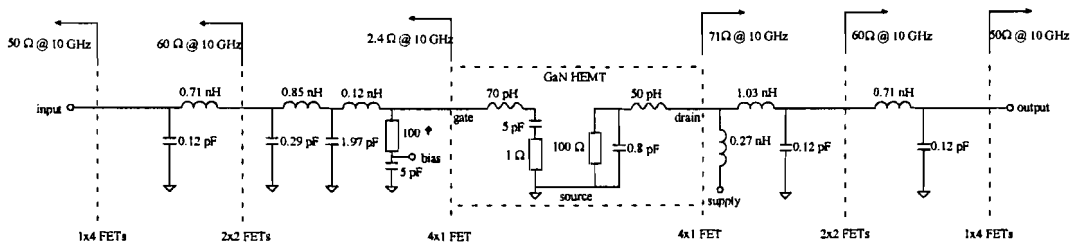
Figure 3.4 Amplifier topology for a lumped element approach.

It is important to notice the fact that the impedance transformation of the gate is performed in two steps. This is done to increase bandwidth and limit the required capacitance and inductance values. The inductance and capacitance values as indicated in the amplifier topology can be seen as a first guess for simulation purposes. By the time the final large signal HEMT model becomes available the amplifier topology can be adapted to reflect the changes in the HEMT input and output impedance.

3.3 Lumped element matching solution

This section will start with a brief overview of the passive components, followed by an assessment of the viability of a GaN high-power amplifier with lumped element matching networks.

3.3.1 Overview of lumped element components

Lumped element resistors

The preliminary amplifier only shows one resistor, but in practice it might be necessary to add more resistors to force stability. These resistors need to be independent of the voltage across them and a value of 100 ohms per square can be used to create a wide range of resistances. Both series and shunt resistances are desired.

The two types of lumped element resistors that are frequently used are:

- Semiconductor bar, a bar of GaN can be used to form a resistor, the main disadvantage of this type of resistor is the bias dependency, the advantage stems from the fact that the technology to fabricate these components is already available from the HEMT process.
- Thin film, in thin film technology a thin metal layer, normally NiCr, is sputtered onto the chip, this metal layer has a relatively high resistivity, yielding the 100 ohms per square.

Due to the fact that a semiconductor bar resistor is much less ideal than a thin-film resistor, the thin film resistor will be reviewed, a lay-out and an equivalent circuit are presented below:
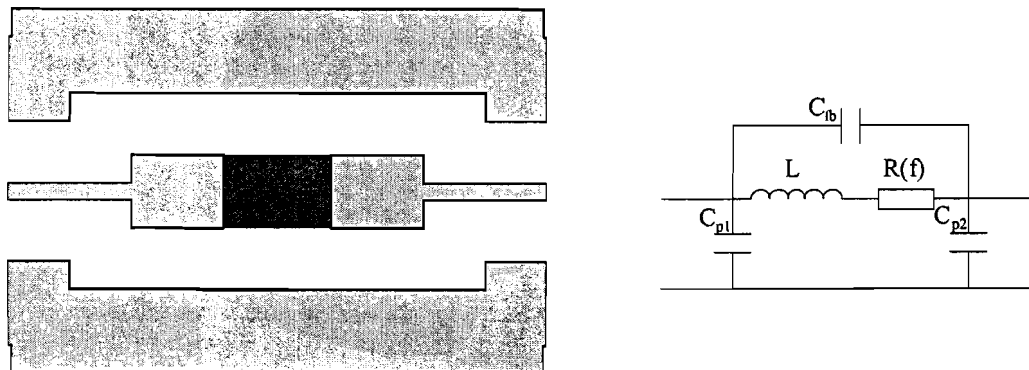
Figure 3.5 Thin-film resistor lay-out and equivalent circuit.

The first thing that should be noticed in the circuit is the frequency dependence of the main component R(f), the resistor is frequency dependent due to the skin effect which may not be neglected at these frequencies. The inductor, L, models the inductance of the input and output lines while the capacitor, C_{fb}, models the coupling between the input and the output. The shunt capacitors, C_{p1} and C_{p2}, model the coupling to the ground planes.

The advantages of thin film resistors are the fact that it is bias independent and the resistance per square can be adjusted during processing by applying a thicker or thinner layer. However, the technology required for the fabrication of these types of passive components is no longer present at Eindhoven. Another negative point is the fact that an additional mask is required for the definition of the NiCr resistor while GaN bar resistors can be made using the masks available in the HEMT process.

lumped element capacitors

The preliminary amplifier covered a capacitance range of 0.12 up to 5 pF, to be on the safe side the models should extend to up to 10 pF. The expected operating voltage of the amplifier extend up to 75 volt, the capacitors should aim at a breakdown voltage in excess of 150 volts.

The most common capacitor layouts are:

- Interdigitated, this type of capacitor is formed by a series of fingers connected in turns to each side of the capacitor. The total capacitance is determined by the perimeter, which is shared by both capacitor ends. The capacitance is limited to approximately 0.5 pF.
- Metal-Isolator-Metal, this type of capacitor is formed by two parallel plates that are separated by a thin film of dielectric material. Capacitance values of up to 10 pF are readily obtained.

The figures below present an example of a series capacitor with its equivalent circuit.
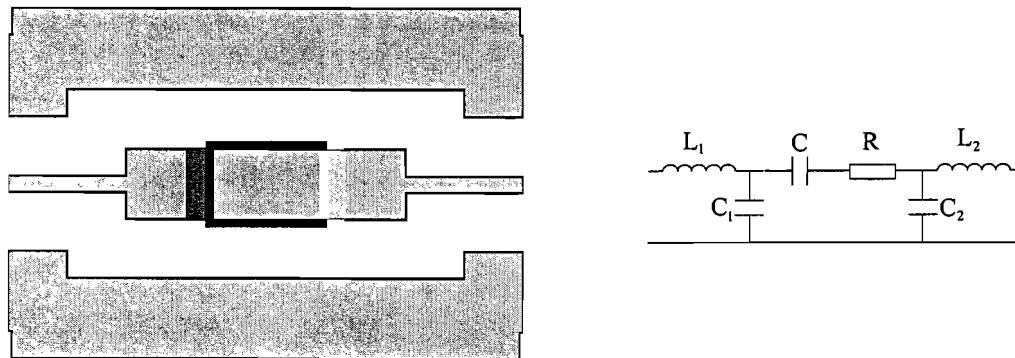
Figure 3.6 MIM-capacitor lay-out and equivalent circuit.

the series capacitor, C, models the main capacitance while the resistor, R, models the losses of the lower metal plate, which has not been plated. The shunt capacitors, C_1 and C_2, model the coupling to the ground planes while the inductors, L_1 and L_2, model the inductance of the input and output lines.

A remark has to be placed in regard to the necessity of airbridge technology, one could argue that the top plate could be made to rest on the insulator surface and no airbridges would be required. Although this is an option, the breakdown voltage of such a structure is lower and is therefore not commonly used.

A set of experiments was performed on some rudimentary MIM capacitors, the capacitors had a top plate of 100x100 μm and a SiO_xN_y dielectric with 300 nm thickness. No overlap between the top plate and the dielectric was present, which could lead to early breakdown at the edges of the MIM-capacitor.
The capacitors have shown a breakdown voltage in excess of 150 volts and a capacitance of 2 pF.

The advantages of MIM capacitors can be found in the high capacitance per unit chip area and the possibility to change the capacitance and the breakdown voltage by changing the dielectric thickness. On the downside the need for airbridge technology and the higher series resistance due to the thin lower plate are mentioned.

lumped element inductors

In the preliminary amplifier design, inductance values up to just over 1 nH can be observed, for modelling purposes this maximum value will be set to 2 nH so that room remains for alterations.

The most common inductor layouts are:

- Single loop, a thin metal track is curved into a loop, this way a relatively long line can be formed which does not require airbridge technology. The disadvantage is that a limited range of inductance values can be obtained.
- Circular spiral, the spiral inductor is formed by a gradual helix with an airbridge to connect the inner contact with the outside world. Most circuit simulators do not support this type of spiral inductor, probably due to the high modelling complexity.
- Octagonal spiral, a structure similar to the circular spiral except that the circles have been approximated by eight corner structures. This results in a simpler layout, but again ,most circuit simulators do not support this type of structure.
- Square spiral, again similar to the circular spiral inductor but now with right angle bends. Experimental results have shown that this structure has a higher series resistance, about ten percent, which limits its behaviour. This is the most common solution since it is supported by the simulator.

A lay-out example and a commonly used equivalent circuit of a spiral inductor are presented below:
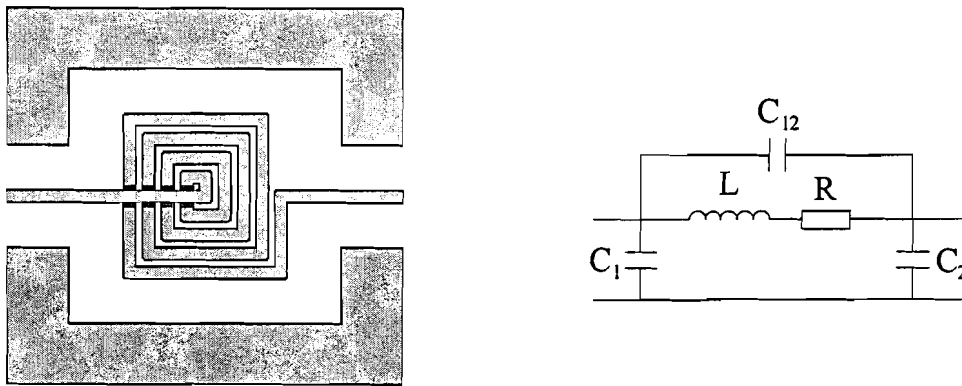
Figure 3.7 Spiral inductor lay-out and equivalent circuit.

It must noted that with a growing number of turns the single section equivalent circuit has to be replaced by a series of sections, and a feed through capacitor, C_{12}, between the input and output.
The inductor L models the main inductance of the spiral inductor while R model the metal losses.
finally C_1 and C_2 are used to model the coupling to the ground planes.

The fact that high inductance values can be obtained combined with the relatively low chip area required to do so, are the main advantages of the spiral inductor. However, the spiral inductor requires an airbridge to connect the inner contact to the outside world, which means that the tracks under the airbridge will not be plated and suffer from high series resistance. This in turn introduces higher losses and limits the current carrying capability of the total inductor.

3.3.2 Assessment of the lumped element solution

Several criteria have to be met before the lumped element matching networks can be approved. Now that the structures have been introduced a closer look at these requirements can be presented.

Lumped element size

The size of the structures is limited by the lumped element assumption, basically this means that the total length and width of the structures should remain small compared to the effective wavelength at a certain frequency. In general a limit of $0.1\lambda_{effective}$ is assumed to be adequate, a simple calculation results in a maximum dimension of approximately 1 mm at 10 GHz for a AlN or GaN substrate.

Breakdown voltage

The capacitor and resistor should be able to deal with the operating voltages of the GaN amplifier, preferably the breakdown voltage of these components should exceed twice the operating voltage. Experiments on some basic lumped element capacitors showed breakdown voltages in excess of 150 Volts for a 150 nm thick SiO_xN_y dielectric layer, resulting in a 2 pF capacitor at an area of 100x100 μm. This indicates that the breakdown voltage will not pose a problem for the capacitors from the approximate matching solution.

Current limits

The current limit requires some additional attention, the process which limits the current a conductor can carry is called electromigration. Due to high-current density, caused by an increased current combined with a decrease in interconnect size, the electrons gain enough momentum to stimulate drift of gold-ions. For this reason electromigration is sometimes referred to as 'electron wind' force, this wind force causes failures:

- open circuit, or voids, in the metal tracks carrying the current.
- short circuit between two metal tracks caused by stacks of metal ions, or hillocks.

A simple design rule yields a current density limit of approximately 15 mAμm^{-2}, this means that a 2μm thick conductor carrying 1 ampere should be at least 35 μm wide. For the expected current densities in the GaN high-power amplifier the current density will cause impractical conductor dimensions for spiral inductors.

conclusion

A matching solution based on lumped elements will not be possible due to the conductor cross-section required for long-term operation.

It has been shown that MIM capacitors can be engineered with break down voltages well above the operating voltage of the amplifier. This indicates that the lumped element/transmission line hybrid solution could be realised. For any practical matching solution the resistor process needs to be implemented.

The next chapter will introduce the measurements. First a mask is defined, which is used to extract a scalable model for a conductor backed coplanar waveguide. The problems that can be expected in the extraction of the scalable model are introduced and solutions are proposed.

4 Measurement theory

4.1 Introduction

In circuit simulators like ADS, MDS and LIBRA microstrip element models are readily available. This means that microstrip circuits can be designed using the models that are available in these simulators. For circuits based on coplanar waveguides, only the most basic components are included in the simulators, which means that the remaining components need to be modelled before a circuit can be designed. This chapter introduces methods to extract models from measurements on coplanar elements.

The first step is to determine under what conditions the models should be valid. The models are intended for an X-band power amplifier MMIC, this means that the desired frequency ranges from 8 GHz up to 12 GHz. The models should be valid to the highest frequency possible. Furthermore the term MMIC implies that all elements will be integrated on one substrate thus the models should allow for this high level of integration.

Using the knowledge about the operating frequency a measurement set-up can be selected. In this case the choice is rather straightforward. At microwave frequencies a vector network analyser, HP8510, is used to measure the scattering parameters of the devices. Furthermore the high level of integration requires that the structures are measured on wafer. Normally coplanar probes are used to contact the structures. The picture below shows an active device with two coplanar probes :
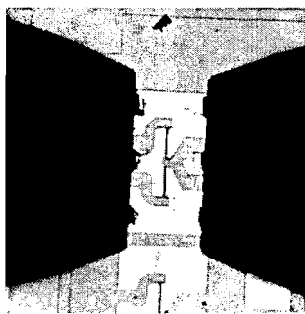

Figure 4.1 An example of a coplanar probe and the probe pad configuration.

The first step of any measurement is the calibration of the measurement set-up, in literature a large range of calibration techniques have been reported [19-28]. The Through-Reflect-Line (TRL) technique was used in the measurements for this study. After this calibration step the reference plane is placed on the probe tips. The reference plane is the position up to where the measurements have been corrected for systematic errors.

In this work, the measurements will be focussed on transmission line elements. However, the methods that will be used for the transmission line elements will be used for other types of elements in future work. This means that the methods are more complex that strictly needed for the transmission line examples used here.

Next the line is placed between the probe pads, which cause a distortion of the transmission line behaviour. Any measurement based model approach has to account for the effect of the probe pads on the total model. An calibration procedure is used to extract the pad structure parameters, this step is called de-embedding.

The method used to extract the pad structure is able to extract all the S-parameters of the pad structures. Unfortunately these parameters are normalised to the characteristic impedance of the lines connected to the pad structure. At the probe side this impedance equals the 50 Ω of the measurement set-up. However the impedance on the structure side equals the unknown characteristic impedance of the line connected to the pad. Section 4 will present methods to extract the characteristic impedance of the line from measurements.

The next section will present the mask that was used to test all de-embedding and pad structure extraction algorithms. It also contains the structures, which are required to extract a scalable model for a conductor backed coplanar waveguide.

4.2 Transmission line mask

The results obtained in chapter 3 have resulted in the design of a maskset that can be used to process and measure a large range of transmission line structures. The first goal for the maskset was to be able to test the three pad extraction algorithms and support other possible algorithms if needed. The second goal was to gain more insight into the behaviour of some coplanar transmission lines and to extract both the characteristic impedance and propagation constant of these transmission lines.

Common calibration algorithms require a through, a delay and a reflective standard, short or open, this standard should preferably be identical for both ports. This means that these four elements should be included on the mask.

To test the transmission line properties a large range of characteristic impedances is required. Another constraint is posed by the current carrying capability. Assuming a metal thickness of 2 μm in combination with a current density limit of 15 mAμm^{-1} results in a desired range of transmission line widths of 25, 50, 75, 100, 150 and 200 μm. The spacing of the lines was chosen at 10, 20, 40, 80, 160 and 320 μm since it turned out to be the limiting factor, instead of the characteristic impedance. Finally a series of line lengths was included, the lengths are 400, 800, 1600 and 3200 μm. The distribution of the characteristic impedances based on Heinrich [7] is presented below:
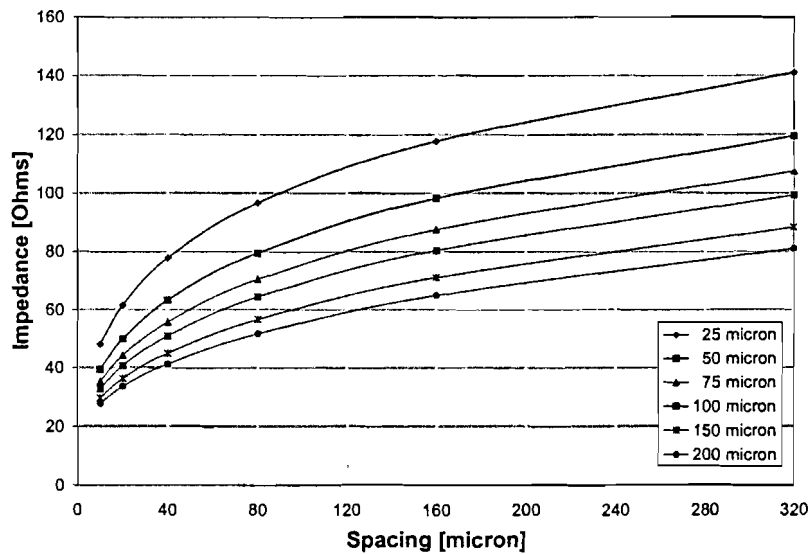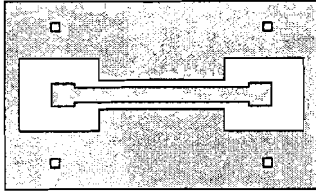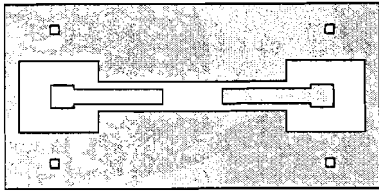
Figure 4.2 Targeted distribution of the characteristic impedance distribution.

The graph shows that the chosen width and spacing values yield an acceptable range of characteristic impedances. The final distribution will differ from this distribution due to the fact that the laterally large structures, i.e. the 150 and 200 μm wide lines and the structures with 160 and 320 μm spacing, will show deviating behaviour.

A short list showing the different elements which are included on the transmission line test structures mask and a short description showing their purpose is presented in the table below:

Table 4.1 overview of the transmission line test structures.

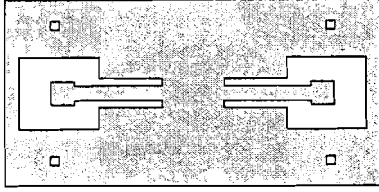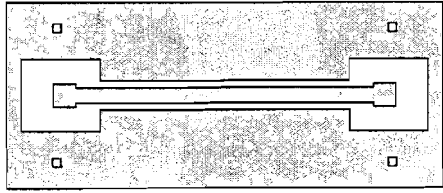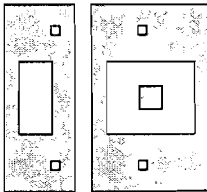|	
through The through structure is intended for de-embedding purposes, a short section of transmission line is added to the pad structure to ensure a gradual transition to the elements placed in between the two pad structures.	
open An open is commonly used in general calibration procedures. It can also be used to get an idea about the quality of the extracted pad structures.	
short A short is commonly used in general calibration procedures. The short can also be used to get an idea about the quality of the extracted pad structures.	
lines The shortest transmission line is used for the extraction of the pad structure. The propagation constant is extracted from all lines available, and should remain constant. The different line lengths can also be used to verify whether the measured capacitance scales with line length.	
probe test structure These structures can be used to get an estimate of the combination of the probe stray capacitance and the open end capacitance of the transmission line.	

Since it has been established which structures should be present on the mask, the final layout can be made. This layout has to be made in such a way that the cells fit on the samples, the sample measure 1.5x1.5 cm, which means the cells need to remain below 1.0x1.0 cm. Since the total mask should not exceed 3.0x3.0 cm a choice was made to divide the mask into nine blocks of 1.0x1.0 cm, which resulted in the mask below:
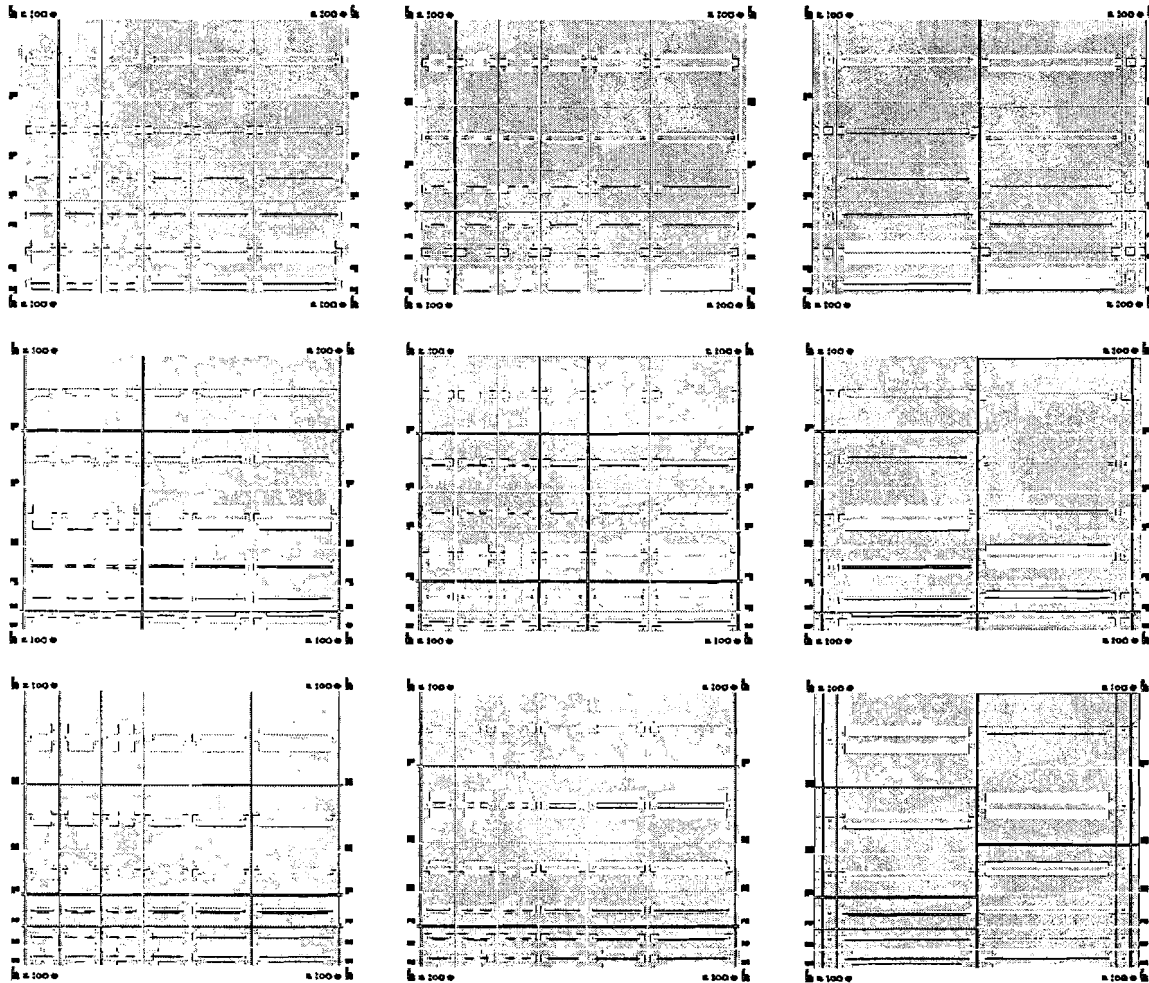
Figure 4.3 The final layout for the transmission line test structure mask.

The first two columns contain the through, open, short and three shortest lines while the block on the right contains the largest lines for the two columns on its left. Each block is built up from bottom to top with increasing line width and spacing, each subsequent block adds an offset to the spacing. This means that the six blocks in the first two columns contain all possible width-spacing combinations, while the block size remains approximately equal. To facilitate measurements the width and spacing is written before and after each line in each block.

4.3 Extraction of the pad structure

Literature presents a wide range of methods that are able to separate the pad structure from the line [28,33]. TNO-FEL and TU/e have suggested the Line-Reflect-Line (LRL) and Through-Short-Delay (TSD) methods respectively. These two methods have been implemented and tested to see which method performs best. Finally a third method was implemented which uses knowledge of the structure to facilitate calculations.

Although the TSD and LRL differ in name they refer to the same set of structures. The difference between the two methods is the way they deal with the set of mathematical equations that needs to be solved. The complete description of both methods can be found in appendix B.

Figure 4.1 Standards used for both the LRL and TSD algorithms.

The LRL and TSD algorithms use two error boxes, one for each pad on the structure. Since two error boxes are used, differences caused by 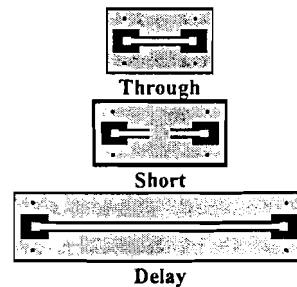measurement and processing variations can be accounted for. However, the purpose of the error boxes is to use them on other structures, which is only valid in case the processing and measurement variations are small compared to the actual measurement.

The third method assumes that both pads are identical, an estimation of the error in this assumption is obtained by comparing S_{11} with S_{22} and S_{12} with S_{21} for the measurements. A second assumption is that the pads are reciprocal, which means S_{12} should equal $S_{21.}$ With these assumptions only two calibration standards are required, a through and a delay. This method will be referred to by BCL algorithm.

The disadvantages of the LRL and TSD methods lie in the fact that no direct solution is obtained, a root selection problem remains which can be solved by knowledge of the structures. Another disadvantage of the original routines is that three standards are required for the extraction. The assumptions used for the third method can also be used for the TSD and LRL routine, resulting in symmetrical LRL and TSD algorithms, the resulting simplified algorithms are also able to extract the pad structure using only two standards.

The symmetrical algorithms were implemented into MATLAB, the routines were programmed straight forward using the advanced mathematical capabilities of MATLAB. To test whether the implementation of an algorithm was done correctly a test was performed.

First Sonnet EM simulator was used to generate data for a pad structure, this way no pad structure equivalent circuit needs to be determined. After this the data for a through and delay structure were generated using a fictional but realistic propagation constant. This data was then fed into the extraction algorithms and the extracted pad structure was compared to the original generated by Sonnet.

All three methods were able to correctly reproduce the pad structure, indicating that the methods were implemented correctly.

The test presented above checked whether the algorithm was implemented correctly, however it did not test the capability of the algorithm to deal with measurement uncertainties. These measurement uncertainties should remain small but they can propagate through the calculations, simple numerical methods theory indicates that the result can no longer be guaranteed to be accurate. To test the influence of measurement uncertainty the previously described test was modified.

Again Sonnet was used to generate pad structure data. This data was then used to create the necessary through and delay data. At this point the data was corrupted with a random component. The data was then fed into the extraction algorithms and the output was compared to the original pad structure. After an error was calculated, the extracted pad structure was used to create new through and delay data, which was than used for another iteration step.

The result of the error in the magnitude and phase of the transmission of the pad structure for the three algorithms is presented below.
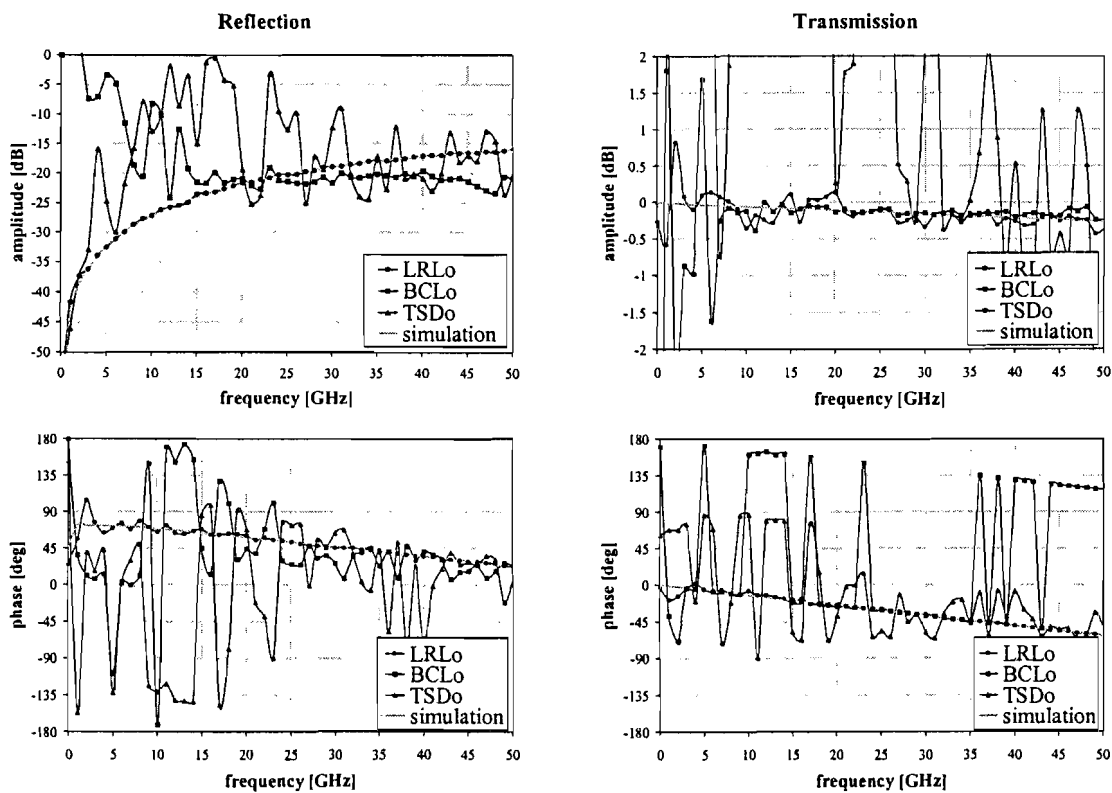

Figure 4.2 Error propagation through the original extraction methods.

This clearly shows that the methods, implemented directly into MATLAB, have problems with the calculations. A numerical optimisation step was used to simplify the calculations and reduce the number of unnecessary operations.

To illustrate how the algorithms were optimised, two versions of the equation for S_{11} are presented below, before and after optimisation respectively.

$$S_{11} = \frac{\left(1 - \dfrac{\dfrac{(1-T_r)(1+T_r)+T_t^2}{T_t}+2}{(1+T_r)^2 - T_t^2}T_t\right)\left(1 + \dfrac{(1+T_r)^2 - T_t^2}{4T_t}Y_3^2\right) + Y_3^2}{\left(1 + \dfrac{\dfrac{(1-T_r)(1+T_r)+T_t^2}{T_t}+2}{(1+T_r)^2 - T_t^2}T\right)\left(1 + \dfrac{(1+T_r)^2 - T_t^2}{4T_t}Y_3^2\right) - Y_3^2}$$ [4.1]

The first equation contains approximately 50 mathematical operations while the second contains 10. The same principle has been applied to the extraction algorithms, the result is presented in appendix B.

$$S_{11} = T_r + \frac{(1+T_s)^2 Y_3^2 - 4T_t}{(1+T_s)^2 Y_3^2 + 4T_t} T_t$$ [4.2]

After the optimised algorithms were implemented, they were tested, as presented below:
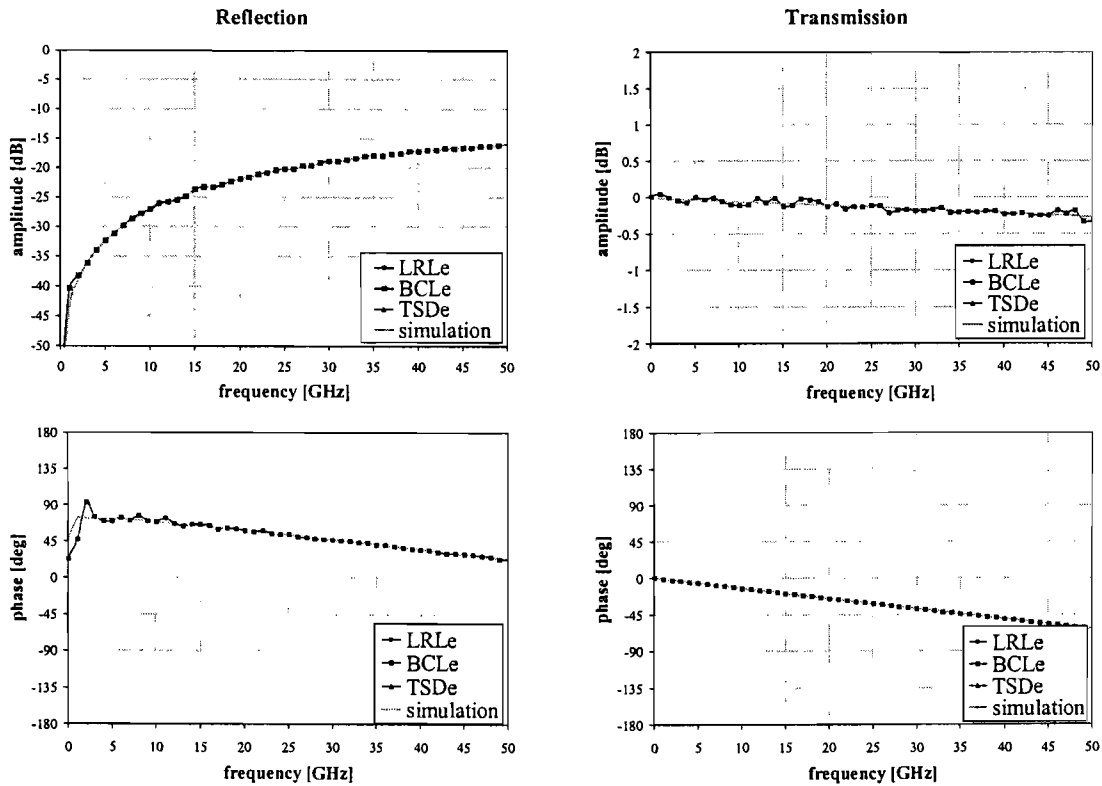

Figure 4.3 Error propagation through the optimised extraction methods.

These graphs clearly show that the TSD and LRL method are numerically stable while the alternative procedure has more problems. An accurate comparison between the TSD and LRL methods shows that the LRL method is the most robust of the three methods.

4.4 Capacitance measurements and calculations

The LRL, TSD and the alternative de-embedding algorithm are able to extract the normalised scattering parameters of the pad structure and are thus able to de-embed the device under test. However, the scattering parameters are normalised to the characteristic impedance of their environment. At the probe tips this characteristic impedance is 50 Ohms. Unfortunately this is no longer the case after the probe pads, since at this point the impedance is determined by the transmission line connected to the device under test.

It is desired to extract both the characteristic impedance and propagation constant from the same series of measurements, and though a lot of research has been performed on this subject no satisfactory solution has been found. In case the pad structure is modelled by a simple lossy capacitor and inductor [13], the problem is simplified such that the characteristic impedance can be solved from the scattering parameter measurements. Since these methods are limited in their application, they will not be used for this study.

Other investigations [29-33] determine the characteristic impedance of a transmission line from one of the generalised circuit parameters of the line. For any transmission line, the generalised circuit parameters C, G, R and L are defined in terms of the characteristic impedance Z and the propagation constant γ by:

$$\frac{\gamma}{Z_{line}} = j\omega C + G \qquad [4.3]$$

$$\gamma Z_{line} = j\omega L + R \qquad [4.4]$$

The inductance L and resistance R of the transmission line depend strongly on frequency while the capacitance C can be replaced by the near DC capacitor C_0. This means that the choice of determining C and G separately is the logical choice. Several methods have been proposed to extract the capacitance from measurements, simulations or analytical calculations.

Williams [30,31] proposes two methods to extract the capacitance from measurements. The first method uses network analyser measurements down to 5 MHz while the second method requires processing lumped element loads. At current the technology for processing lumped element resistors is not available, which means that no lumped loads can be processed. Furthermore, the HP 8510 measurement set-ups that will be used have a minimum frequency of 50 MHz. This means both methods cannot be used for this work.

In this section a technique will be presented which does not require any additional structures or processing, and can be performed with the available equipment. As a means of verification of the measured capacitance two methods will be presented which extract the capacitance of the transmission line from simulations or calculations. Since the structures will be fabricated on good insulating material it suffices to extract the capacitance since the conductance can be neglected, in this case the characteristic impedance follows by:

$$Z_{line} = \frac{\gamma}{j\omega C_0} \qquad [4.5]$$

4.4.1 Determining of C_0 from conformal mapping.

The capacitance that was measured will be used to calculate the characteristic impedance of the line. This means that any error in the capacitance will directly translate into an error in the characteristic impedance. To be able to confidently present the capacitance of a line it is necessary to have a method to verify the measured capacitance, for this purpose two conformal mapping algorithms were used [7,13].

Conformal mapping theory [38]

To describe the principle of conformal mapping the simplest coplanar waveguide structure is used, which means that both the substrate and ground planes are assumed to be infinite.
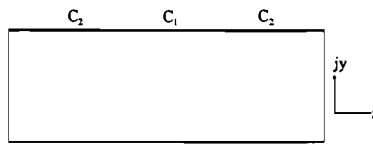

Figure 4.4 Cross-section of an ideal coplanar waveguide in the Z-plane.

In order to find the transmission line parameters, Laplace's equations needs to be solved.

$$\nabla^2 \varphi = \frac{\partial^2 \varphi}{\partial x^2} + \frac{\partial^2 \varphi}{\partial y^2} = 0$$

[4.6]

with the appropriate boundary conditions

$$\varphi = \varphi_1 \quad \text{on } C_1$$
$$\varphi = \varphi_2 \quad \text{on } C_2$$

[4.7]

Although the structure is relatively simple, an analytical solution for Laplace's equation has not yet been obtained. At this point the strength of conformal mapping becomes apparent. Essentially conformal mapping is a method, which transforms the transmission line geometry to another, less complex geometry.

Assume that a conformal mapping transform can be found which transforms any point x+jy in the Z-plane to an alternative point u+jv in the W-plane such that the dielectric is enclosed between the surface S_1 and S_2.
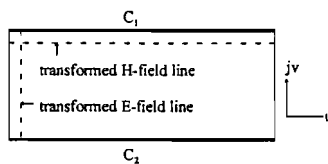
Figure 4.5 Cross-section of an ideal coplanar waveguide in the W-plane.

The field solution can easily be solved in the W-plane and once a solution in the W-plane is known the solution can be mapped back onto the Z-plane, thus resulting in a solution in the Z-plane. The exact details of the solution depend heavily on the exact nature of the problem and intended use and will thus not be treated.

The conformal mapping method has been used for a wide range of coplanar waveguide problems [7,10-13] while another commonly used approach uses measurement based models [7,14] or full-wave or mode matching analyses [8,9].

Quasi-TEM method proposed by Heinrich [7]

The coplanar waveguide geometry that was investigated by Heinrich is presented in the picture below, it exists of a single coplanar waveguide with two finite grounds and an infinite substrate. Heinrich also accounts for the influence of metalisation thickness.
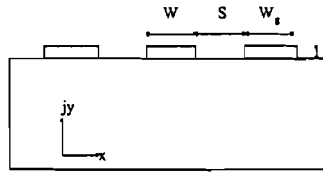

Figure 4.6 Cross-section of an ideal coplanar waveguide in the Z-plane.

Essentially Heinrich divides the problem into two regions, the air and the substrate, and solves the capacitance for each of those two areas separately. The resulting equations are presented below:

$$C_{air} = 2\varepsilon_0 F(t = t')$$ [4.8]

$$C_{sub} = 2\varepsilon_0\varepsilon_r F(t = 0) = 2\varepsilon_0\varepsilon_r \frac{K(k_1)}{K'(k_1)}$$ [4.9]

Where K(k) and K'(k) are the elliptic integrals that result from the conformal mapping algorithm [7]. In this formula the function F(t) denotes a function created by Heinrich and k_1 is a geometrical factor obtained from [7]. It is partially based on a conformal mapping algorithm and partially based on a polynomial fit. It can be noted that the metalisation thickness is only used in the air capacitance, which is approximately nine times lower than the substrate capacitance. Both air and substrate capacitance are assumed to be independent of frequency.

The quasi-TEM approach assumes that the dominant mode can be represented by a TEM mode. This posses various frequency and geometry limits. First of all the substrate thickness must remain large in comparison to the lateral dimensions of the coplanar waveguide, normally greater than twice the ground-to-ground spacing. Second the structure needs to be small compared to the effective wavelength, which means that the maximum frequency can be defined by:

$$f \leq \frac{1}{10} \frac{1}{\sqrt{\varepsilon_0\varepsilon_r\mu_0}} \frac{1}{W + 2S}$$ [4.10]

Adapted conformal mapping algorithm as proposed by Williams

Williams adapted the conformal mapping algorithm proposed by Heinrich to model multilayer structures. Although this algorithm was not intended for conductor backed coplanar waveguide it can be used as such.

As the method is based on the quasi-TEM description proposed by Heinrich it can be expected that the limits proposed for Heinrich can be maintained. Except for the substrate thickness limits which is accounted for.

4.4.2 Determining C_0 using a HP4275A LZR meter

The capacitance of the transmission lines can be measured using a HP 4275A, which can achieve fF accuracy in case the measurement set-up is constructed as to minimise the parasitic capacitance. The measurement set-up that was used for the measurements is depicted below:
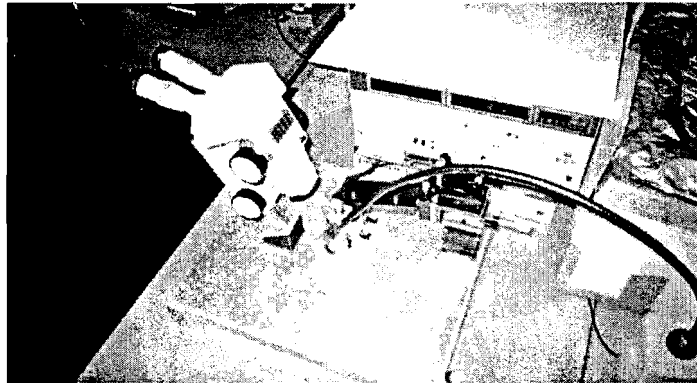

Figure 4.7 The measurement set-up that was used for the capacitance measurements.

The HP 4275A can calibrate to fF scale at a frequency setting of approximately 2 MHz. At this frequency the assumption that the lines are short with respect to the effective wavelength holds. This means that the transmission line can be divided into three regions, two pads and a transmission line, as presented below.

pad   line   pad
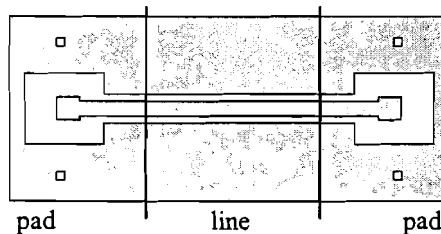
Figure 4.8 Separation of the pad structures and the transmission lines.

It is assumed that the behaviour of the pad structure can be estimated by a simple transmission line equivalent circuit with two unequal capacitors and conductors. This means that the entire equivalent circuit consists of three cascaded sections, one pad section is presented below:
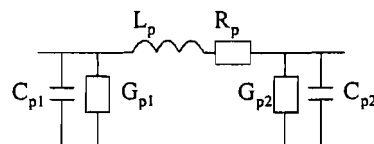
Figure 4.9 Low-frequency equivalent circuit of a pad structure.

This equivalent circuit can be reduced to a single capacitor. It can be shown that the error introduced by this simplification remains well below 1 percent. The capacitance will be determined by measurements on five different line lengths. The shortest line, a through, is subtracted from the remaining lines and finally a simple linear fit through the origin is performed. The next chapter will present the measurement results.

5 Measurement results

5.1 Introduction

All structures that are required for a measurement-based approach to model coplanar waveguide elements have been determined. A first mask containing the elements required to test several de-embedding methods and to get a first impression of the problems to expect in a subsequent mask are identified. This chapter will present the results from measurements together with some experiments, which provide more insight into the problems that occur.

Before the measurements the HP8510 network analyser needs to be calibrated. For this work the TRL calibration was used. This calibration was performed on a 101-190B ISS substrate, which contains all the required structures. The input power was set to −5 dB with a slope of 0.1 dB/GHz and a 0.0 dB attenuation. After the calibration the influence of the measurement set-up is corrected for up to the tips of the probes.

The remaining calibration standards are an open, probes in air, and three line lengths. Normally two line lengths would have sufficed but the transition between the lines would be placed between 9 and 12 GHz. Since the final goal is to use the measurements for a 9 GHz amplifier three standards, 5200, 1750 and 850 μm long, were chosen.

In this chapter the measurement results will be compared with theoretical data. The data will be presented in tables, which contain both the data and coloured bars. These bars give some insight into the difference between the measured data and the calculated data, as shown in the table below:

Table 5.1 Definition of the error bound labels.

	≤ 2.5 %
	2.5-5.0 %
	5.0-7.5 %
	≥ 7.5 %

Section two presents some typical measurement results. These results are intended to present some insight into the measurement data that was obtained. Also a short review is presented which shows the correlation between coplanar waveguide geometry and the measured reflection and transmission.

Section three introduces the results from the capacitance measurements and they are compared with two conformal mapping techniques. Finally the measured capacitance values are fitted to a polynomial to form a simple design equation.

Section four introduces the results, which were obtained using the pad extraction algorithms together with the scaling properties of the pad structures.

Section five introduces the results from the de-embedding algorithm that was used to extract the propagation constants. The extracted propagation constants are compared to the conformal mapping algorithm proposed by Heinrich and to the results of TXLine, which is a commercially available transmission line calculator.

Section six presents a set of tests that were performed to study the influence of backside metalisation and substrate thickness.

Finally section seven presents some general conclusions which can be drawn from the measurement results obtained in this chapter.

5.2 Evaluation of the measurements

5.2.1 Quasi-TEM versus non-quasi-TEM structures

The mask from the previous chapter was measured. This section will introduce those measurements by presenting some typical measurements. As can be expected the measurements also reflect the division of the mask into a quasi-TEM section and a section where the quasi-TEM assumption no longer holds.
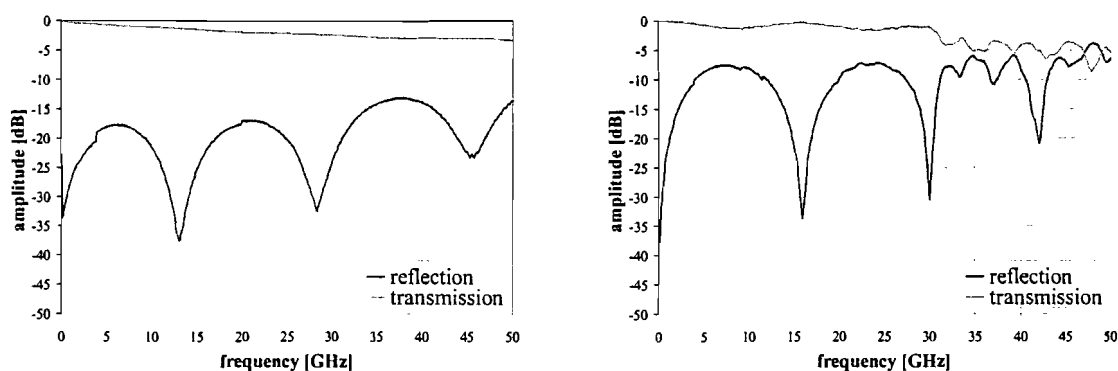

Figure 5.1 Example of a quasi-TEM, left, and non-quasi-TEM, right, transmission line.

The figure on the left shows the typical behaviour of a quasi-TEM transmission line. The line has a width of 50 µm, a spacing of 80 µm and a length of 3200 µm. The top curve shows the transmission, which is near unity, and the lower curve shows the reflection, which approaches zero at DC. This behaviour resembles the behaviour as presented in chapter two.

The figure on the right, which has a width of 200 µm, a spacing of 320 µm and a length of 3200 µm, shows non-quasi-TEM behaviour. The first change that can be noticed is that the curves are distorted above 20 GHz. Furthermore no fixed period can be found, a minimum appears at 16 GHz, at 30 GHz and at 40 GHz.

If a distinction is made between structures showing quasi-TEM and non-quasi-TEM behaviour, the following table can be found:

Table 5.1 Separation of the measurements in quasi-TEM and non-quasi-TEM.

		Width [µm]					
		25	50	75	100	150	200
Spacing [µm]	10						■
	20					▓	■
	40				▓	■	■
	80				▓	■	■
	160				▓	■	■
	320	▓	▓	▓	■	■	■

The table shows a division into three shades of grey, the lightest grey indicates that the measurements are predominantly quasi-TEM while the darkest grey indicates that the non-quasi-TEM effects start to dominate the measurement. The distribution is in agreement with the validity boundary predicted by Heinrich.

The examples used in this chapter will be taken from the quasi-TEM region, since the curves from the non-quasi-TEM region show entirely different behaviour.

5.2.2 Scaling properties of the transmission line structures

To indicate the scaling properties of the transmission lines, a set of measurements will be presented that show the behaviour of different through structures. This presents some insight into how the structures scale with geometry. The first picture shows the effect of the spacing between the ground and the centre conductor. The width of the lines is 25 μm while the spacing ranges from 20 up to 80 μm. The reflection is relatively low, witch indicates a good match while the transmission is almost unity, which indicates that the losses are low.

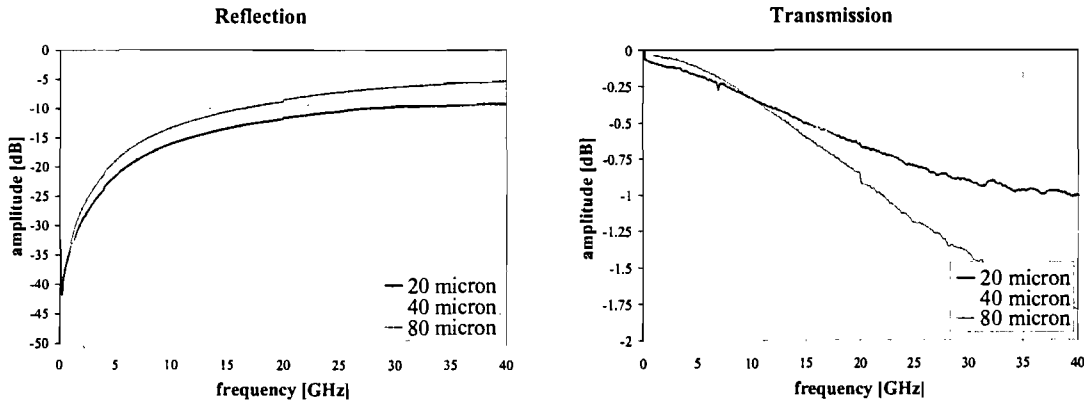Reflection   Transmission

Figure 5.1 Effect of scaling of the spacing on the through structure.

It can be observed that the reflection increases with increasing spacing, on the other hand the transmission decreases with increased spacing. This can be expected since an increase in characteristic impedance causes an increase in reflection coefficient since the impedances increase starting from approximately 50 Ω. The pad discontinuity has been neglected to get a first impression.

The next picture shows the effect of the centre conductor width, the spacing of the lines is a constant 80 μm while the width ranges from 25 up to 75 μm. The latter already shows limited signs of non-quasi-TEM behaviour. Again the same behaviour for the reflection and transmission coefficients is observed.

Reflection   Transmission
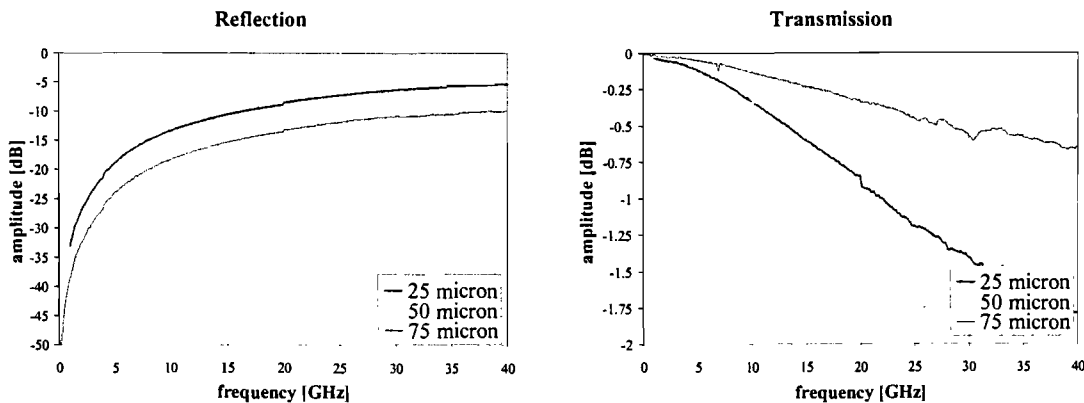
Figure 5.2 Effect of scaling of the centre width on the through structure.

It can be observed that the reflection decreases with increasing width, while the transmission scales with centre conductor width. Again this can be expected since an increase in centre conductor width causes a decrease in characteristic impedance and thus a decrease in reflection coefficient, for impedances larger than 50 Ω. Again the influence of the pad structure is neglected.

5.3 Capacitance measurements and simulations

5.3.1 Capacitance measurements using the HP 4275A

Before a sample is measured the HP 4275A is calibrated. This is done on an open part of the sample. The measured capacitance of the probe on the AlN is approximately equal for the different substrates, which is important since the largest line lengths are located on a separate sample. If a discrepancy was found, the through structure on one sample could not have been used to de-embed the large line located on another.

After calibration all the lines on a particular sample are measured. This routine is repeated until all samples have been measured. The capacitance of a line segment is now calculated by subtracting the line measurement and the appropriate through measurement. This method has the advantage that any offset introduced during the calibration is subtracted from the line capacitance together with the pad capacitance.

The measured capacitance values are corrected for pad structure capacitance and systematic errors by subtracting the pad capacitance from the remaining four lines. After this step a simple curve fit through the origin is used to extract the capacitance per unit length.

The measured values for the capacitance per unit line length are presented in the table below:

Table 5.3 Capacitance per unit line length as measured with the HP 4275A.

C [pF/m]	Width [μm]					
	25	50	75	100	150	200
10	148.4	179.6	200.7	215.5	236.8	244.0
20	115.7	142.4	161.3	172.7	191.8	200.8
40	91.1	111.7	125.0	138.5	150.4	160.1
80	68.8	85.9	97.1	104.3	117.5	124.7
160	52.6	63.4	75.8	82.0	87.1	92.9
320	38.4	45.8	50.6	55.0	59.8	64.5

(Row labels at left: Spacing [μm])

A three dimensional plot of the capacitance values is presented below. It clearly shows a decreasing capacitance for an increasing spacing while the capacitance increases with width.
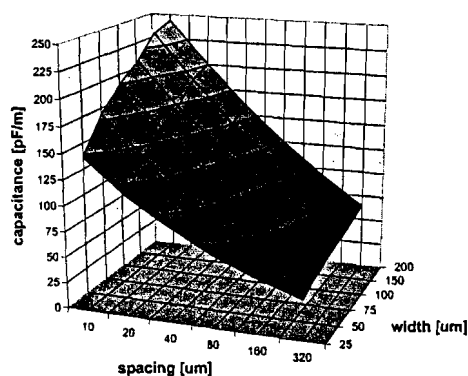

Figure 5.4 Measured capacitance as a function of width and spacing.

To test reproducibility a single, nominal, structure was probed and measured thirty times. After each measurement the probe was lifted and displaced in both the x and y direction. The probe placement was rough, to provide a larger than normal deviation so an upper bound limit on the deviation could be found. This measurement showed a mean value of 62.4 fF and a standard deviation of 0.3 fF, the most extreme measurements were 63.2 fF on the high and 61.9 fF on the low side.

5.3.2 Capacitance calculations based on conformal mapping

This section will present the results of the conformal mapping algorithm proposed by Heinrich and Williams [7,13]. The first method that was implemented was the quasi-TEM description provided by Heinrich, which resulted in the table shown below:

Table 5.4 Capacitance per unit line length as calculated using the quasi-TEM description of Heinrich.

C [pF/m]		Width [μm]					
		25	50	75	100	150	200
Spacing [μm]	10	144.5	178.1	200.1	216.4	240.2	257.3
	20	114.2	142.4	161.7	176.4	198.4	214.8
	40	91.3	113.4	129.1	141.6	160.9	175.6
	80	74.1	90.8	103.0	112.9	128.7	141.2
	160	61.1	73.8	83.0	90.5	102.8	112.7
	320	51.2	60.9	67.9	73.6	82.9	90.4

It can be seen that the method of Heinrich shows a division of the structures, which is in accordance with the expected division based on the assumption of an infinite substrate thickness, as presented in Table 5.2.

The second algorithm that was implemented is based on a method by Williams, which was intended for multilayer substrates, produces the capacitance values presented below:

Table 5.5 Capacitance per unit line length as calculated using the quasi-TEM description of Williams.

C [pF/m]		Width [μm]					
		25	50	75	100	150	200
Spacing [μm]	10	140.4	173.7	194.7	209.6	229.6	242.0
	20	111.9	139.4	157.6	170.8	188.9	200.3
	40	89.4	110.5	125.0	135.8	150.7	160.3
	80	71.5	86.9	97.4	105.4	116.4	123.4
	160	56.1	66.7	73.7	78.9	86.0	90.4
	320	41.0	47.1	51.3	54.5	59.0	61.5

The method should be able to give an accurate estimate for the larger structures, and an improvement can be observed for that aspect. The majority of the capacitance values falls well within a 2.5 % error boundary.

The measured capacitance shows good agreement with respect to the expectations based on conformal mapping, which indicates that the extraction method based on measurements is acceptable.

The formula below is the result of a curve-fit on the measured capacitance data :

$$C = \varepsilon_0 \frac{\varepsilon_r + 1}{2} \frac{K(k_1)}{K'(k_1)} \alpha_{width} \alpha_{spacing} \qquad [5.1]$$

with

$$\alpha_{width} = -4.62\,10^{-6} W^2 - 6.87\,10^{-4} W + 4.20 \qquad [5.2]$$

$$\alpha_{spacing} = 1.05\,10^{-6} S^2 - 1.20\,10^{-3} S + 1.00 \qquad [5.3]$$

The equation for the elliptic integral, $K(k_1)$, was borrowed from Heinrich [7] while the two fitting terms, α_{width} and $\alpha_{spacing}$, were introduced to achieve an acceptable fit with the measured data. This equation is able to predict the capacitance of any line within 2 percent, while the majority remains well below 1 percent.

5.4 Extracted pad structures

Three methods were identified that could be used to extract the pad structures from the measurements, an initial study showed that the LRL method should be the most stable method. To see how the methods perform for a real structure all three methods were performed on an average measurement. This resulted in almost identical curves, with only a few structures showing deviating behaviour for the alternative algorithm. This would indicate that all algorithms could be used to extract the pad-structure.

In case the alternative algorithm is used, the influence of the characteristic impedance can be taken into account. Resulting in pad structures referenced to 50 Ω at both sides, which is easy for comparison. An overview of the influence of the spacing on the extracted pad structure is presented below:
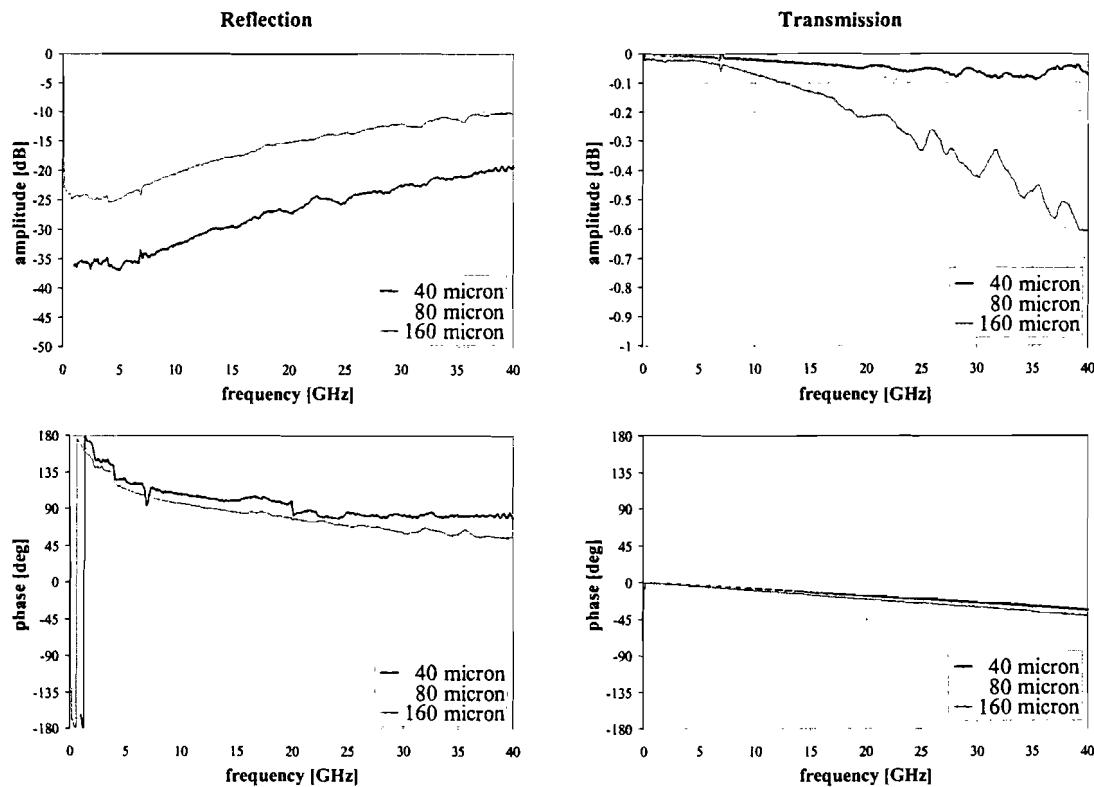

Figure 5.1 Influence of spacing on the extracted pad structure.

The pad structures shown above are obtained from the transmission lines with a width of 100 μm, a length of 800 μm while the different values for the spacing are 40, 80 and 160 μm respectively. With increased spacing an increased reflection combined with decreased transmission is observed, this could be expected since the characteristic impedance of the lines increases from 50 Ω upwards.

The pictures below present an overview of the influence of line width on the extracted pad structure:
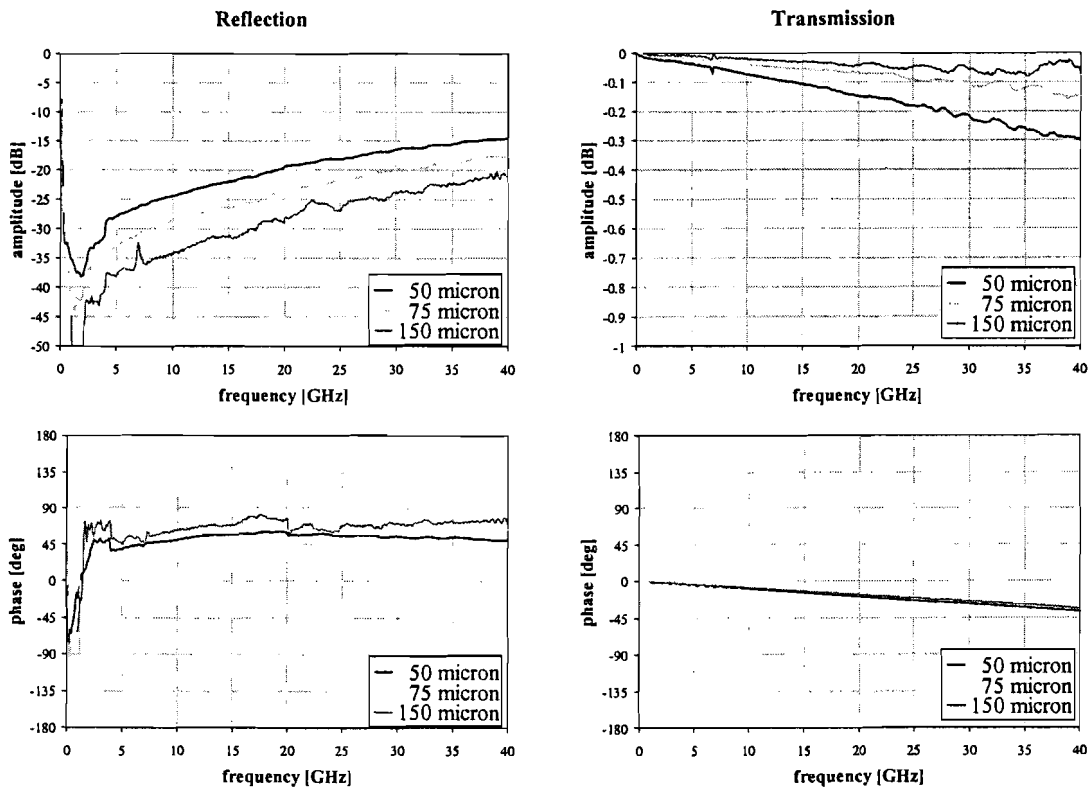

Figure 5.6 Influence of width on the extracted pad structure.

The pad structures shown above are obtained from the transmission lines with a spacing of 40 μm, a length of 800 μm while the different values for the width are 50, 75 and 100 μm respectively. With increased spacing a decreased reflection combined with an increased transmission is observed, this could be expected since the characteristic impedance of the lines decreases.

5.5   Propagation constant extraction

A lot of emphasis has been placed on the fact that the pad discontinuities need to be accounted for in case a measurement based modelling approach were to be chosen. However it has not been shown what influence the pad structure has on for example a line. To demonstrate this influence the picture below shows the propagation constant extracted directly from the measurement and after de-embedding. The line has a width of 50 µm, a spacing of 80 µm and a length of 800 µm.
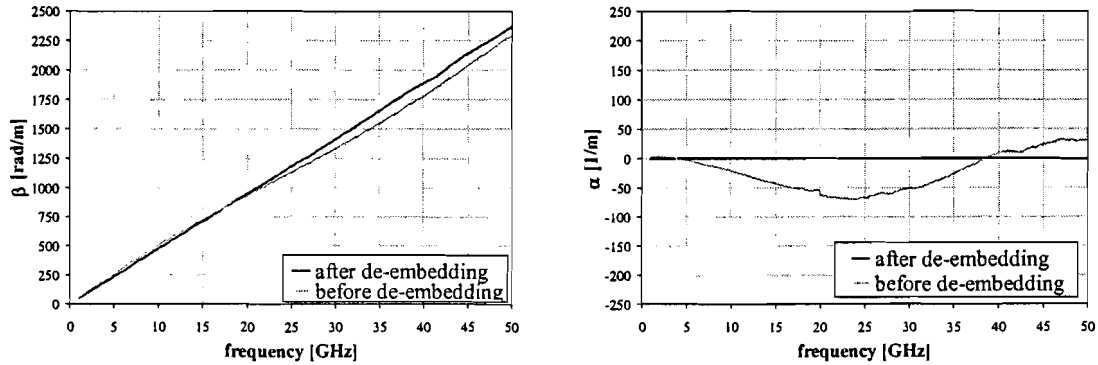

Figure 5.7 Example of the influence of de-embedding on the propagation constant of a standard line structure.

This figure clearly illustrates the need for a de-embedding algorithm, since the dispersion would have been overrated in case no de-embedding algorithm would have been used. For the extraction of the propagation constant two extraction algorithms have been implemented. The first is a part of the LRL algorithm while the second uses an actual de-embedding technique.

In case the de-embedding algorithm is used, the propagation constant can be extracted from a series of lines with varying length, the combined data from these lines can then be used to get a better estimate for the propagation constant. The results for a line with a width of 50 µm and a spacing of 80 µm are presented:
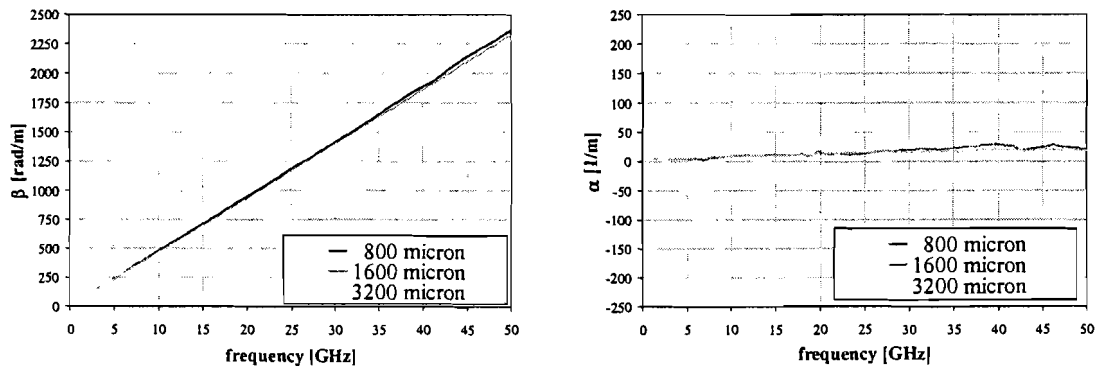

Figure 5.8 Example of the scaling of the propagation constant with line length.

It can be observed that there is a small difference between the different lines. The longer line lengths seem to lead to straighter propagation constant curves, which can be expected since the longer lines show a larger phase shift. It can be noted that the extraction of the propagation constant would benefit from using the longest line available.

In the presentation of the measurement results a distinction was made between the elements which showed quasi-TEM behaviour and elements which showed deviating behaviour. The same distinction can be made for the extracted propagation constants. A line with a width of 75 μm and a spacing of 80 μm and a line with a width of 200 μm and a spacing of 320 μm yield the curves shown below:
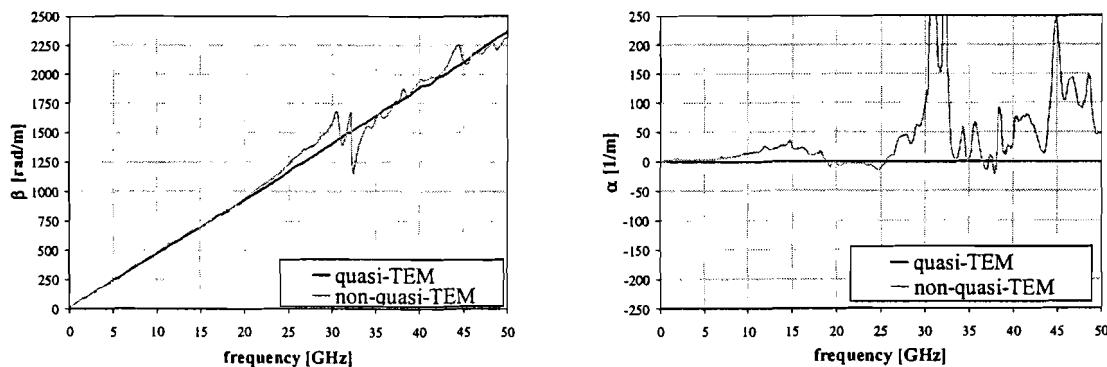

Figure 5.9 Example of the propagation constant of two standard line structures.

The figure on the right clearly shows the same distortion as was found in the measurements, indicating this effect is not caused by pad parasitics. Again the distribution is in agreement with the limits proposed in [7].

The graph below shows the extracted propagation constant for different width and spacing values. The figure on the left has a constant spacing of 80 μm, a length of 3200 μm and widths of 25, 75 and 150 μm. The figure on the right has a constant width of 75 μm, a length of 3200 μm and a spacing of 10, 40 and 160 μm.
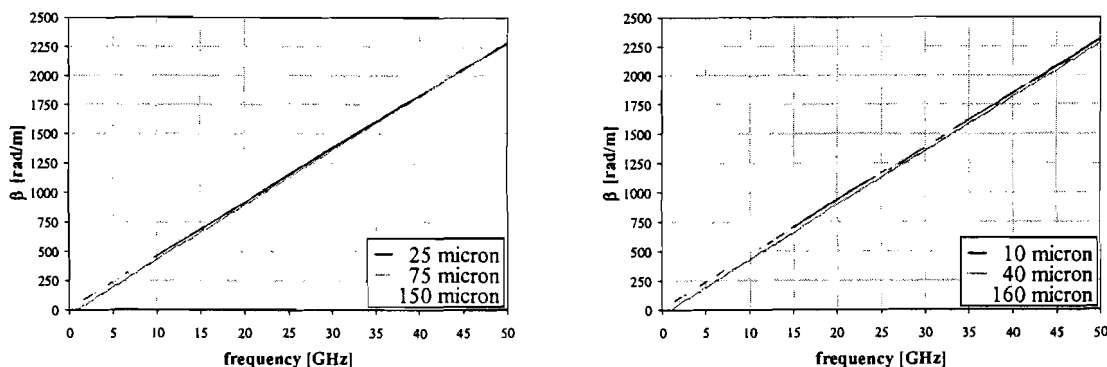

Figure 5.10 Example of the propagation constant dependency on line width (left) and spacing (right).

To increase the efficiency of the curve fitting, the propagation constant will be extracted using the effective dielectric constant which can be defined by:

$$\varepsilon_{\text{eff}} = \left(\frac{\beta c}{2\pi f}\right)^2 \approx \frac{\varepsilon_r + 1}{2} \approx 5$$ [5.4]

Where c models the speed of light. For a lossless transmission line the dielectric constant should be independent of frequency, which results in an easy fit. The curves on the next page show a cross section of the effective dielectric constants, the samples on the left are taken from 25, 75 and 150 μm wide lines while pictures on the right represent 10, 80 and 160 μm spacing.
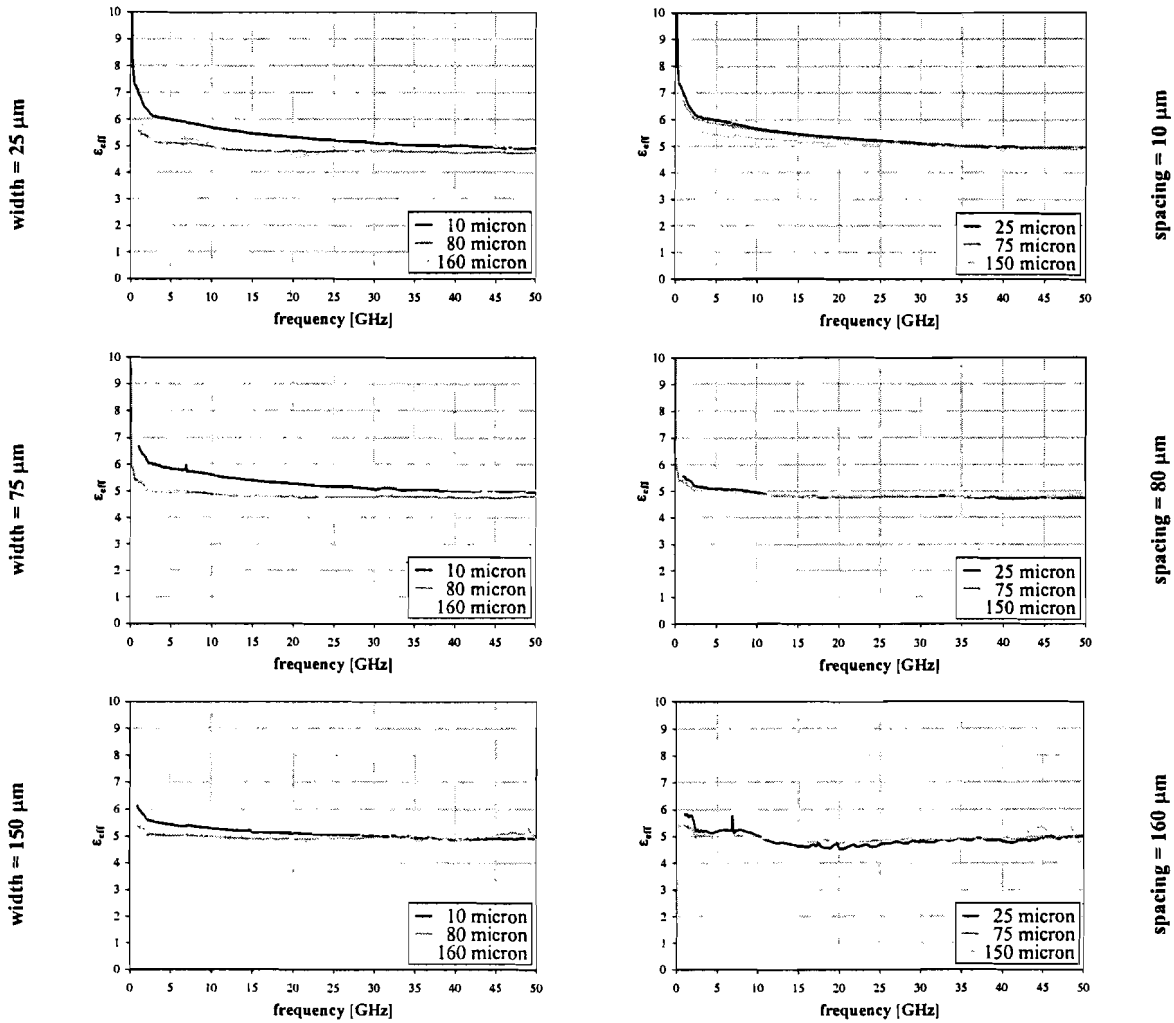
Figure 5.11 Examples of the extracted effective dielectric constants.

The extracted effective dielectric constants, depicted above, show deviating behaviour for structures with large spacing values and higher frequencies. This can be explained by the fact that the basic coplanar mode is no longer the dominant mode and higher order modes cause distortion above 20 GHz. The other behaviour that can be noticed is that the low frequency behaviour is dominated by dispersion.

The table below shows the result of extracting the propagation constant, frequencies below 10 GHz were ignored and the data from lines with a length of 800, 1600 and 3200 µm were combined to obtain this result.

Table 5.5 propagation constant per unit line length and frequency.

β 10^{-9} [m^{-1}Hz^{-1}]		Width [µm]					
		25	50	75	100	150	200
Spacing [µm]	10	46.02	45.85	46.36	45.25	45.40	45.18
	20	45.32	45.77	45.83	45.11	45.53	45.76
	40	45.27	46.62	45.70	46.37	45.99	46.54
	80	45.33	45.37	45.67	46.23	46.68	46.78
	160	46.11	45.75	45.90	46.66	46.79	47.33
	320	46.39	46.79	47.07	47.20	48.77	48.44

The next step is to fit some formula to the extracted data, however 95 % of the extracted propagation constants are within 2 % of a value of 46.17, which means that a constant value would yield an acceptable fit.

A comparison with a commercial transmission line calculator, TXLine[2] from Microwave Office, resulted in the table below. The larger spacing values are not supported by this software and are thus left out.

Table 5.7 Propagation constant per unit line length and frequency generated by microwave office.

$\beta\ 10^{-9}\ [m^{-1}Hz^{-1}]$		Width [μm]					
		25	50	75	100	150	200
Spacing [μm]	10	46.40	46.42	46.43	46.45	46.51	46.58
	20	46.41	46.43	46.46	46.49	46.56	46.66
	40	46.44	45.47	46.51	46.55	46.66	46.78
	80	46.51	46.57	46.63	46.69	46.84	47.00
	160	x	x	x	x	x	x
	320	x	x	x	x	x	x

The propagation constant obtained using this transmission line calculator shows little width and spacing dependency. The total range of propagation constant values lies within 1 percent of 46.7 rad/m at 1 GHz. The extracted propagation constant can be approximated by a mean value of 46.2 with an overall error of a couple of percent, the plots below show the extracted propagation constant and the propagation constant obtained using TXLine. The scale has been adjusted to zoom in to the covered range.
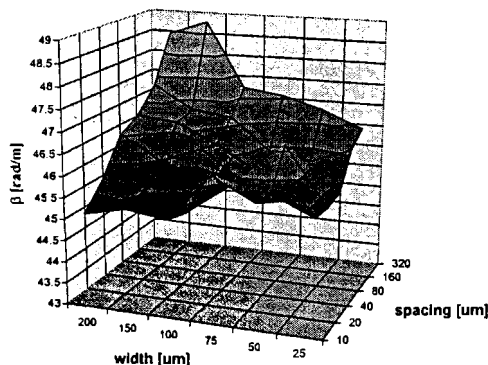

Figure 5.12 Extracted propagation constant as a function of width and spacing.

The agreement between the propagation constant obtained using TXLine and the extracted propagation constant is acceptable.

The second verification is based on the conformal mapping algorithm proposed by Heinrich. This algorithm has been modified in such a way that it uses the measured instead of the calculated capacitance values, to account for the back plane influence.

Table 5.8 Propagation constant per unit line length and frequency using the description of Heinrich.

$\beta\ 10^{-9}\ [m^{-1}Hz^{-1}]$		Width [μm]					
		25	50	75	100	150	200
Spacing [μm]	10	47.10	46.49	46.37	46.20	45.97	44.58
	20	46.58	46.18	45.68	45.75	45.46	44.00
	40	45.83	45.81	45.45	45.72	44.72	43.59
	80	44.24	44.81	44.85	45.33	44.30	43.17
	160	42.07	42.61	42.85	44.91	42.59	42.02
	320	39.05	39.65	39.89	43.43	39.31	39.29

Again the same distribution as presented in Table 5.2 can be observed. Indicating proper extraction of the propagation constant for the smaller structures.

---

[2] TXLine version 1.1. copyright Applied Wave Research Inc. 1996.

5.5.1 Characteristic impedance extraction

Finally the characteristic impedance values can be determined based on the extracted propagation constants and the measured capacitance values. Due to the fact that the attenuation of the transmission lines has not been investigated only the real part of the characteristic impedance, presented below, is determined:

Table 5.9 Propagation constant per unit line length and frequency.

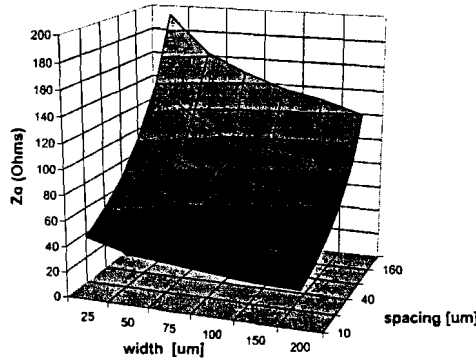| Z_0 [Ω]		Width [μm]					
		25	50	75	100	150	200
Spacing [μm]	10	49.4	40.6	36.8	33.4	30.5	29.5
	20	62.3	51.2	45.2	41.6	37.8	36.4
	40	79.1	66.4	58.2	53.3	48.7	46.3
	80	104.9	84.1	74.9	70.5	63.2	59.7
	160	139.5	114.9	96.4	90.6	85.5	81.1
	320	192.3	162.6	148.0	136.6	129.8	119.5

Figure 5.13 Extracted characteristic impedance as a function of width and spacing.

Instead of performing a curve-fitting algorithm on the extracted characteristic impedance, an equation is determined based on the fit for the propagation constant and the transmission line capacitance. This results in the equation presented below:

$$Z_0 = \frac{\gamma}{\omega C} \approx \frac{46.2}{\pi \varepsilon_0 (\varepsilon_r + 1)} \frac{K'(k_1)}{K(k_1)} \frac{1}{\alpha_{width} \alpha_{spacing}} \qquad [5.5]$$

where α_{width} and $\alpha_{spacing}$ are derived from the capacitance formula. The formula illustrates it's derivation based on the propagation constant and a transmission line capacitance. The same methods can be applied to extract an approximate formula for the inductance per unit line length.

$$L = \frac{\gamma^2}{\omega^2 C} \approx \frac{1067}{\pi^2 \varepsilon_0 (\varepsilon_r + 1)} \frac{K'(k_1)}{K(k_1)} \frac{1}{\alpha_{width} \alpha_{spacing}} \qquad [5.6]$$

A comparison between the extracted characteristic impedance and the characteristic impedance that is obtained using the algorithm proposed by Heinrich results in the table below:

Table 5.10 Characteristic impedance generated by Heinrich.

Z_0 [Ω]		Width [μm]					
		25	50	75	100	150	200
Spacing [μm]	10	48.0	39.4	35.2	32.7	29.6	27.7
	20	61.5	49.9	44.2	40.6	36.2	33.5
	40	77.9	63.3	55.8	51.0	45.0	41.3
	80	96.7	79.6	70.4	64.3	56.6	51.7
	160	117.8	98.4	87.7	80.5	71.1	64.9
	320	140.9	119.4	107.5	99.3	88.4	81.1

Again the quasi-TEM distribution can be observed, indicating that the extracted characteristic impedance is accurate for the smaller structures. As a second verification tool the extracted characteristic impedance is compared with the results from the commercial TXLine, the results are presented below.

Table 5.11 Characteristic impedance generated by microwave office.

Z_0 [Ω]		Width [μm]					
		25	50	75	100	150	200
Spacing [μm]	10	48.9	40.6	36.5	33.8	30.5	28.4
	20	65.3	54.7	49.0	45.4	40.7	37.7
	40	82.2	69.6	62.5	57.8	51.5	47.5
	80	99.3	85.4	77.2	71.5	63.8	58.7
	160	x	x	x	x	x	x
	320	x	x	x	x	x	x

The table shows the results using halve the width due to a bug in the algorithms used by TXLine. Applied wave research has been contacted about the topic and they confirmed the bug in the software and are currently looking into the problem.

Finally a comparison between the extracted characteristic impedance and the characteristic impedance that is obtained using the finite grounded coplanar waveguide transmission line in MDS:

Table 5.12 Characteristic impedance generated by MDS.

Z_0 [Ω]		Width [μm]					
		25	50	75	100	150	200
Spacing [μm]	10	44.0	38.0	34.5	32.5	30.0	28.0
	20	57.0	48.0	43.0	40.0	36.0	34.0
	40	72.5	60.0	53.5	49.5	44.5	41.5
	80	90.5	75.0	67.0	61.5	55.0	51.0
	160	111.5	93.0	83.0	77.0	68.5	63.5
	320	135.5	114.0	103.0	96.0	86.5	80.0

It can be observed that the agreement with MDS is poor, this means that MDS should not be used to estimate the behaviour of a conductor backed coplanar waveguide.

At current no accurate comparison can be made due to the lack of a conformal mapping algorithm and a bug in TXLine. Due to the observed accuracy of both the propagation constant and transmission line capacitance the remaining error observed in the characteristic impedance is accepted for the moment.

5.5.2 De-embedding examples

To demonstrate the use of the de-embedding algorithm, it has been used on the short-circuit and open-circuit structures that were included on the coplanar waveguide mask. The pictures presented on this page are based on a structure with a width of 50 μm and a spacing of 40 μm.

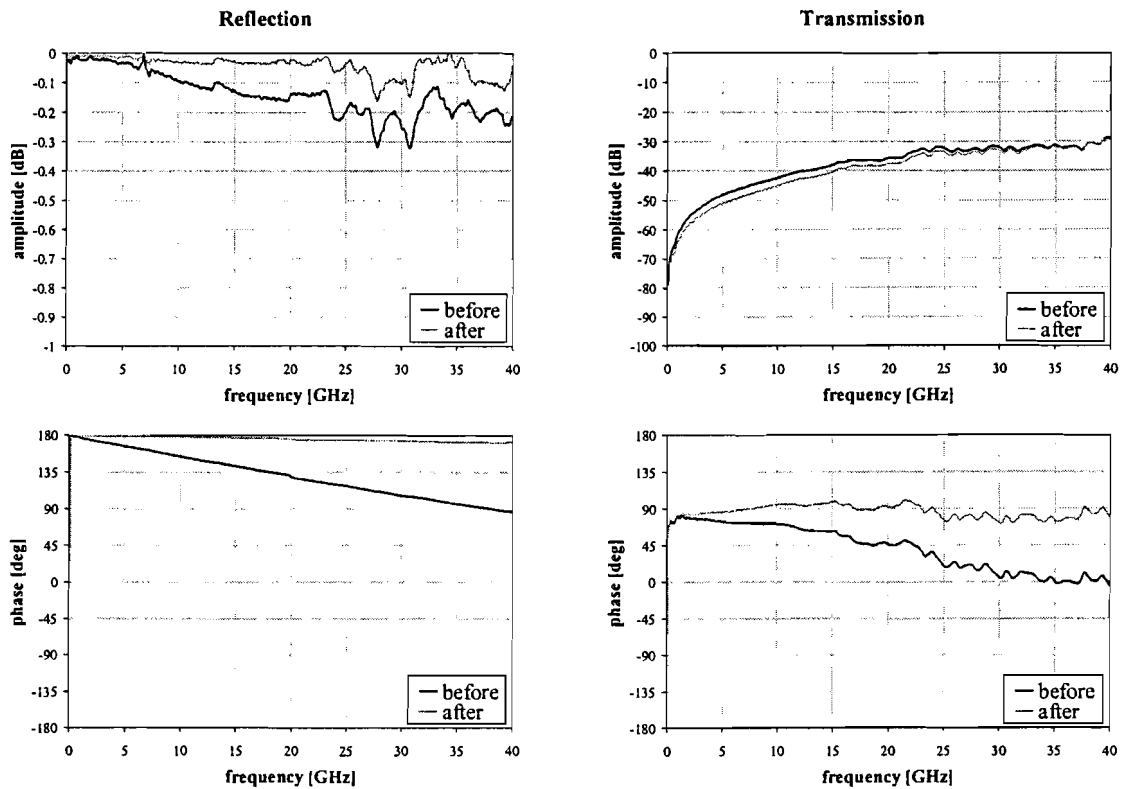**Reflection**   **Transmission**

Figure 5.14 A short circuit before and after de-embedding.

The de-embedded short-circuit shows a small phase shift compared to the original. The remaining phase shift is caused by de-embedding errors and the non-zero length short. A rough estimate of this is obtained by assuming that the remaining equivalent circuit is dominated by an inductor between the signal path and ground. This results in an inductance of approximately 12.5 pH, which is obtained by transforming the de-embedded scattering parameters to Z-parameters and then fitting Z_{11} with a straight curve.

The same principle can be applied to the open circuit, which is available on the same mask. Again a line with a width of 75 μm and a spacing of 40 μm was used.
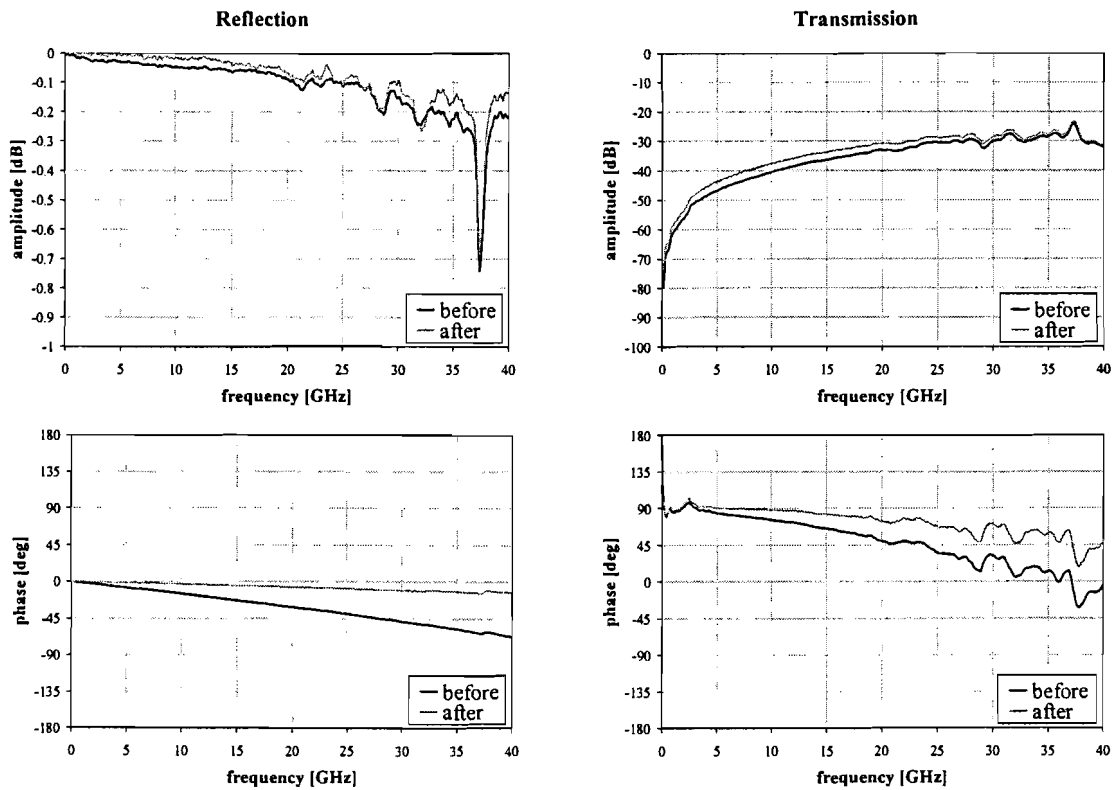
Reflection

Transmission

Figure 5.15 An open circuit before and after de-embedding.

The de-embedded open-circuit again shows a small phase shift, it can be attributed to de-embedding and stray capacitance at the end of the transmission line. A rough estimate of this stray capacitance yields a value of approximately 6.5 fF, which is obtained by fitting Y_{11} with a straight curve.

5.6 Additional tests

This section will look into the influence of backside metalisation and a thicker substrate. Unfortunately these measurements were performed at different locations with a different measurement set-ups.

Before the measurements performed at TNO-FEL and the measurements performed at the TU/e can be compared, a line with a width of 200 μm, a spacing of 320 μm and a length of 3200 μm is compared. The results from this measurement are depicted below.
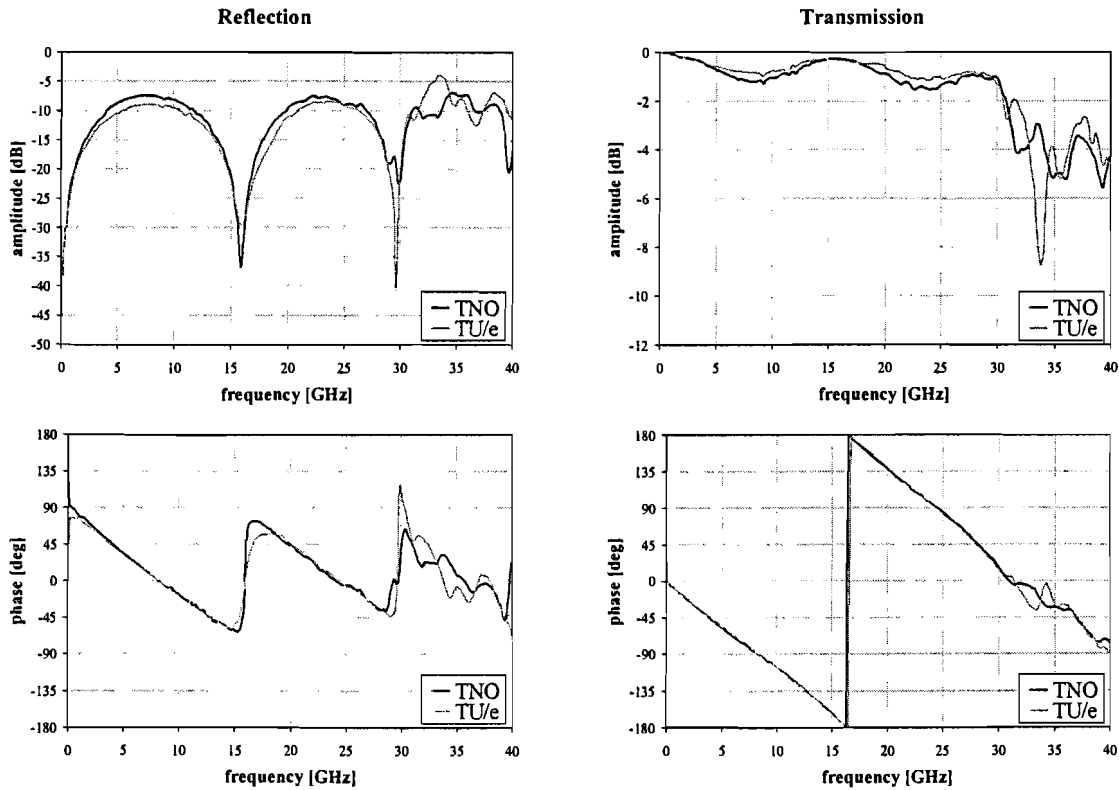

Figure 5.16 Comparison of measurements performed at TNO-FEL and measurements performed at TU/e.

The agreement that can be observed between the transmission and reflection coefficients is acceptable, although the agreement is not ideal. At this moment it is not clear to what effect this difference can be attributed, but it is suspected that the differences could, in part, be caused by the different types of probes used to measure the structures.

5.6.1 Backside metalisation test

The first test involves the influence of a backside metalisation step on the parallel plate modes. Since all measurements are performed on a metal chuck it can be expected that the difference between the two measurements is minimal. A small difference could exist due to the thin layer of air between the sample and the metal chuck. The structure has a width of 200 µm, a spacing of 320 µm and a length of 1600 µm.
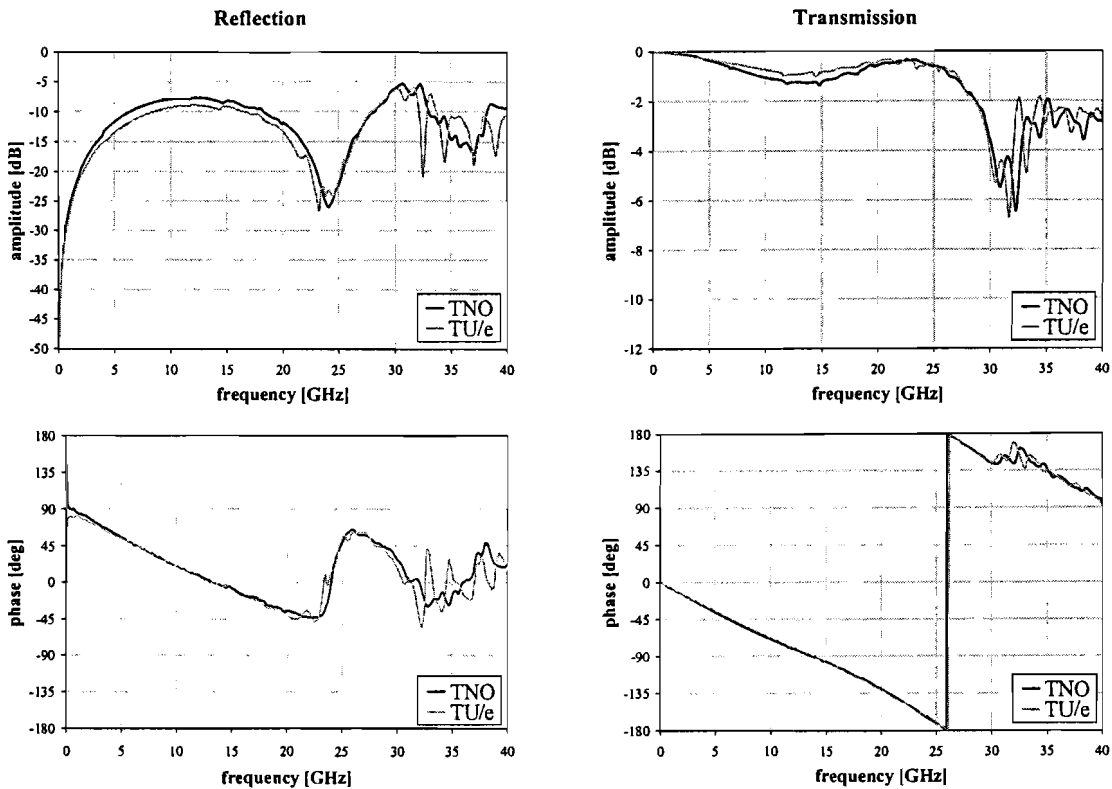

Figure 5.17 Measurements showing the influence of a backside metalisation on a laterally large structure.

As expected the difference between the measurements is minimal. The same difference between the measurements performed at TNO-FEL and the measurements performed at the TU/e can be observed. This effect shows that no significant improvement is observed in case a backside metalisation is applied to the sample, making this additional processing step obsolete.

5.6.2 Substrate thickness tests

Two tests have been performed to check the influence of a thicker substrate on the parallel plate modes. The first test was performed at TNO-FEL. Due to the lack of a thicker substrate a simple plastic cover was used to raise the sample a couple of millimetre into the air. The dielectric constant that is measured now becomes a function of the AlN substrate, the plastic cover and the remaining air under the cover, which means that the frequency between adjacent minima will increase slightly. The measurement depicted is performed on a line with a width of 200 µm, a spacing of 320 µm and a length of 3200 µm.

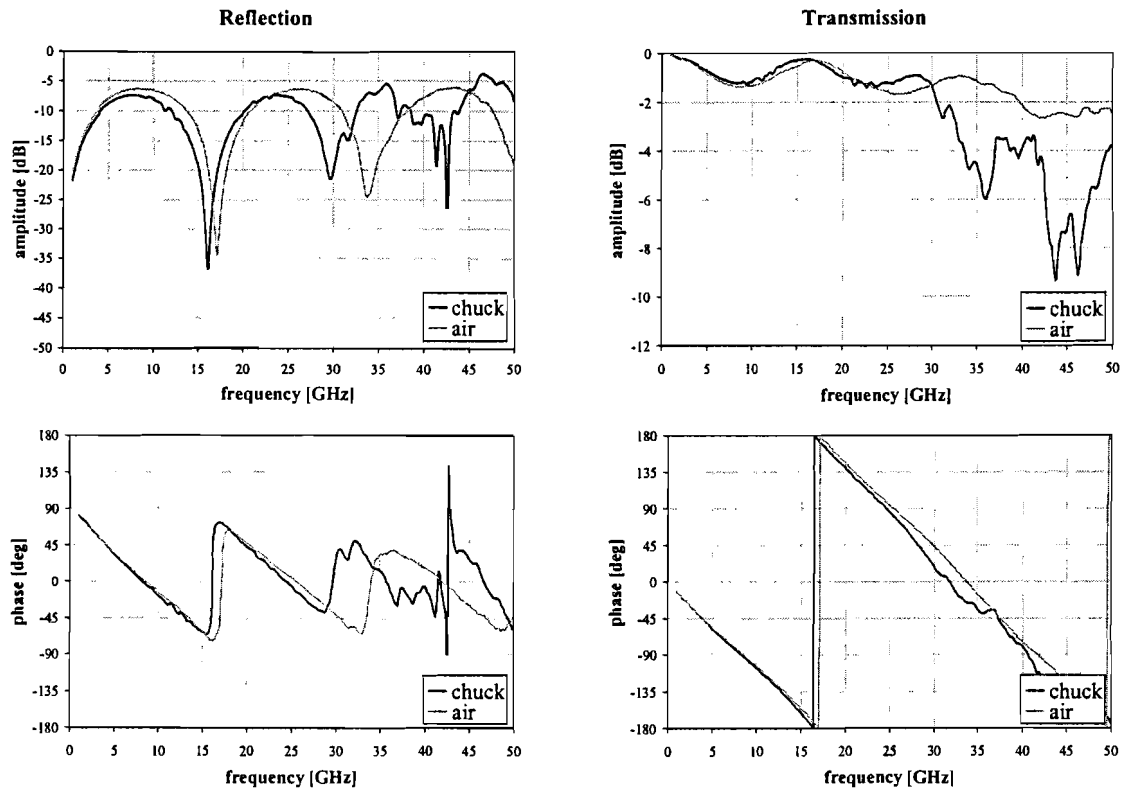**Reflection**   **Transmission**

Figure 5.18 Measurements showing the influence of a raising the sample into the air on a laterally large structure.

The result of the increased sample thickness is remarkable. The effect of the parallel plate mode has almost completely disappeared. The peaks in the single substrate are located at approximately 16, 30 and 42 GHz, after the sample has been raised the peaks are located at 17, 34 and just over 50 GHz. After the substrate was raised the peaks are equidistant while they were not before. This is another indication that the effect observed is not a function of the pad structures but has to do with parallel plate modes.

The influence of raising the substrate was clear, but it is important to study the influence of substrate thickness. Since acquiring a set of substrates with increasing thickness is not an option, the increasing substrate thickness was realised by stacking multiple samples without metalisation under the sample under test. The measurement depicted is performed on a line with a width of 200, a spacing of 320 and a length of 3200 µm.
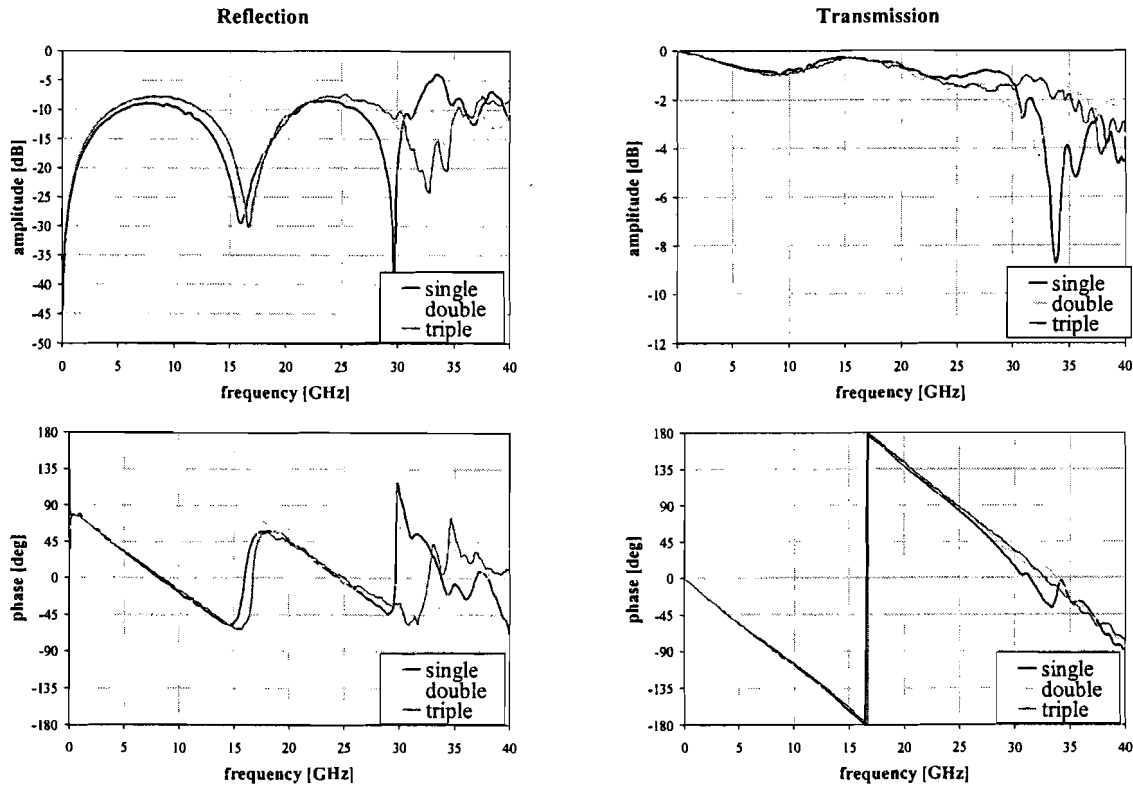
Figure 5.19 Measurements showing the influence of an increased substrate thickness on a laterally large structure.

The measurements depicted above present the results of increasing the substrate thickness, the first measurement was performed on a standard sample, the second measurement featured a double substrate and the third measurement had two substrates stacked under the sample.

The results of this test are promising, the peak at 30 GHz, present in the original measurements, is gone in the second and third measurement. In the third measurement the second minimum in the reflection is visible at approximately 33 GHz, which corresponds with the first minimum at 16.5 GHz. However the distortion at the higher frequencies remains.

A further increase of a stack of three substrates to a stack of five substrates shows no further improvement. Which might indicate that the remaining distortion is, in part, caused by the stack itself. Due to the fact that the substrates don't form one uniform substrate and air is thus still present between the samples, some distortion might be caused by the stack itself, this can only be tested by processing a thick sample.

5.7 Results and conclusions

This section introduces the results, which were obtained, from the measurements and the related experiments.

Measurement results

The measurements show a clear distinction between structures showing behaviour, which is in agreement with the expected curves and transmission lines showing non-quasi-TEM behaviour. The distribution of the measurements is in agreement with the distribution proposed by Heinrich according to the validity of the quasi-TEM model.

The non-quasi-TEM phenomenon was attributed to higher-order modes after the influence of probe placement and calibration errors was eliminated by repeating previous measurements. The non-TEM effects include a significant decrease in period over frequency and distortion of the measurements at higher frequencies.

Transmission line capacitance

It has been established that the extraction of a transmission line capacitance is essential to extracting valid circuit models. Two approaches have been studied, the first approach is based on measurements while the second approach introduces two conformal mapping algorithms.

The measurement of the transmission line capacitance is based on a HP 4275A LZR meter. The original set-up was modified to support coplanar probes and allow for acceptable measurement accuracy. It has been established that measurements are reproducible to within 1 fF and with a standard deviation of 0.3 fF. The method used the different line lengths for the extraction of the transmission line capacitance per unit length.

Two conformal mapping algorithms have been implemented, which rely on the assumption that the capacitance does not depend on frequency. The conformal mapping algorithms were able to reproduce the measured capacitance values within a 2.5 % error boundary.

Finally a simple design equation based on curve fitting is presented, which is able to reproduce the measured transmission line capacitance values to within a 1 % error boundary.

It has been established that the assumption that transmission line capacitance remains constant as a function of frequency should remain valid down to at least 2 MHz. The agreement between conformal mapping algorithms and measurement results indicates that the capacitance values per unit line length, obtained with the HP 4275 A LZR meter can be used for the characterisation of coplanar waveguide transmission lines .

Pad structure extraction

Three pad structure extraction algorithms, based on the TSD, LRL and an alternative algorithm, were implemented and tested. All algorithms are capable to extract the pad structures from the measurements but prior tests have shown that the LRL algorithm is likely to produce the most accurate results.

With increased spacing the pad structures show an increased reflection combined with a decreased transmission, which can be explained by the increasing characteristic impedance of the lines. For an increasing signal track width the pad structures show a decreasing reflection and an increased transmission, which can be explained by the decreasing characteristic impedance.

The results obtained with the pad extraction algorithms indicate that the pad structures can be extracted in sufficient degree to allow the implementation of a de-embedding algorithm to be useful.

Propagation constant

A de-embedding algorithm based on the LRL pad extraction algorithm was implemented. This algorithm was used to extract the propagation constant of the transmission lines. The de-embedded propagation constants show behaviour, which depends less on frequency, which could be expected.

The de-embedding algorithm was not able to remove the resonant behaviour present on the larger structures. This supports the assumption that the resonant behaviour originates from higher order modes and not from the discontinuities at the pad structure transmission line transition.

The distribution of the extracted propagation constant does not follow a specific trend, which can be explained by the fact that the propagation constant for higher order modes differs from the propagation constant of the basic propagating mode. The quasi-TEM distribution proposed by Heinrich is also valid for the extracted propagation constant.

The extracted propagation constants can be fitted with a constant value of 46.2 introducing a limited error bound. This same behaviour is obtained in case TXLine is used. A comparison with the propagation constant obtained with the conformal mapping algorithm proposed by Heinrich shows an acceptable agreement for the relevant structures.

It has been shown that the propagation constant, which is extracted after de-embedding the transmission lines, shows acceptable agreement with conformal mapping and TXLine. This supports the usefulness of both the pad structure extraction and the de-embedding algorithms.

Characteristic impedance

The characteristic impedance was calculated using the measured transmission line capacitance and the extracted propagation constant. This characteristic impedance was compared with the characteristic impedance obtained using TXLine. A bug was noticed in TXLine, which, at current, limits the usefulness of TXLine. However, it can be assumed that the characteristic impedance is extracted with sufficient accuracy.

Parallel plate modes and backside metalisation

The resonant phenomena have been attributed a higher order parallel plate mode. Some tests were performed which were intended to investigate the influence of substrate thickness and backside metalisation.

The first test used a backside metalisation. This yielded no significant difference implying that the little air that remains between chuck and substrate does not play a significant role.

For the second test a plastic cover was placed between the sample and the chuck. The non-quasi-TEM phenomenon was almost completely removed from the measurement. This would indicate that substrate thickness plays a significant role with respect to the non-quasi-TEM phenomenon.

A third test used a stack of substrates instead of the plastic cover. The number of substrates under the sample was increased to study the phenomenon as a function of substrate thickness. With an increasing number of substrates the periodicity returned and the distortion was reduced. However a completely normal measurement was not obtained, this could be due to the fact that a stack of substrates was used.

6 Simulation results

6.1 Introduction

The previous chapters aimed at circuit models for coplanar waveguide passive components, these models were based on measurements. Another approach, which is gaining a lot of terrain, is extracting the models from electromagnetic simulations. This option has become available due to the progress in numerical methods and increased computing power.

This section will present an initial study, which is based on three commercial electromagnetic circuit simulators, namely HP Momentum, Sonnet EM Suite and HP High-frequency Structure Simulator. The first two simulator are 2.5D, in effect the structures simulated in this type of simulator need to be planar. The latter is a true 3D simulator, this means the complex geometry of the structures can be used in the simulation.

It should be noted that only a limited amount of time has been spent using the simulators. For this reason one should be careful with the conclusions, in effect this means that no direct conclusions have been drawn and the sections contain elements which can be used as a base for further investigation of the structure simulators.

This chapter is divided into sections, which correspond to the different circuit simulators, the chapters will present some of the problems related to using the specific simulator and where possible a solution is presented. Finally some conclusions are presented on the usefulness of the simulations that were performed.

6.2 Sonnet EM Suite

6.2.1 Definition of test structures

This section presents the constants used in Sonnet to define substrate material and metal types.

Dielectric definition

This section will deal with the definition of a single dielectric layer. Sonnet uses a set of parameters to describe the properties of a dielectric layer, the ones needed for the coplanar structures are the thickness of the dielectric layer structure with the relative dielectric constant, ε_r, the dielectric loss tangent, $\tan \delta_e$, and the dielectric conductivity, σ. The combination of relative dielectric constant, dielectric loss tangent and dielectric conductivity is used to calculate a total effective loss tan, which is defined as:

$$\tan \delta_{\text{efectivef}} = \tan \delta_e + \frac{\sigma}{\omega \varepsilon_r \varepsilon_0} \qquad [6.1]$$

Since no magnetic materials will be used, the magnetic parameters, which have not been listed, should be chosen such a way that they don't influence the simulations, in effect they should be left at the default values.

Metal definition

Sonnet EM Suite divides the metalisation losses into DC losses and RF losses, for each type of metalisation loss a correction factor is introduced, R_{DC} for the low frequency losses and R_{RF} for the high frequency losses. A surface reactance can be specified, this surface reactance is meant for super conductor purposes and should not be used for normal operation. For coplanar waveguides the surface reactance will always be set to zero.

The bulk conductivity of the metal used and the cross-section of the metal determine the low frequency losses. Sonnet uses the resistance per square to describe the DC metalisation losses.

$$R_{DC} = \frac{1}{\sigma t} \quad \left(\Omega sq^{-1} \right) \qquad [6.2]$$

Where t is metalisation thickness (m)

The high frequency metalisation losses can be accounted for by specifying the skin effect coefficient R_{RF}. Sonnet multiplies this skin effect coefficient by the square root of the frequency.

$$R_{RF} = \sqrt{\frac{\pi \mu_0}{\sigma}} \quad \left(\Omega Hz^{-\frac{1}{2}} sq^{-1} \right) \qquad [6.3]$$

Below a threshold frequency, F_T, the metal losses are estimated by the DC losses and above this frequency the losses are modelled by the RF losses, the transition region is also modelled accurately.

$$F_T = \left(\frac{R_{DC}}{R_{RF}} \right)^2 \quad (Hz) \qquad [6.4]$$

6.2.2 Sonnet simulation results

First a pad was simulated, which was compared to measurements as presented below:
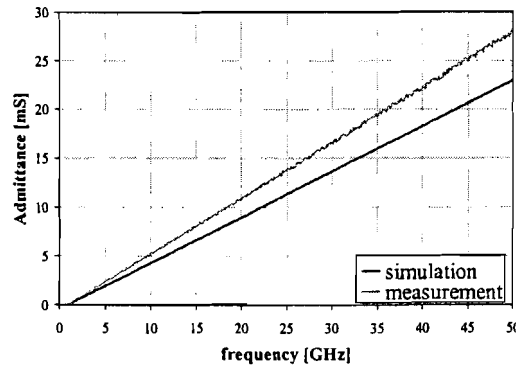

Figure 6.1 Measured admittance of the pad structure versus simulated pad structure.

The figure above presents the admittance of both a measured and simulated pad structure. The measurement yields a capacitance of 4.3 fF while a value of 6.8 fF is obtained from the simulation. A series of simulations was performed to compare measured data to the data generated by Sonnet. The first simulation shows a line with a width of 25 μm, a spacing of 10 μm and a length of 800 μm.
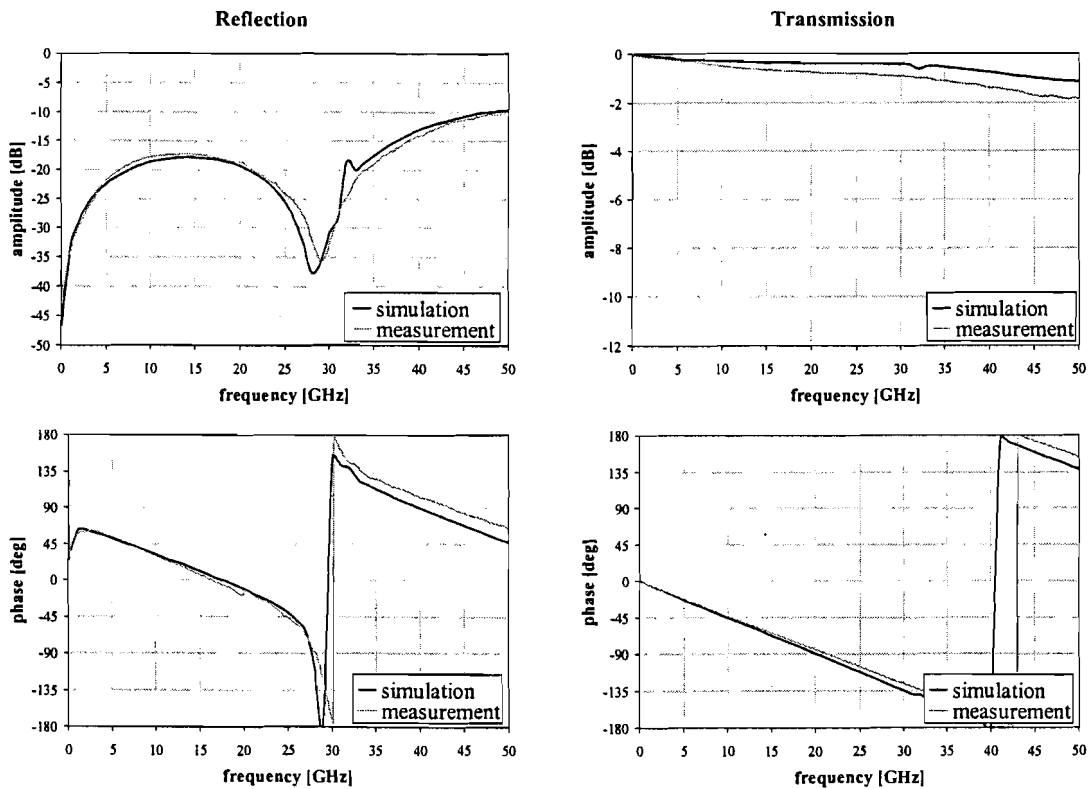
Figure 6.2 Comparison of a laterally small simulated and measured coplanar waveguide.

The graphs present both the measured and simulated transmission and the reflection coefficients. Although the difference is clearly visible, the same trend can be observed in both curves.

The simulation shows a resonance at approximately 32 GHz, while no box resonance error was generated. A box resonance is a resonance, which is caused by the fact that a standing wave can occur within the bounding box. The reason for the peak is not fully understood. A thorough simulation of this frequency spectrum showed that the peak was not a single sample but that the effect was a true result from the simulation. Although Sonnet did not detect a box resonance it could be a remnant from one that was eliminated.

Another structure that was simulated using Sonnet is the largest line, which has a width of 200 μm, a spacing of 320 μm and a length of 800 μm. The results of this simulation are presented below:
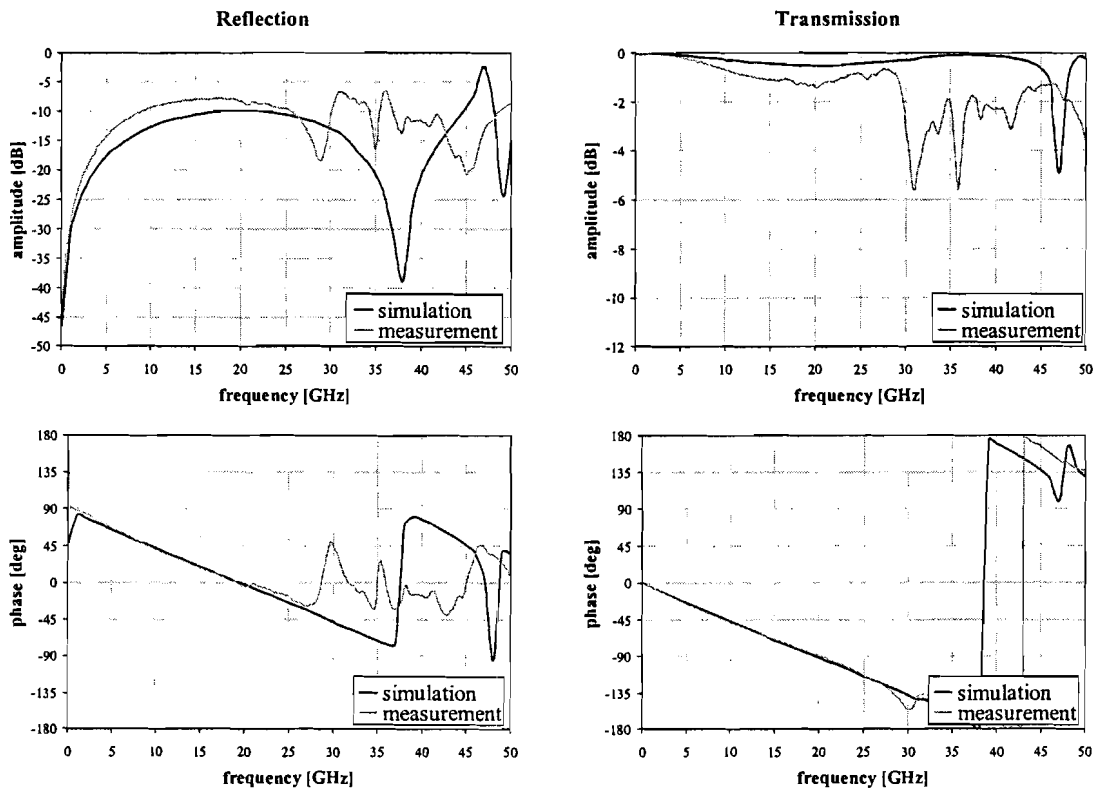
Figure 6.3 Comparison of a laterally large simulated and measured coplanar waveguide.

These simulations show a larger deviation for the magnitude of both the transmission and reflection coefficients, the phase shows a good agreement up to 25 GHz. At this point the measurements shows the effects of the higher order parallel plate modes while the simulation does not, as expected. The resonance peak in this structure is a box resonance, this resonance could not be eliminated.

The following page shows a simulation of a 250 μm wide open circuit with a width of 200 μm and a spacing of 320 μm. While a second simulation shows a 250 μm wide open circuit with width of 25 μm and a spacing of 10 μm. The fit between the measured and simulated data is acceptable, especially for the open structure.

Another thing, which can be noticed, is that the short circuit transmission shows the same kind of parallel plate distortion as the larger structures. This distortion is present at the point that the measured transmission already starts to rise to reasonable values. The difference between the measured and simulated transmission for the open structure can, in part, be explained by the fact that the measured signal is well below the calibration level.

The simulation results for the open and short-circuit mentioned on the previous page are presented below:
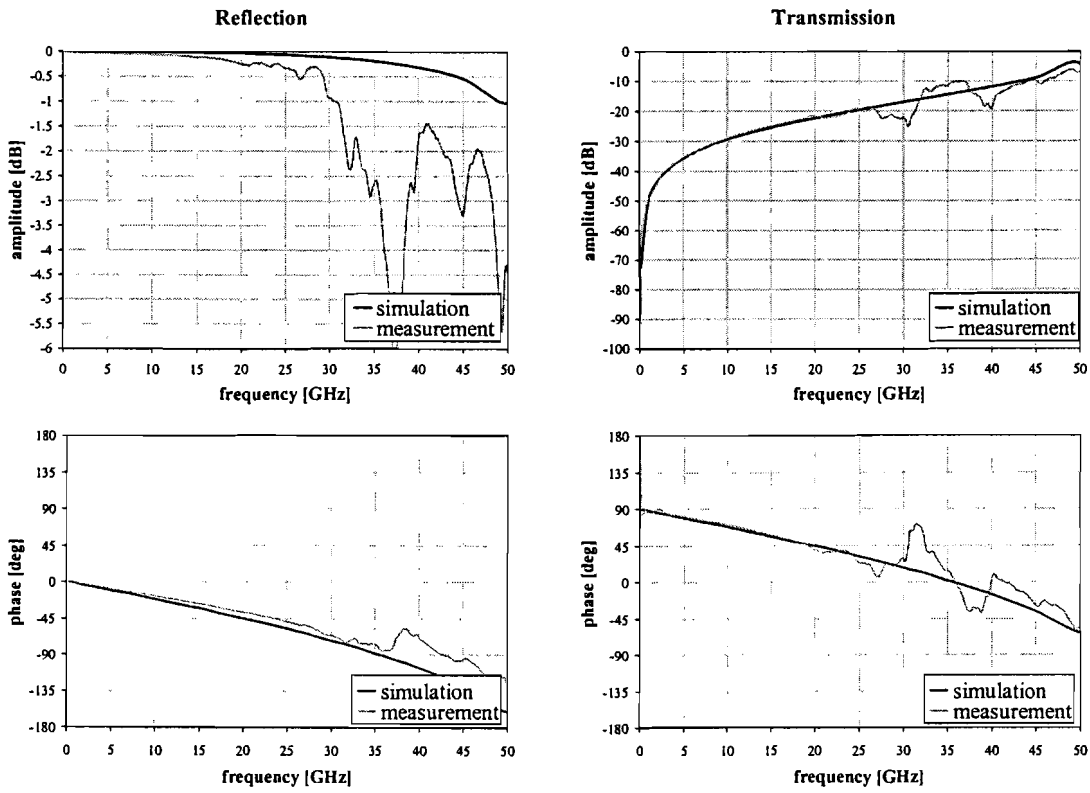
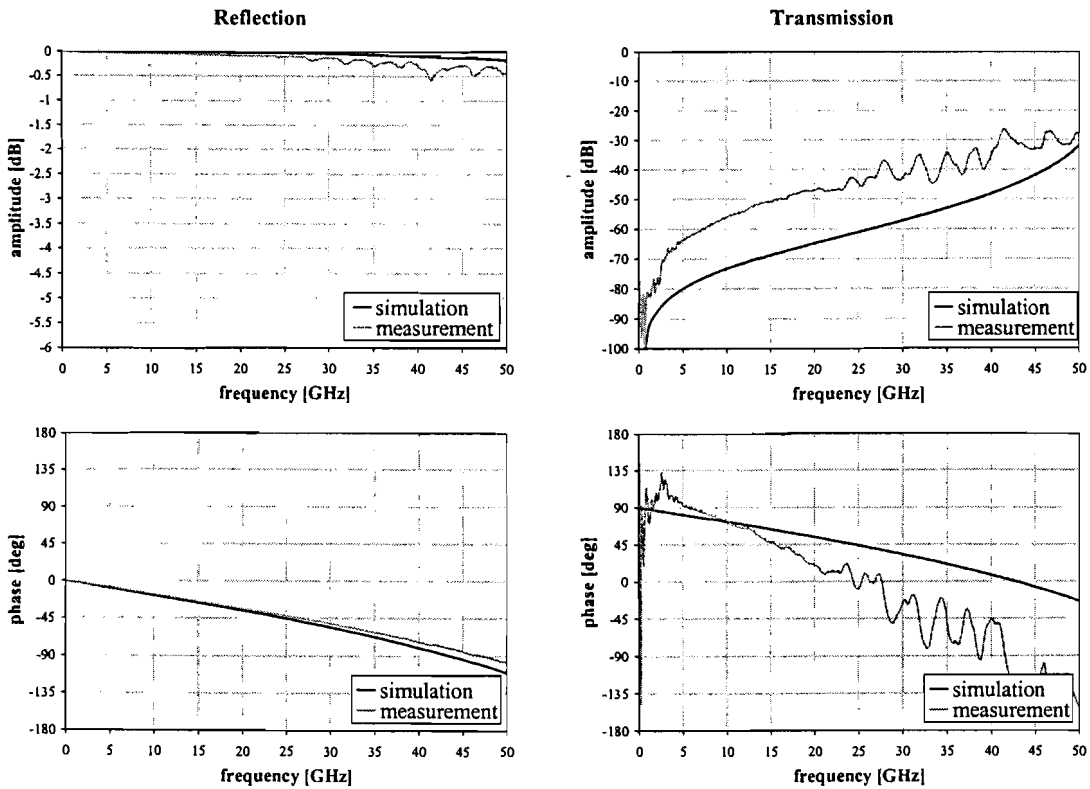**Figure 6.4 Comparison of a laterally large simulated and measured coplanar open-circuit.**

Figure 6.5 Comparison of a laterally small simulated and measured coplanar short-circuit.

6.3 HP Momentum

6.3.1 Description of the settings for the test structures

The material parameters as described in the list of constants section have been used to define the substrate and metalisation in momentum. The bottom of the substrate was defined to have a gold ground-plane, this way the grounded coplanar waveguide geometry was inherently included in the simulations.
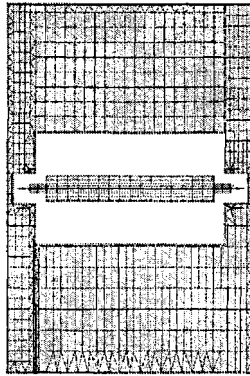
Figure 6.6 Example of the coplanar waveguide simulation structure used in Momentum.

One of the remaining problems in momentum is the definition of the coplanar waveguide structure. Coplanar waveguides can be defined by the slots in the metal or by the metal surface itself, the method preferred in momentum is to use slots. Due to the finite ground of the coplanar waveguides used, this method is not ideal.

To transform the simulated six-port data to the required two-port data, an additional simulation step in ADS is used. This step reads the six-port data and then combines the six-port data into two-port data. The first step is to connecting both ground ports, next a transformer is used to create a new ground while the ground used for the six ports is left floating. A simple circuit using this principle is shown below:
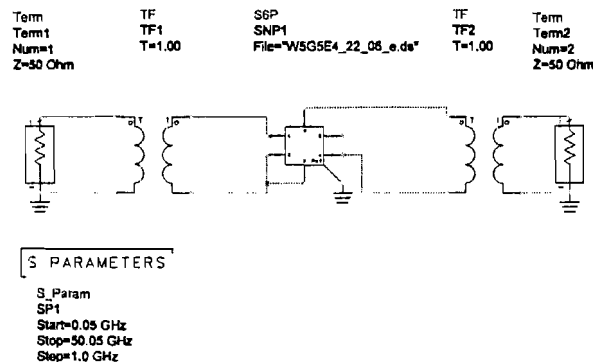

Figure 6.7 Example of a the conversion from 6-port to 2-port data.

Two results of the simulations performed with Momentum are presented on the following page. Both simulations are performed on a structure with a width of 25 µm and a length of 800 µm, the spacing are 10 and 320 µm respectively. The larger structure shows a good fit with the measured data, this is not the case for the smaller structure. This could be caused due to the fact that strips, which are not intended for tightly spaced lines, are used instead of slots.
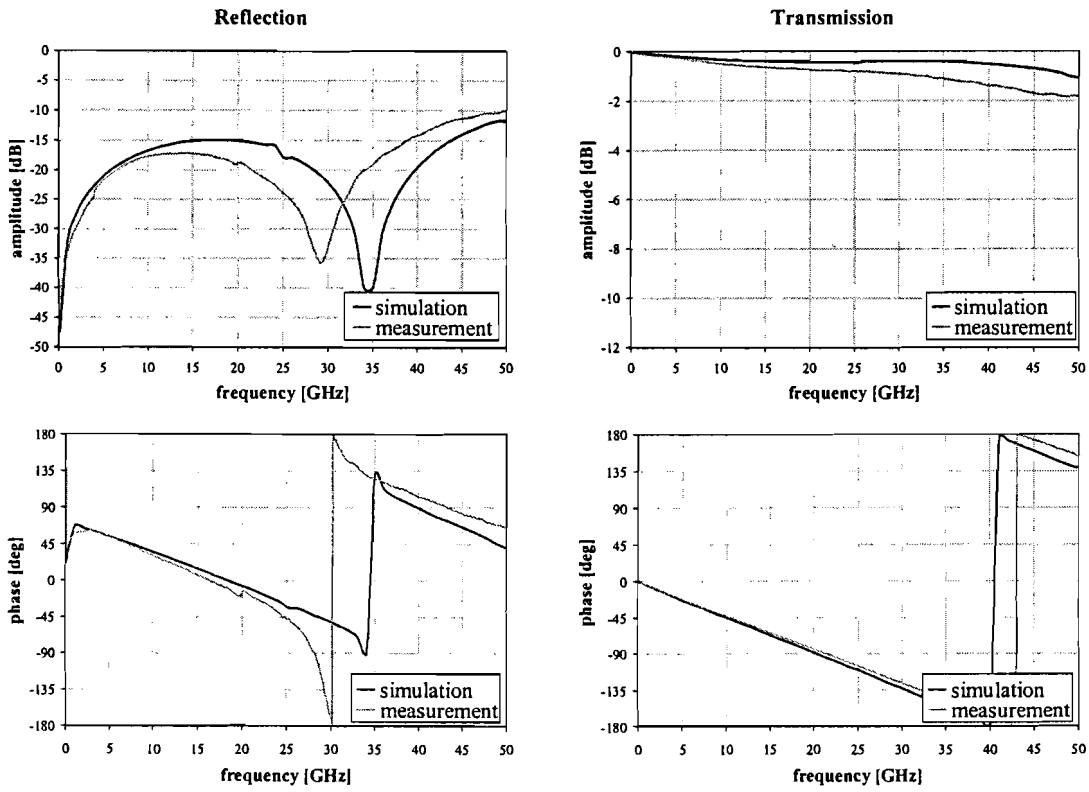
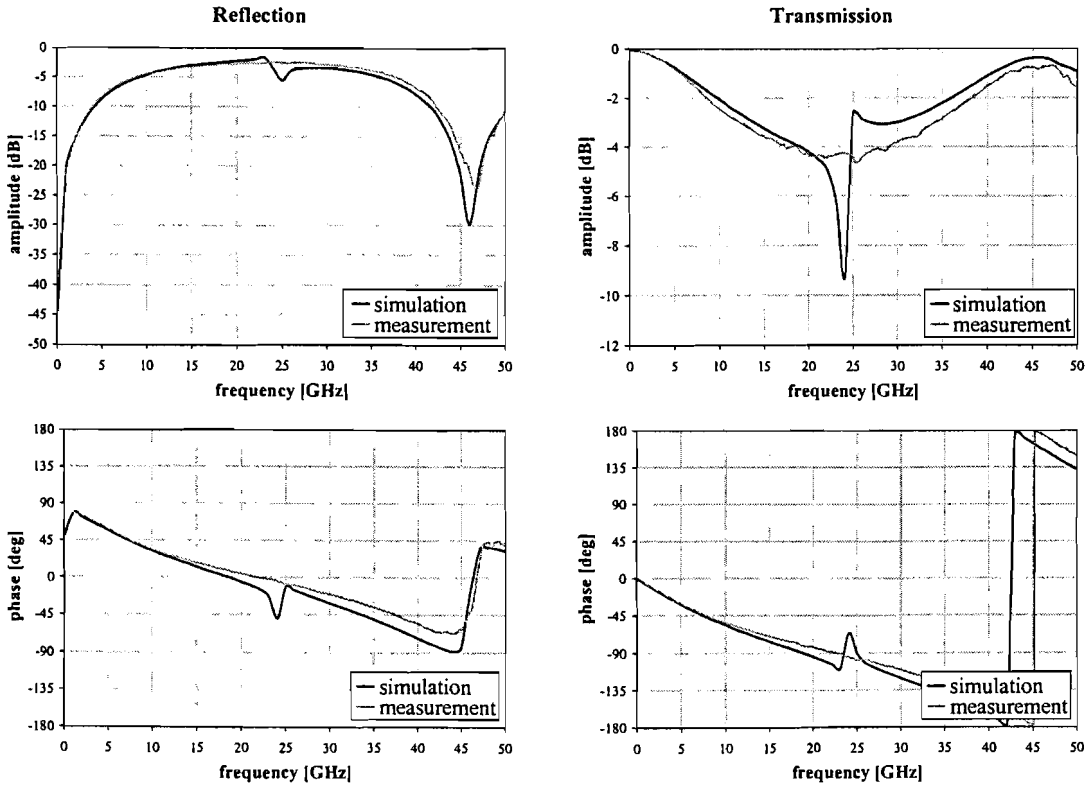Figure 6.8 Comparison of a laterally small simulated and measured coplanar waveguide.

Figure 6.9 Comparison of a laterally large simulated and measured coplanar waveguide.

6.4 HP High-frequency structure simulator

Only one full structure simulation was performed using HP HFSS. The increased flexibility available in HFSS also provides a higher complexity in the design and definition of the structure. Due to the limited amount of time that remained, no other simulations were performed using HFSS.

The pictures below show the result of the HFSS simulation for a through structure with a width of 25 μm a spacing of 10 μm, the scattering parameters of the three basic modes are presented.

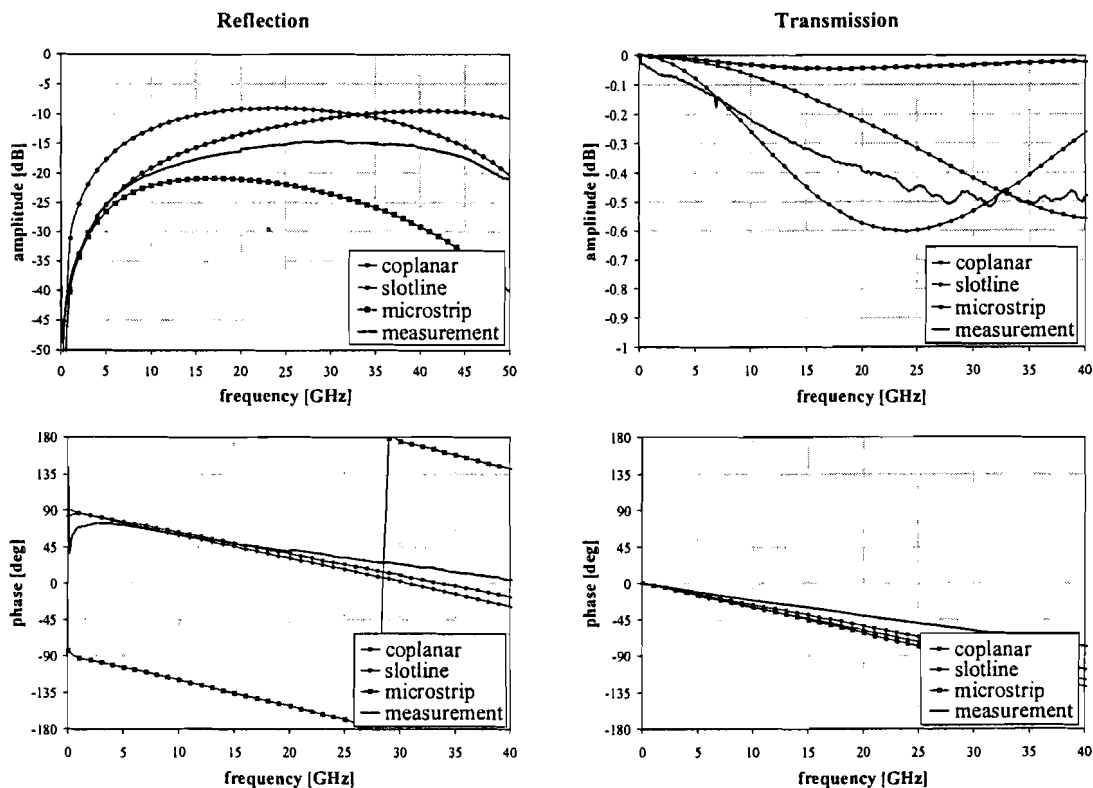**Reflection**   **Transmission**

Figure 6.10 Comparison of a measurement and a HFSS simulation showing the three basic modes.

The pictures show that the simulated coplanar reflection coefficient resembles the measured reflection, the transmission however still shows a large difference. the microstrip mode also shows behaviour similar to the measurements for the reflection but shows an even larger difference for the transmission. Finally the slotline mode shows a large difference for the reflection but is able to account for the lower transmission.

To understand how HFSS works with these different modes, one should first understand how HFSS works in general. But for this work it suffices to mention that HFSS calculates a two dimensional electromagnetic solution at the ports, called the port solution. Actually there are a number of port solutions, each one of these solutions corresponds with a certain mode. By applying a certain solution as a boundary condition this specific mode is excited and thus the solution for this mode is obtained.

To check whether HFSS simulations would result in higher order modes a simulation with a larger number of modes was run. The propagation constants of these modes are presented below, three parallel plate higher-order modes can be observed next to the common microstrip, slotline and coplanar waveguide modes:
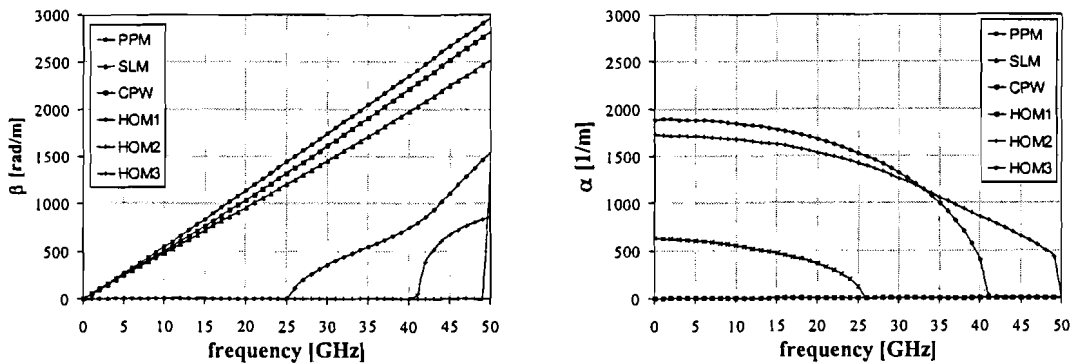

Figure 6.11 The propagation and attenuation constants of six modes on a coplanar waveguide.

The picture below presents the reflection and transmission for a large line, if the frequency at which the distortion first occurs is compared to the frequency at which the higher order modes begin to propagate a correlation can be observed.
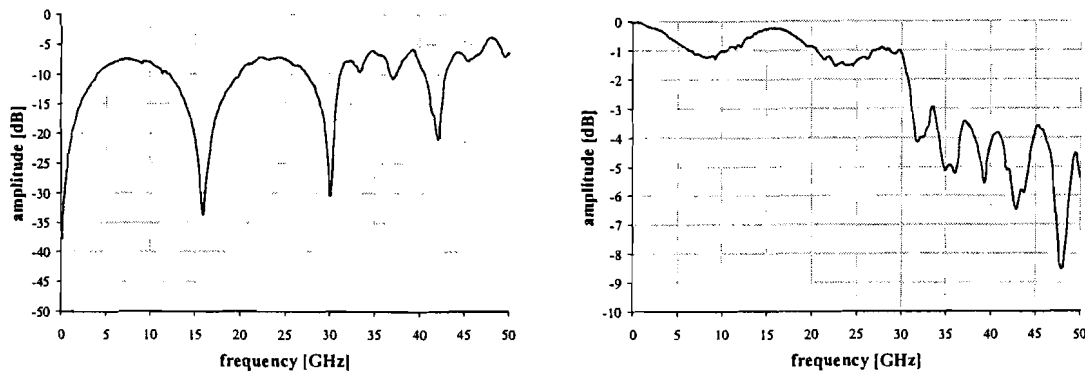

Figure 6.12 Measured reflection and transmission for a laterally large line.

It is clear to see that higher order modes due occur, but the influence of these modes on the final measurement is less clear. HFSS supports no means to mould the six sets of S-parameter data into one set, which represents the actual measurement situation. A proposition for a method to be able to verify the influence of the higher order modes is presented below:

The output is a (N*M)x(N*M)-matrix, where N is the number of ports and M is the number of modes. If the incoming wave is assumed to be a superposition of the six modes with weight factors a_1 to a_6 the scattering parameters at the output can be calculated as well. By introducing a second set of weighting factors the resulting scattering parameter matrix could be calculated. This 2x2-matrix would than contain the interaction between the different modes caused by discontinuities within the structure.

7 Conclusions and recommendations

7.1 Conclusions

This section will draw conclusions with regard to this report based on the five goals mentioned in section 1.2.

Conclusions with respect to the overview of the passive components

The goal was aimed at the passive components required for a monolithic or hybrid GaN-based HPA. An assessment should be made which matching networks would best suit the requirements.

- It has been established that a monolithic or hybrid solution has to be based on coplanar waveguide instead of the more common microstrip transmission lines, since no via holes can be realised on a sapphire substrate.
- General transmission line theory combined with some basic matching theory resulted in an approximate solution for the matching networks required for a GaN based high-power amplifier.
- The lumped element solution has been eliminated due to the lack of current carrying capability of the spiral inductors required to realise the inductance values. A solution based on lumped element resistors and MIM capacitors in combination with inductance realised by long transmission lines should be used.

It can be concluded that any research towards passive components for a GaN based amplifier should focus on coplanar waveguide elements. Key elements are lumped element resistors, lumped element capacitors, coplanar waveguide transmission lines and coplanar waveguide transmission line discontinuities.

Conclusions with respect to a measurement based approach to modelling of passive components

The requirements for a measurement based modelling approach have been explored. This lead to three basic requirements, capacitance measurements, pad structure extraction algorithms and a de-embedding algorithm.

- The first measurement that has been explored is the measurement of the transmission line capacitance per unit length. It has been established that the set-up based on a HP 4275 A LZR meter is capable of these measurements with a standard deviation of approximately 0.3 fF. The measurements have been compared to two conformal mapping algorithms and show good agreement for the relevant structures.
- The second topic that was covered focuses on the extraction of the scattering parameters of a pad structure. Three methods have been implemented, which are based on general calibration algorithms but have been adapted to simplify the required calculations. All three methods have shown to produce acceptable pad structures.
- The third topic that was covered is the routine that is required for the de-embedding of measurements. The routine that was implemented uses the results from the LRL pad extraction and subtracts the pads from any subsequent measurement. Since no passive components have been characterised the method has been tested on a short circuit and an open, the results of this de-embedding test are very promising.

It can be concluded that the basic elements required for a measurement based approach to modelling coplanar waveguides are met, the three key elements are de-embedding, pad extraction and capacitance measurements.

Conclusions with respect to a simulation based approach to modelling of passive components

The viability of extracting structure models based on simulations has been investigated using electromagnetic structure simulators, which are Sonnet EM Suite, HP Momentum and HP High-frequency structure simulator.

- Sonnet EM suite, the similarity between the measurements and the simulations is reasonable. It would be interesting to verify whether Sonnet is able to reproduce the behaviour of more complex circuits.
- HP Momentum, the agreement between the measurements and the simulations is reasonable at best.
- HP HFSS, the only true three dimensional structure simulator, only one simulation was performed, the result was promising. Higher order modes are indicated with cut-off frequencies of 25 GHz, 40 GHz and 48 GHz. This is in agreement with the frequency at which the first resonant behaviour is observed.

Due to the limited amount of time spent evaluating the electromagnetic simulators a hard conclusion can not be drawn. However, the result obtained using HFSS indicates the possibility of studying the influence of the higher-order modes. This influence should be tested to greater degree, which will require a series of experiments with different geometry variations.

Conclusions with respect to the characterisation of a set of coplanar waveguides

A scalable model for a conductor-backed coplanar waveguide based on the extracted propagation constant and characteristic impedance has been derived from measurements using previously described algorithms.

- The first scalable model was created for the measured transmission line capacitance, an overall error bound well below 1 % for the measured capacitance values was obtained. The measurements showed good agreement with two conformal mapping algorithms indicating that the measurement was correct.
- The extracted propagation constant shows no apparent trend. However a constant value of 46.2 radm^{-1} at 1 GHz results in a reasonable fit. TXLine shows the same behaviour, with an error bound below 1 % for a constant value of 46.7 radm^{-1} at 1 GHz.
- The characteristic impedance was calculated using the capacitance and the propagation constant, again a comparison with TXLine results in reasonable agreement.

It can be concluded that a scalable model for the transmission line parameters can be extracted which shows reasonable accuracy over the entire geometry range. Reasonable agreement was observed with respect to conformal mapping algorithms and TXLine.

Conclusions with respect to feasibility of a coplanar GaN-based HPA

After all the different aspects of modelling coplanar waveguide elements have been treated a conclusion can be drawn with respect of the feasibility of a coplanar GaN-based HPA.

- The effective wavelength is approximately 3 mm at 8 GHz, indicating that the inductors, which are realised by transmission lines, will require a length in the millimetre range.
- It has been shown that the lateral dimensions have to be limited, indicating the need for a thicker plating.
- Models can be extracted based on measurements, this indicates that it should be possible to extract the models required for the design of the amplifier.

It has been established that the coplanar elements required for a GaN-based HPA can be realised, although these elements will probably require thicker plating to limit lateral dimensions of the transmission lines. A method for the extraction of the models required for a GaN-based HPA was proposed and successfully tested. These facts lead to the final conclusion that a coplanar GaN-based HPA is feasible, although a lot of effort will be required to model the necessary elements and expand the knowledge with respect to thick plating.

For this reason the next section will be used to introduce some reflections and some topics which have not been worked-out in this work. Any future work could include these topics.

7.2 Recommendations and future work

The examples of coplanar structures presented below have been implemented in a mask generation program, which will not be discussed in further detail.

Changes in coplanar waveguide structures

The structures that were designed for the first mask were intended to be fabricated at the Eindhoven University of technology. Due to problems with the fabrication of masks the mask was kept as simple as possible. If the mask is fabricated elsewhere the complexity of the mask could be increased. This increased complexity could be used to create pad structures with smoother transitions.
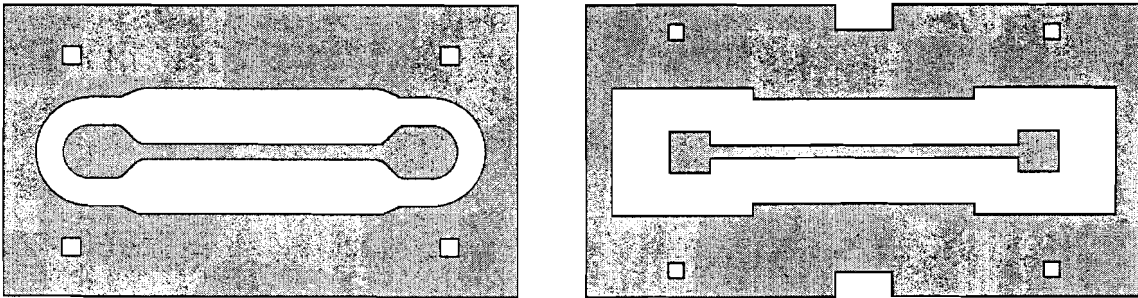
Figure 7.1 Lay-out of the optimised, left, and original, right, through structure.

The improvements that are introduced to this new through structure are presented below:

- Pad structure impedance was matched to a 50 Ω transmission line geometry, which improves the match between probe and pad structure.
- The pad structure has a round end capacitance, the removal of the edges introduces a better defined state, and no unnecessary discontinuities are introduced.
- The transitions in line width and spacing are smoothened using a cosine function. This way the transition is less abrupt and a lower reflection can be expected.

The same optimisation can be applied to an open end structure, which is presented below.
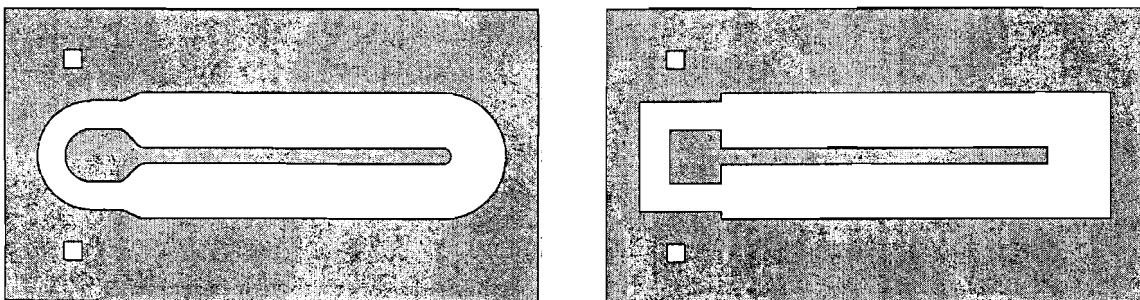

Figure 7.2 Lay-out of the optimised, left, and original, right, open structure.

It is common practice to describe an open and short by an additional length of transmission line. In case the new geometry is used the open circuit will behave as a true additional length of transmission line, due to the fact that the end of the transmission line will not cause distortions in the field pattern.

Influence of characteristic impedance on the pad structure extracted using the BCL algorithm

One item, which has not been mentioned before, is an effect that was noticed when the pad structures were extracted. As mentioned in chapter five the pad structures were extracted using the BCL algorithm since this algorithm is able to account for the different characteristic impedance levels at both ports of the pad structure. It was noted that the extracted scattering parameters of the pad structures show a minimum near the characteristic impedance obtained for the transmission lines, this effect is presented below:
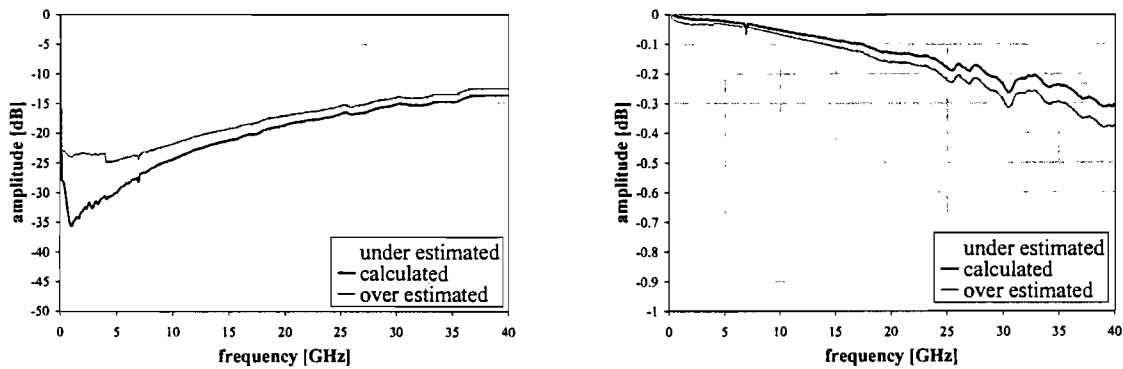
Figure 7.3 Influence of the characteristic impedance on the extracted pad structure.

The relation between the characteristic impedance and the extracted pad structure, which is observed, could be used to verify the extracted characteristic impedance. Perhaps the necessity of a separate capacitance measurement could be eliminated completely.

Further investigations using HFSS

Additional attention should be paid to the output produced by HFSS. As the scattering parameters for each of the modes are generated it should be possible to use this data to predict the measured behaviour. As mentioned before HFSS generates a $(N*M)x(N*M)$-matrix, where N is the number of ports and M is the number of modes. A program could be written, for example using MATLAB, which combines the scattering parameter data and transforms them into a measurement like data set.
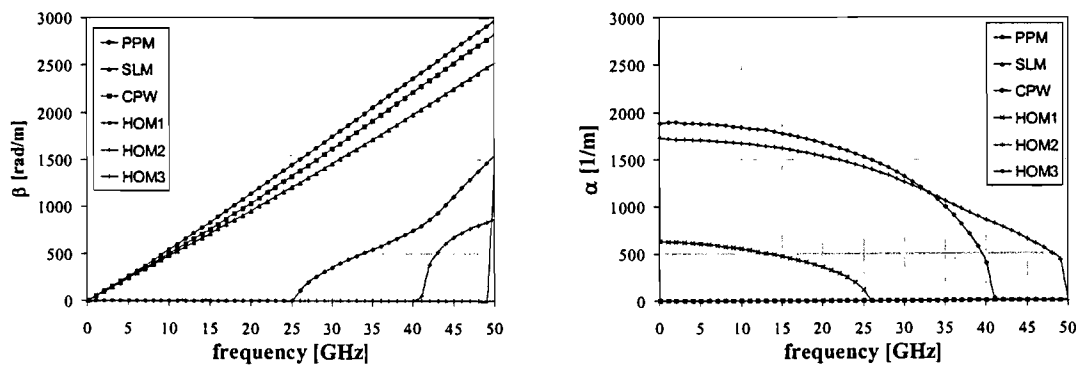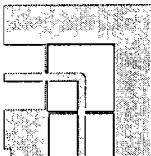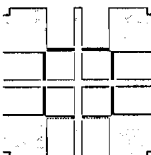

Figure 7.4 The real and imaginary part of the propagation constants of the six modes on a coplanar waveguide.

The propagation constant of the higher order modes are presented above, they indicate that these modes can propagate through the structure. The only thing missing at this moment is a method to describe their interaction. This will require investigation into the weighing vector, which should be used to divide the input wave over the different modes and the weighing vector used to describe the resulting output.

Modelling of coplanar waveguide discontinuities

Finally some attention has to be paid to which structures should be modelled. It is apparent that a set of coplanar waveguide discontinuities should be modelled. Among these structures at least those presented below should be incorporated.

Table 7.1 Overview of the required coplanar waveguide discontinuities.

element	example
OPEN An open end can be used in stubs, closing the end by connecting the two ground planes ensures a defined situation, increasing the model accuracy.	
SHORT An short circuit can be used in stubs. The short circuit is inherently better defined than the open end and could for that reason be preferred.	
BRIDGE Bridges should be used in any coplanar waveguide design to periodically tag both ground planes together. Two topologies are possible for the airbridge, either lifting the ground plane or the signal track.	
CORNER To be able to increase the length of the transmission line segments without wasting chip area the transmission line are folded together. The ground planes can be connected using several methods. Furthermore a curved corner could be used.	
TEE Tees can be used to split signal paths. Normally the tee will connect two signal paths with a wider signal path. Again several methods are available to connect the three ground planes. Finally, a choice might be made to choose a Y-shape instead of the T-shape depicted here.	
CROSS In case a division into three signal leads is required, the cross structure could be used, again supporting different methods to connect the four ground planes.	
TAPER A taper can be used to connect different lines together. The taper introduces less of a discontinuity than the step in width.	

Up to this point the focus was placed on modelling single structures, such as a corner or capacitor. It should be verified if the models generated for these are able to predict the behaviour of more complex structures. For this reason special attention should be paid to types of circuits which could be used to verify the models of single components. One could use simple band-pass filters or simple single stub matching networks.

Reference list

General

[1] M. Gillick et al, 'Uniplanar techniques for monolithic microwave integrated circuits', Electronics and communication engineering journal, August 1994 pp. 187-193.
[2] W. Heinrich and C. Rheinfeld, 'Coplanar silicon MMICs', IEEE 1998, pp 79-84.
[3] Y. Baeyens et al, 'Design of compact millimeter-wave MMICs using CPW', IEE. 1997.
[4] R. Sorrentino, 'Modeling of microwave and millimeter wave passive components in Europe' IEEE microwave theory and techniques digest 1989, pp. 613-616.
[5] T. Sporkmann, 'The current state of the art in coplanar MMICs', Microwave journal 1998, pp. 60-74.
[6] F. Gonzalez, 'Effects of matching on RF power amplifier efficiency and output power', microwave journal, April 1998, pp. 60-72.

conformal mapping and related topics

[7] W. Heinrich, ' Quasi-TEM description of MMIC coplanar lines including conductor-loss effects', IEEE transactions on microwave theory and techniques, vol. 41, no. 1, pp. 45-52.
[8] W. Heinrich, 'Full-wave analysis of conductor losses on MMIC transmission lines', IEEE microwave theory and techniques digest 1989, pp. 911-914.
[9] W. Heinrich, 'Full-wave analysis of conductor losses on MMIC transmission lines', IEEE microwave theory and techniques, vol. 38, no. 10, pp. 1468-1472.
[10] J.W. Lee et al, 'Quasi-static analysis of conductor-backed coupled coplanar waveguide', Electronics letters, vol. 34, no. 19, pp. 1861-1862.
[11] M. Gillick et al, 'An analytical method for direct calculation of E & H-field patterns of CBCPW' IEEE transactions on microwave theory and techniques, vol. 41, no. 9, pp. 1606-1610.
[12] M. Gillick et al, 'Direct solution for the E-field distribution at the conductor surfaces of CPW' IEEE transactions on microwave theory and techniques, vol. 41, no. 1, pp. 129-135.
[13] D.F. Williams et al, 'Quasi-TEM model for coplanar waveguide on Silicon', 1997, pp. 225-228.
[14] G. Ponchak et al, 'A measurement based design equation for the attenuation of MMIC CPWs', IEEE transactions on microwave theory and techniques 1999, vol. 47, no. 2, pp. 241-243.

Coplanar waveguide modes and propagation

[15] M. Riaziat et al, 'Propagation modes and dispersion characteristics of coplanar waveguides', IEEE transactions on microwave theory and techniques, vol. 38, no. 3, pp. 245-251.
[16] J. Sheen and Y. Lin, 'Propagation characteristics of the slotline first higher order mode', IEEE transactions on microwave theory and techniques, vol. 46, no. 11, pp.1774-1781.
[17] A.K. Rastogi and S. mishra, 'Coplanar waveguide characterisation with thick metal coating', Journal of infrared and millimeter Waves, vol. 20, no. 3, 1999, pp. 505-525.
[18] W.T. Lo et al, 'Resonant phenomena in conductor backed coplanar waveguides', IEEE microwave theory and techniques digest 1993, pp. 1199-1202

Network analyser calibration

[19] J. Pla et al, 'On-wafer calibration techniques for measurement of microwave circuit and devices on thin substrates', IEEE microwave theory and techniques digest 1995, pp. 1045-1048.

[20] K.J. Silvonen, 'A general approach to network analyzer calibration' IEEE transactions on microwave theory and techniques, vol. 41, no. 4, pp. 754-759.

[21] R.R. Pantoja et al, 'Improved calibration and measurement of the S-parameters of microwave ICs', IEEE transactions on microwave theory and techniques, vol. 37, no. 11, pp. 1675-1680.

[22] R.A. Soares et al, 'A Unified mathematical approach to two-port calibration techniques', IEEE transactions on microwave theory and techniques, vol. 37, no. 11, pp. 1669-1673.

[23] C. Wan et al, 'A simple error correction method for 2-port transmission parameter measurement', IEEE microwave and guided wave letters, vol. 8, no. 2, pp. 58-59.

[24] R.B. Marks, 'A multiline method of network analyzer calibration', IEEE transactions on microwave theory and techniques, vol. 39, no. 7, pp. 1205-1215.

[25] M.I. Herman et al, 'Millimeter wave deembedding using the extended TRL(ETRL) approach', IEEE microwave theory and techniques digest 1990, pp. 1033-1036.

[26] C.F. Engen and C.A. Hoer, 'TRL : an improved technique for calibration the dual 6-port ANA', IEEE transactions on microwave theory and techniques, vol. 27, no. 12, pp. 987-993.

[27] H.J. Eul and B. Schiek, 'A generalized theory and new calibration procedure for NA calibration', IEEE transactions on microwave theory and techniques, vol. 39, no. 4, pp. 724-731.

[28] F.Th. Nagelhout, 'Een calibratie procedure voor netwerk analyzer S-parameter metingen gebruik makend van het TSD-algoritme', 1981.

Characteristic impedance extraction

[29] D.F. Williams and R.B. Marks, 'On-wafer impedance measurement on lossy substrates', IEEE microwave and guided wave letters 1994, vol. 4, no. 6, pp. 175-176.

[30] D.F. Williams and R.B. Marks, 'The interpretation and use of S-parameters in lossy lines', Publication of the national institute of standards and technology, pp. 84-90.

[31] D.F. Williams and R.B. Marks, 'Transmission line capacitance measurement', IEEE microwave and guided wave letters 1991, vol. 1, no. 9, pp. 243-245.

[32] D.F. Williams and R.B. Marks, 'Characteristic impedance determination using propagation constant measurement', IEEE microwave and guided wave letter, vol. 1, no. 6, pp. 141-143.

[33] G. Carchon et al, 'Compensating differences between measurement and calibration wafer probe tip calibrations – deembedding of line parameters', 28th European microwave conference, pp. 259-264.

[34] D.F. Williams, 'Accurate Characteristic impedance measurement on silicon', IEEE microwave theory and techniques digest 1998, pp. 1917-1920.

[35] M. Janezic and D.F. Williams, 'Permittivity characterization from transmission line measurement', IEEE microwave theory and techniques digest 1997, pp. 1343-1346.

[36] J. Mondal and T. Chen, 'Propagation constant determination in microwave fixture deembedding procedure', IEEE transactions on microwave theory and techniques, col. 36, no. 4, pp. 706-714.

Transmission line theory

[37] E.H. Fooks and R.A. Zakarevicius, 'Microwave engineering using microstrip circuits', 1990 Prentice Hall, ISBN 0136916503.

[38] L.N. Dworsky, 'Modern transmission line theory and applications', 1979 John Wiley & sons, inc. ISBN 0-471-04086-X.

[39] S.Y. Liao, 'Microwave devices & circuits – third edition', 1980 Prentice-Hall, ISBN 0-13-583204-7.

[40] R. Goyal, 'Monolithic microwave integrated circuits: technology & design', 1989 Artech house, inc. ISBN 0-89006-309-5.

[41] D.M. Pozar, 'Microwave engineering', 1990 Addison-Wesly Publishing company, inc. ISBN 0-201-50418-9.

A S-parameters and Smith charts

A.1 S-Parameters

Normally circuit theory uses impedance or admittance parameters to describe two-port behaviour. The impedance parameters for a two-port network can be defined by a matrix relation presented below:

$$\begin{bmatrix} V_1 \\ V_2 \end{bmatrix} = \begin{bmatrix} Z_{11} & Z_{12} \\ Z_{21} & Z_{22} \end{bmatrix} \cdot \begin{bmatrix} I_1 \\ I_2 \end{bmatrix} \qquad \text{thus } Z_{11} = \frac{V_1}{I_1}\bigg|_{I_2=0} \qquad [A.1]$$

with V_1 and V_2 the voltages across and I_1 and I_2 the currents into ports 1 and 2 respectively. This means the a hypothetical open circuit is needed in order to define the two-port, likewise admittance parameters require a short circuit. At microwave frequencies shorts and opens no longer exist since the parasitics of these structures play a dominant role, and are likely to cause instabilities in the measurements.

Scattering parameters have the same goal as the impedance or admittance parameters, the only difference is that the two-port is described as a function of incident, reflected and transmitted power waves, the figure below presents a two port with the appropriate definitions:
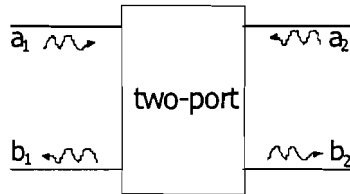

Figure A.1 Incident and reflected waves at the input and output of a two-port network.

this results in the parameter matrix presented below:

$$\begin{bmatrix} b_1 \\ b_2 \end{bmatrix} = \begin{bmatrix} S_{11} & S_{12} \\ S_{21} & S_{22} \end{bmatrix} \cdot \begin{bmatrix} a_1 \\ a_2 \end{bmatrix} \qquad \text{thus } S_{11} = \frac{b_1}{a_1}\bigg|_{a_2=0}$$
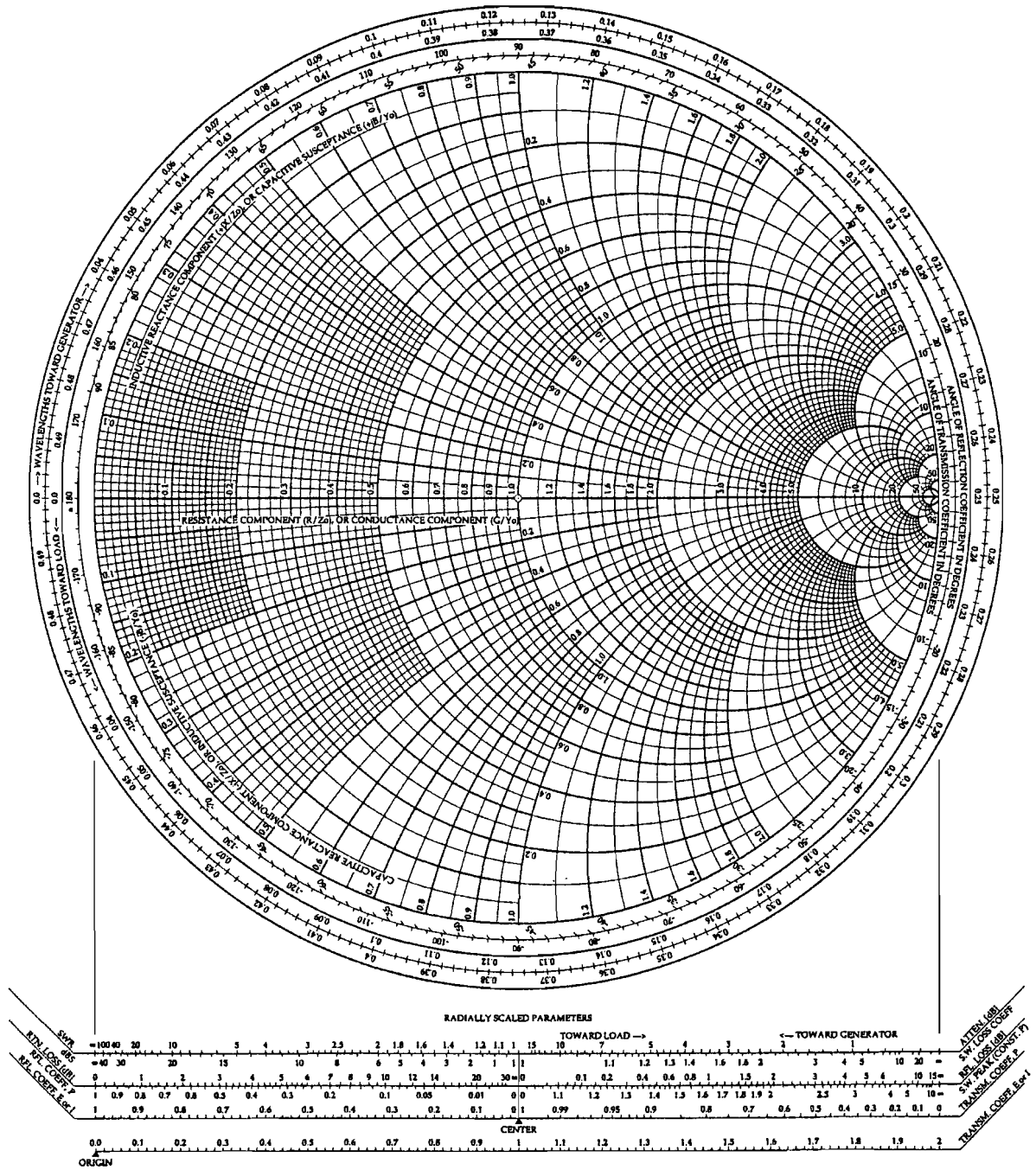
with

$$a_i = \frac{V_i + Z_i I_i}{2\sqrt{R_i}} = \frac{V_0^+}{R_0} \qquad [A.2]$$

$$b_i = \frac{V_i - Z_i^* I_i}{2\sqrt{R_i}} = \frac{V_0^-}{R_0} \qquad [A.3]$$

For the scattering parameters, the incident wave at port 2 needs to be set to zero, this can be achieved by connecting port 2 to a perfectly matched load.

A.2 Smith charts

The Complete Smith Chart
Black Magic Design

A.3 Parameter conversions

	S	Z	Y	H	ABCD
S	$S_{11}\ S_{12}$ $S_{21}\ S_{22}$	$S_{11}=\dfrac{(z_{11}-1)(z_{22}+1)-z_{12}z_{21}}{\Delta_{zs}}$ $S_{12}=\dfrac{2z_{12}}{\Delta_{zs}}$ $S_{21}=\dfrac{2z_{21}}{\Delta_{zs}}$ $S_{22}=\dfrac{(z_{11}+1)(z_{22}-1)-z_{12}z_{21}}{\Delta_{zs}}$	$S_{11}=\dfrac{(1-y_{11})(1+y_{22})+y_{12}y_{21}}{\Delta_{ys}}$ $S_{12}=\dfrac{-2y_{12}}{\Delta_{ys}}$ $S_{21}=\dfrac{-2y_{21}}{\Delta_{ys}}$ $S_{22}=\dfrac{(1+y_{11})(1-y_{22})+y_{12}y_{21}}{\Delta_{ys}}$	$S_{11}=\dfrac{(h_{11}-1)(h_{22}+1)-h_{12}h_{21}}{\Delta_{hs}}$ $S_{12}=\dfrac{2h_{12}}{\Delta_{hs}}$ $S_{21}=\dfrac{-2h_{21}}{\Delta_{hs}}$ $S_{22}=\dfrac{(1+h_{11})(1-h_{22})+h_{12}h_{21}}{\Delta_{hs}}$	$S_{11}=\dfrac{a+b-c-d}{a+b+c+d}$ $S_{12}=\dfrac{2(ad-bc)}{a+b+c+d}$ $S_{21}=\dfrac{2}{a+b+c+d}$ $S_{22}=\dfrac{b-a-c+d}{a+b+c+d}$
Z	$z_{11}=\dfrac{(1+S_{11})(1-S_{22})+S_{12}S_{21}}{\Delta_{sz}}$ $z_{12}=\dfrac{2S_{12}}{\Delta_{sz}}$ $z_{21}=\dfrac{2S_{21}}{\Delta_{sz}}$ $z_{22}=\dfrac{(1-S_{11})(1+S_{22})+S_{12}S_{21}}{\Delta_{sz}}$	$z_{11}\ z_{12}$ $z_{21}\ z_{22}$	$\dfrac{y_{22}}{\lvert y\rvert}\quad -\dfrac{y_{12}}{\lvert y\rvert}$ $-\dfrac{y_{21}}{\lvert y\rvert}\quad \dfrac{y_{11}}{\lvert y\rvert}$	$\dfrac{\lvert h\rvert}{h_{22}}\quad \dfrac{h_{12}}{h_{22}}$ $-\dfrac{h_{21}}{h_{22}}\quad \dfrac{1}{h_{22}}$	$\dfrac{a}{c}\quad \dfrac{ad-bc}{c}$ $\dfrac{1}{c}\quad \dfrac{d}{c}$
Y	$y_{11}=\dfrac{(1-S_{11})(1+S_{22})+S_{12}S_{21}}{\Delta_{sy}}$ $y_{12}=\dfrac{-2S_{12}}{\Delta_{sy}}$ $y_{21}=\dfrac{-2S_{21}}{\Delta_{sy}}$ $y_{22}=\dfrac{(1+S_{11})(1-S_{22})+S_{12}S_{21}}{\Delta_{sy}}$	$\dfrac{z_{22}}{\lvert z\rvert}\quad -\dfrac{z_{12}}{\lvert z\rvert}$ $-\dfrac{z_{21}}{\lvert z\rvert}\quad \dfrac{z_{11}}{\lvert z\rvert}$	$y_{11}\ y_{12}$ $y_{21}\ y_{22}$	$\dfrac{1}{h_{11}}\quad -\dfrac{h_{12}}{h_{11}}$ $\dfrac{h_{21}}{h_{11}}\quad \dfrac{\lvert h\rvert}{h_{11}}$	$\dfrac{d}{b}\quad \dfrac{bc-ad}{b}$ $-\dfrac{1}{b}\quad \dfrac{a}{b}$
H	$h_{11}=\dfrac{(1+S_{11})(1+S_{22})-S_{12}S_{21}}{\Delta_{sh}}$ $h_{12}=\dfrac{2S_{12}}{\Delta_{sh}}$ $h_{21}=\dfrac{-2S_{21}}{\Delta_{sh}}$ $h_{22}=\dfrac{(1-S_{11})(1-S_{22})-S_{12}S_{21}}{\Delta_{sh}}$	$\dfrac{\lvert z\rvert}{z_{22}}\quad \dfrac{z_{12}}{z_{22}}$ $-\dfrac{z_{21}}{z_{22}}\quad \dfrac{1}{z_{22}}$	$\dfrac{1}{y_{11}}\quad -\dfrac{y_{12}}{y_{11}}$ $\dfrac{y_{21}}{y_{11}}\quad \dfrac{\lvert y\rvert}{y_{11}}$	$h_{11}\ h_{12}$ $h_{21}\ h_{22}$	$\dfrac{b}{d}\quad \dfrac{ad-bc}{d}$ $-\dfrac{1}{d}\quad \dfrac{c}{d}$
ABCD	$a=\dfrac{(1+S_{11})(1-S_{22})+S_{12}S_{21}}{2S_{21}}$ $b=\dfrac{(1+S_{11})(1+S_{22})-S_{12}S_{21}}{2S_{21}}$ $c=\dfrac{(1-S_{11})(1-S_{22})-S_{12}S_{21}}{2S_{21}}$ $d=\dfrac{(1-S_{11})(1+S_{22})+S_{12}S_{21}}{2S_{21}}$	$\dfrac{z_{11}}{z_{21}}\quad \dfrac{\lvert z\rvert}{z_{21}}$ $\dfrac{1}{z_{21}}\quad \dfrac{z_{22}}{z_{21}}$	$-\dfrac{y_{22}}{y_{21}}\quad -\dfrac{1}{y_{21}}$ $-\dfrac{\lvert y\rvert}{y_{21}}\quad -\dfrac{y_{11}}{y_{21}}$	$-\dfrac{\lvert h\rvert}{h_{21}}\quad -\dfrac{h_{11}}{h_{21}}$ $-\dfrac{h_{22}}{h_{21}}\quad -\dfrac{1}{h_{21}}$	$a\ b$ $c\ d$

$$\Delta_{zs} = (z_{11}+1)(z_{22}+1)-z_{12}z_{21}$$
$$\Delta_{ys} = (y_{11}+1)(y_{22}+1)-y_{12}y_{21}$$
$$\Delta_{hs} = (h_{11}+1)(h_{22}+1)-h_{12}h_{21}$$

$$\Delta_{sz} = (1-s_{11})(1-s_{22})-s_{12}s_{21}$$
$$\Delta_{sy} = (1+s_{11})(1+s_{22})-s_{12}s_{21}$$
$$\Delta_{sh} = (1-s_{11})(1+s_{22})+s_{12}s_{21}$$

$$Z_{11}=z_{11}Z_0 \qquad Z_{12}=z_{12}Z_0 \qquad Z_{21}=z_{21}Z_0 \qquad Z_{22}=z_{22}Z_0$$
$$Y_{11}=y_{11}Y_0 \qquad Y_{12}=y_{12}Y_0 \qquad Y_{21}=y_{21}Y_0 \qquad Y_{22}=y_{22}Y_0$$
$$H_{11}=h_{11}Z_0 \qquad H_{12}=h_{12} \qquad H_{21}=h_{21} \qquad H_{22}=h_{22}Y_0$$
$$A=a \qquad\qquad B=bZ_0 \qquad\qquad C=cY_0 \qquad\qquad D=d$$

$$\lvert z\rvert = z_{11}z_{22}-z_{12}z_{21}$$
$$\lvert y\rvert = y_{11}y_{22}-y_{12}y_{21}$$
$$\lvert h\rvert = h_{11}h_{22}-h_{12}h_{21}$$
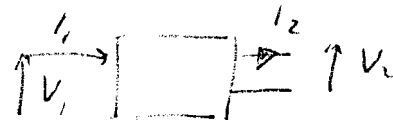
B Pad extraction algorithms

B.1 LRL extraction routine

B.1.1 LRL algorithm

The LRL calibration uses two transmission lines of different length and one short circuit, the behaviour of which does not need to be known. The only limitation placed on the short is that its behaviour is symmetrical with respect to the two ports, which can be guaranteed by designing a symmetrical short.

The LRL algorithm uses wave cascading parameters for the calculations, the relation between wave cascading parameters and scattering parameters are presented below:

$$[T] = \frac{1}{S_{21}} \begin{bmatrix} S_{12}S_{21} - S_{11}S_{22} & S_{11} \\ -S_{22} & 1 \end{bmatrix} \qquad \begin{matrix} b_l & a_2 \\ a_1 & = T \ b_2 \end{matrix} \qquad [B.1]$$

The wave cascading matrix of a lossy transmission line can be written as:

$$[T_{line}] = \begin{bmatrix} e^{-\gamma l} & 0 \\ 0 & e^{\gamma l} \end{bmatrix} \qquad [B.2]$$
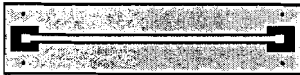
The T-Parameters of the pad structures are presented below:

$$[T_{pad}] = \begin{bmatrix} P_{11} & P_{12} \\ P_{21} & P_{22} \end{bmatrix} \qquad [B.3]$$

The LRL algorithm extracts two pad structures, P_a is the pad structure at port one while P_b represents the pad structure at the second port of the network analyser.

The standards used with the LRL calibration procedure are presented below.

structure	scheme	measurement	theoretical matrix	
through		$\begin{bmatrix} S_{T11} & S_{T12} \\ S_{T21} & S_{T22} \end{bmatrix}$	$[M_{through}] = [T_{pad}][T_{pad}]^{*}$	[B.4]
line A		$\begin{bmatrix} S_{D11} & S_{D12} \\ S_{D21} & S_{D22} \end{bmatrix}$	$[M_{line}] = [T_{pad}][T_{lineA}][T_{pad}]^{*}$	[B.5]
reflect		$\begin{bmatrix} S_{RA} & 0 \\ 0 & S_{RB} \end{bmatrix}$		[B.6]

The first step is to combine [B.4] and [B.5] which yields the expressions below:

$$[M_{delay}] = [T_{pad}][T_{line}][T_{pad}]^{-1} \cdot [M_{through}]$$ [B.7]

$$[M_{dtA}][T_{pad}] = [T_{pad}][T_{line}]$$ [B.8]

with

$$[M_{dtA}] = [M_{delay}][M_{through}]^{-1} = \begin{bmatrix} M_{11A} & M_{12A} \\ M_{21A} & M_{22A} \end{bmatrix}$$ [B.9]

The next step is to write [B.9] in to its separate term so the final relations can be exposed.

$$M_{11A}P_{11A} + M_{12A}P_{21A} = P_{11A}e^{-\gamma l}$$ [B.10]

$$M_{21A}P_{11A} + M_{22A}P_{21A} = P_{21A}e^{-\gamma l}$$ [B.11]

$$M_{11A}P_{12A} + M_{12A}P_{22A} = P_{12A}e^{\gamma l}$$ [B.12]

$$M_{21a}P_{12A} + M_{22A}P_{22A} = P_{22A}e^{\gamma l}$$ [B.13]

Where l is equal to the difference in line length between the through and the delay. Dividing [B.10] by [B.11] and [B.12] by [B.13] yields two quadratic equations which have the same coefficients:

$$M_{21A}x^2 + (M_{22A} - M_{11A})x - M_{12A} = 0$$ [B.14]

The solutions from [B.14] should be mapped onto $\dfrac{P_{11A}}{P_{21A}}$ and $\dfrac{P_{12A}}{P_{22A}}$ which can be represented by:

$$\frac{P_{11A}}{P_{21A}} = S_{11A} - \frac{S_{21A}S_{12A}}{S_{22A}}$$ [B.15]

$$\frac{P_{12A}}{P_{22A}} = S_{11A}$$ [B.16]

smaller

This means a decision has to be made which result gets assigned to S_{11A}, this can be done using the fact that $|S_{11A} S_{22A}|$ will be larger than $|S_{11A} S_{22A} - S_{21A}S_{12A}|$ for practical situations. Finally [B.13] divided by [B.10] results in an expression for γ.

$$e^{+2\gamma l} = \frac{M_{21A}\dfrac{P_{12A}}{P_{22A}} + M_{22A}}{M_{12A}\dfrac{P_{21A}}{P_{11A}} + M_{11A}}$$ [B.17]

Using [B.18] up to [B.20] instead of [B.7] up to [B.9] results in an equivalent problem for P_b, the method is exactly the same, and no further attention will be paid to this problem.

$$[M_{delay}] = [M_{through}][T_{pad}]^{-1} \cdot [T_{line}][T_{pad}]$$ [B.18]

$$[T_{pad}][M_{dtB}] = [T_{line}][T_{pad}]$$ [B.19]

With

$$[M_{dtB}] = [M_{through}]^{-1} \cdot [M_{delay}] = \begin{bmatrix} M_{11B} & M_{12B} \\ M_{21B} & M_{22B} \end{bmatrix}$$ [B.20]

The next step is to use the two unknown but equal reflection measurements. These measurements can be made equal by measuring the same structure, or creating a symmetrical reflect structure.

$$S_{RA} = S_{11A} + \frac{S_{12A}S_{21A}}{\dfrac{1}{\Gamma_R} - S_{22A}}$$ [B.21]

$$S_{RB} = S_{22B} + \frac{S_{12B}S_{21B}}{\dfrac{1}{\Gamma_R} - S_{11B}}$$ [B.22]

Rewriting [B.21] and [B.22] yields:

$$S_{22A}\left(1 + \frac{S_{12A}S_{21A}}{S_{22A}} \frac{1}{S_{RA} - S_{11A}}\right) = S_{11B}\left(1 + \frac{S_{12B}S_{21B}}{S_{11B}} \frac{1}{S_{RB} - S_{11B}}\right)$$ [B.23]

All the elements between brackets are known from [B.15], [B.16] or measurements, S_{RA}. The next step is to use the through measurement to get a relation between S_{22A} and S_{11B}. For this purpose the wave cascading parameters of the through are expanded into S-parameter terms.

$$S_{T11} = S_{11A} + \frac{S_{12A}S_{21A}S_{11B}}{1 - S_{22A}S_{11B}}$$ [B.24]

This equation can be rewritten to form an expression of S_{11B} as function of S_{22A}.

$$S_{11B} = \left(1 + \frac{S_{12A}S_{21A}}{S_{22A}} \frac{1}{S_{T11} - S_{11A}}\right)^{-1} \frac{1}{S_{22A}}$$ [B.25]

Again measurements or [B.15] and [B.16], yield the elements situated between the brackets. Combining [B.23] with [B.25] results in the expression shown below, which yields S_{22A} and S_{11B}.

$$S_{22A} = \pm\sqrt{\left(1 + \frac{S_{12A}S_{21A}}{S_{22A}(S_{RA} - S_{11A})}\right)^{-1}\left(1 + \frac{S_{12B}S_{21B}}{S_{11B}(S_{RB} - S_{11B})}\right)\left(1 + \frac{S_{12A}S_{21A}}{S_{22A}(S_{T11} - S_{11A})}\right)^{-1}}$$ [B.26]

The choice of sign is than dictated by knowledge from the structure, using the fact that an improper choice results in a physically improbable result.

B.1.2 Symmetrical LRL algorithm

The LRL algorithm described in the previous section obtains results for S_{11A}, S_{22A}, S_{12A}, S_{21A}, S_{11B}, S_{22B} and $S_{12B}S_{21B}$. The disadvantage of this method is that the calculations required to support separate pad structures for both ports are extensive while this feature will not be used. If the algorithm is adapted in such a way that P_a equals P_b and a reciprocal circuit is assumed, i.e. $S_{12A}=S_{21A}$, the routine complexity is reduced significantly. And the reflective standard measurement is no longer needed which should also increase the extraction algorithm's accuracy.

The first step is to extract S_{11}, which is done using [B.16] from the LRL algorithm, instead of introducing the reflective measurement to extract S_{22} the through matrix is expanded and solved.

$$[T] = [T_{pad}][\underline{T_{pad}}] = \begin{bmatrix} T_{11} & T_{12} \\ T_{21} & T_{22} \end{bmatrix}$$

[B.27]

Yielding

$$T_{11} = \frac{1}{S_{21}^2}\left(S_{22}^2 S_{11}^2 - 2S_{12}^2 S_{11}S_{22} + S_{12}^4 - S_{11}^2\right)$$

[B.28]

$$T_{12} = \frac{-1}{S_{21}^2}\left(S_{22}\left(S_{11}S_{22} - S_{12}^2\right) - S_{11}\right)$$

[B.29]

$$T_{21} = \frac{1}{S_{21}^2}\left(S_{22}\left(S_{11}S_{22} - S_{12}^2\right) - S_{11}\right)$$

[B.30]

$$T_{22} = \frac{1}{S_{21}^2}\left(1 - S_{22}^2\right)$$

[B.31]

Combining [B.30] with [B.31] results in an expression for S_{22} as a function of S_{11}, as presented below:

$$S_{22} = -T_{21} - T_{22}S_{11}$$

[B.32]

The final step is to extract S_{12}, which is equal to S_{21} due to the reciprocity, by rewriting [B.15].

$$S_{12} = \pm\sqrt{-S_{22}\left(\frac{P_{11}}{P_{21}} - S_{11}\right)}$$

[B.33]

The sign choice is now fixed due to the fact that the low frequency phase should approach zero from the negative side.

B.1.3 Optimisation of the computational efficiency

The first step was to implement the routine into MATLAB using all matrix mathematics available in MATLAB. The output of this basic algorithm is presented below:
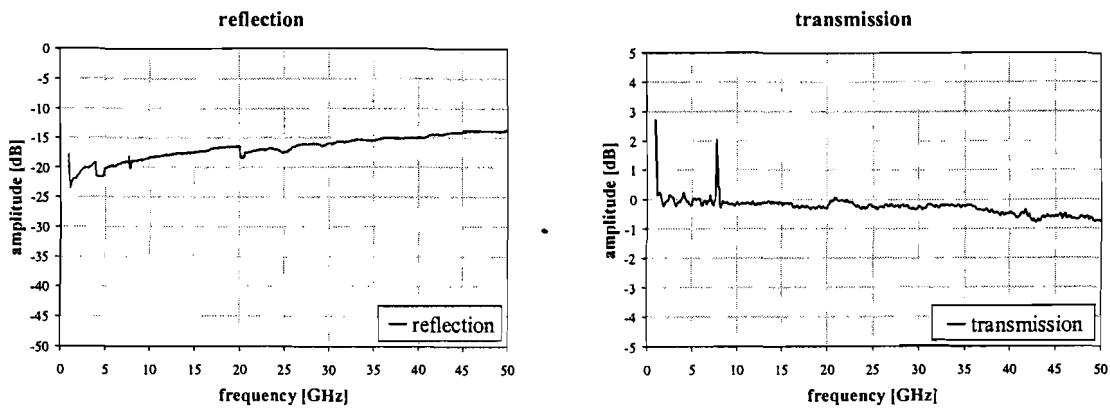

Figure B.1 Pad structure extracted using the original LRL algorithm.

As can be seen on the left picture both reflection parameters behave fairly well, which can be expected since only a limited number of calculations is needed to extract these parameters. The picture on the right shows the transmission parameter S_{12} of the pad structure, It can easily be seen that the extracted behaviour is not physically correct since this behaviour would indicate amplification, $S_{12} > 0$ dB. The graphs below present the numerical stability of the original (LRLo) algorithm.
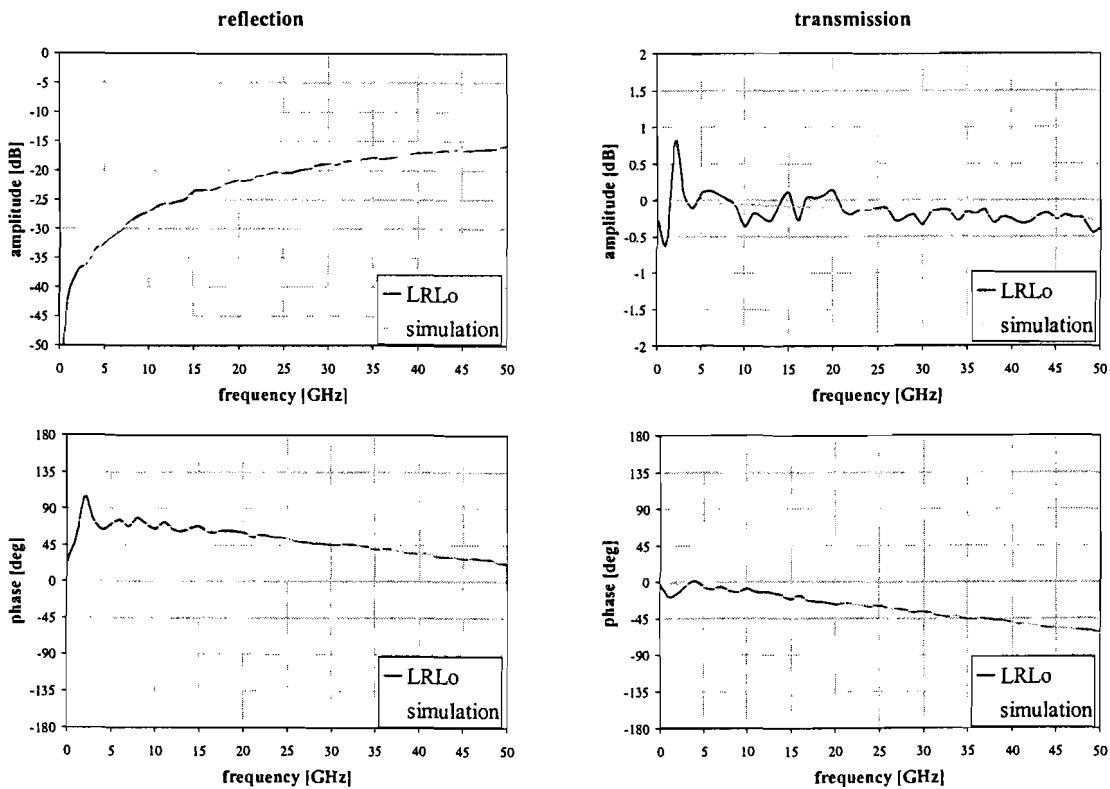
Figure B.2 Error propagation through the original LRL algorithm.

The pictures shows how a distortion of 5 percent on the input signal result in a much larger distortion on the output signal, indicating that this algorithm would probably not result in reliable output data.

The previous pictures illustrate the fact that the numerical efficiency of the original LRL algorithm is not optimised. For this reason the algorithm will be optimised using the method described below.

First we use the knowledge of the test structure, the method described here assumes that the pad structure on the left is identical to the pad structure on the right. This is inherently incorrect since probing variations will cause differences in the measured parameters on the left and right. One can verify the correctness of neglecting this effect by looking at the difference in S_{11} and S_{22}. In the remaining part of the routine port one will be assumed to be exactly the same as port two. A new set of parameters will be introduced. The reflection, T_r, and transmission, T_t, of the through and the reflection, D_r, and transmission, D_t, of the delay. The parameters are obtained from the measured S-parameters by averaging the parameters from both ports.

Next some variables are introduced to speed up calculation by replacing frequently used parameter combinations. The second advantage of this approach is that the resulting formulas remain relatively small. T_{add} represents $S_{Tr} + S_{Tr}$ while T_{sub} equals S_{Tr}-S_{Tt}, D_{add} and D_{sub} perform the same function for the delay. Finally C_{sub} equals S_{Tr}-S_{Dr} and C_{mul} represents $S_{Tr}S_{Dr}$.

Starting top down the expression for S_{11} will be examined first. S_{11} is the smallest solution of a quadratic equation,[B.14]. Rewriting this formula yields an expression in the terms defined previously:

$$X = \frac{T_{add} * T_{sub} - D_{add} * D_{sub} \pm \sqrt{(D_{add} - T_{add})(T_{sub} - D_{sub})(D_{add} - T_{sub})(T_{add} - D_{sub})}}{2C_{sub}} \qquad [B.34]$$

Rewriting [B.32] yields the new formula for S_{22}.

$$S_{22} = \frac{S_{Tr} - S_{11}}{S_{Tt}} \qquad [B.35]$$

The next step is to rewrite [B.33], which leads to the formula below.

$$S_{12} = S_{21} = \pm \frac{\sqrt{(D_{add} - T_{add})(T_{sub} - D_{sub})(D_{add} - T_{sub})(T_{add} - D_{sub})}}{C_{sub}} \qquad [B.36]$$

Finally the extraction of gamma has to be rewritten starting from [B.17], this results in the formula below.

$$\gamma = \frac{1}{2l} \ln \left(\frac{G_a + (C_{mul} - T_{add} * T_{sub})\dfrac{P_{11A}}{P_{21A}}}{S_{Tr}D_{add}D_{sub} - S_{Dr}T_{add}T_{sub} + (C_{mul} - D_{add}D_{sub})\dfrac{P_{11A}}{P_{21A}}} \right) \qquad [B.37]$$

where

$$G_a = \frac{(T_{add} * T_{sub} - D_{add} * D_{sub})^2 - (D_{add} - T_{add})(T_{sub} - D_{sub})(D_{add} - T_{sub})(T_{add} - D_{sub})}{4C_{sub}} \qquad [B.38]$$

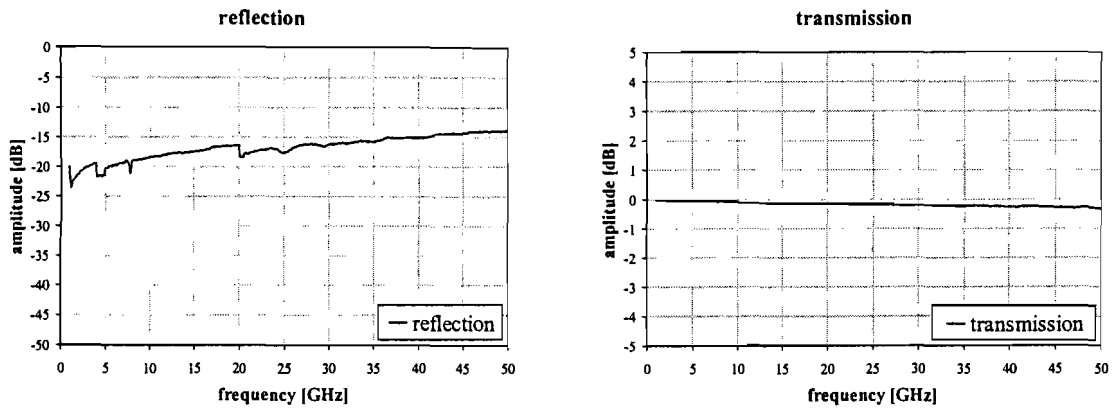With these adjustments the LRL algorithm produces acceptable results.

Figure B.3 Pad structure extracted using the optimised LRL algorithm.

The difference compared to the original LRL algorithm is clearly visible, while the curves show more likely behaviour they can still be erroneous, this check will be presented in the next section. The pictures below present the curves of the optimised (LRLe) algorithm.
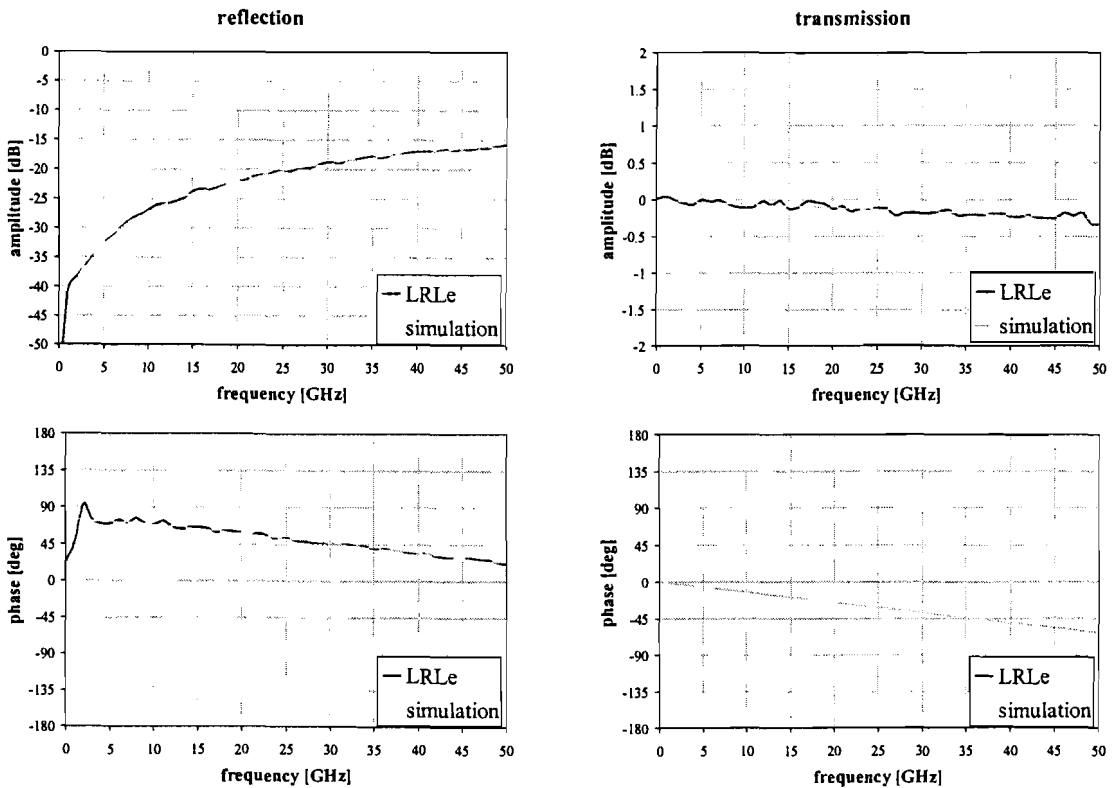

Figure B.4 Error propagation through the optimised LRL algorithm.

The pictures shows how a distortion of 5 percent on the input signal result in a distortion on the output signal, however the distortion is significantly lower than that produced by the original LRL algorithm.

B.1.4 Correctness verification

Before the adapted LRL algorithm can be accepted for use in later modelling schemes, the correctness of the algorithm has to be tested. In order to test the correctness of the algorithm a simple simulation was performed which yields the scattering parameter data of a single pad structure. The pad structure data is than cascaded to form a single through structure. Since the reference impedance at both side of the pad structure was 50 ohms, a second simulation of a delay line cannot be used. The delay line was approximated by a purely imaginary propagation constant, cascaded with the simulated pad structures. If these elements are used as input for the LRL algorithm the input and output data of the algorithm can be verified. The result of this test is presented in the pictures below:
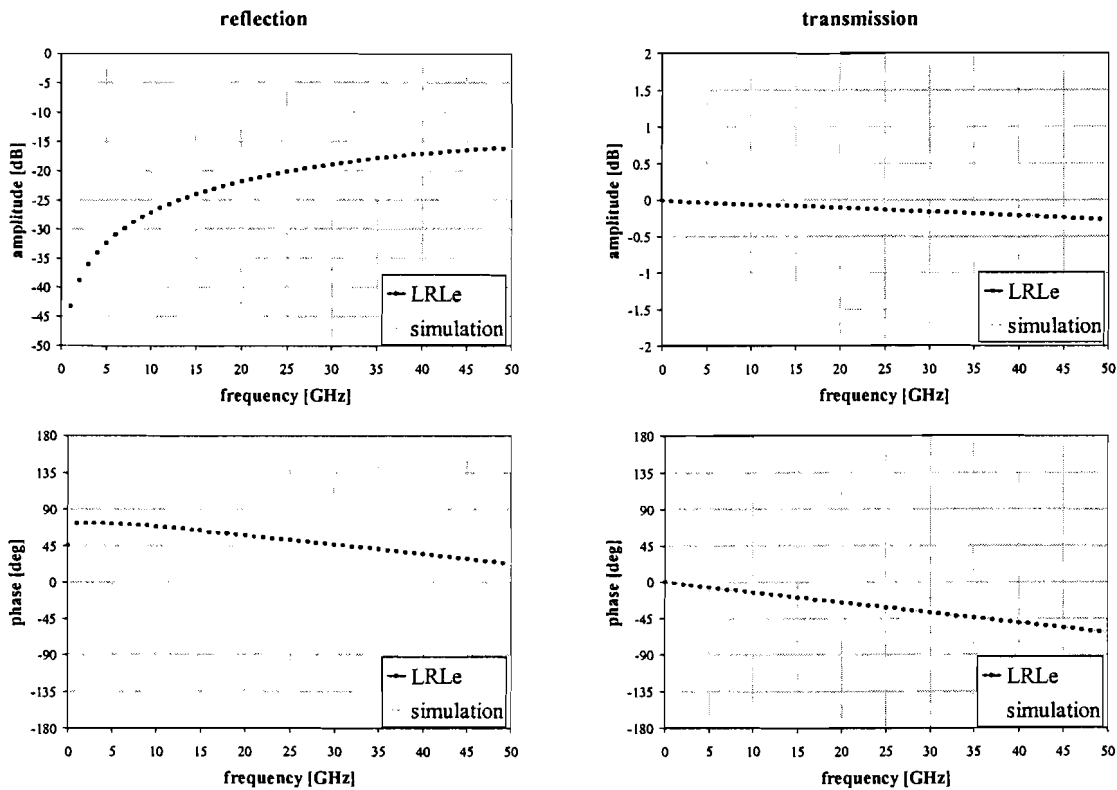
Figure B.5 Input and output of the LRL algorithm used to test the implementation.

The figures above show that the extracted pad structure tightly resembles the original pad structure, which indicates that the LRL algorithm was implemented correctly.
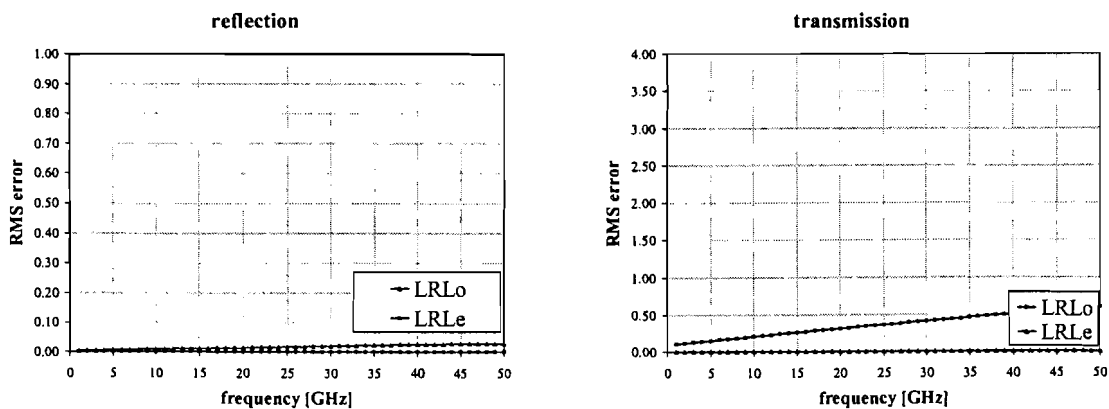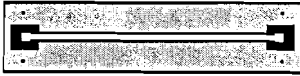

Figure B.6 Error propagation through the original and optimised LRL algorithm.

B.2 BCL extraction routine

B.2.1 BCL algorithm

Where the general TSD or LRL approaches use scattering and wave cascading parameter matrices to calculate the error circuits ABCD and Y and Z parameters could also be used. This has some advantages over using scattering and wave cascading parameters. This method will be referred to with the abbreviation BCL.

The first step is to define the structures necessary for this de-embedding scheme.

structure	scheme	measurement	theoretical matrix	
through		$\begin{bmatrix} S_{Tr} & S_{Tt} \\ S_{Tt} & S_{Tr} \end{bmatrix}$	$[M_{through}] = [A_{pad}][A_{pad}]$	[B.39]
line		$\begin{bmatrix} S_{Dr} & S_{Dt} \\ S_{Dt} & S_{Dr} \end{bmatrix}$	$[M_{lineA}] = [A_{pad}][A_{lineA}][A_{pad}]$	[B.40]

Where the matrices $[M_{through}]$, $[M_{lineA}]$ and $[M_{lineB}]$ represent the measured ABCD parameters of the de-embedding structures. The matrices $[A_{pad}]$ and $[A_{pad}]^{-1}$ represent the theoretical ABCD parameters of the pad structure cascading from left to right and from right to left respectively. Finally the matrix $[A_{lineX}]$ represents the theoretical ABCD parameters of the line segment.

From literature one can find expressions for the ABCD parameters of a lossy transmission line:

$$[A_{lineX}] = \begin{bmatrix} \cosh(\gamma 1_x) & Z_{line} \sinh(\gamma 1_x) \\ Y_{line} \sinh(\gamma 1_x) & \cosh(\gamma 1_x) \end{bmatrix} \qquad [B.41]$$

Again the assumption that the pad structure may be represented by a reciprocal circuit is used to simplify the problem. An expression for the pad structure can be found which has three unknown elements, since any reciprocal circuit can be represented by an equivalent circuit as depicted below.
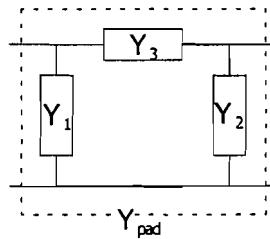

Figure B.7 Representation of the pi-network of a reciprocal circuit.

Using this equivalent circuit the ABCD parameters of the pad structure in terms of the three admittances Y1, Y2 and Y3 from the equivalent circuit now become:

$$[A_{pad}] = \frac{1}{Y_3} \begin{bmatrix} Y_2 + Y_3 & 1 \\ (Y_2 + Y_3)(Y_1 + Y_3) - Y_3^2 & Y_1 + Y_3 \end{bmatrix} \qquad [B.42]$$

The first step in the parameter extraction follows directly from the through measurement by combining [B.39] and [B.42] a matrix relation is obtained, which describes measured through behaviour [B.43]. To simplify the problem the measured matrix of the through will be redefined as shown below in [B.44]:

$$\left[A_{through}\right] = \frac{1}{Y_3^2}\begin{bmatrix} 2(Y_2+Y_3)(Y_1+Y_3)-Y_3^2 & 2(Y_2+Y_3) \\ 2(Y_1+Y_3)((Y_2+Y_3)(Y_1+Y_3)-Y_3^2) & 2(Y_2+Y_3)(Y_1+Y_3)-Y_3^2 \end{bmatrix} \qquad \text{[B.43]}$$

$$\left[M_{through}\right] = \begin{bmatrix} T_0 & T_1 \\ T_2 & T_0 \end{bmatrix} \qquad \text{[B.44]}$$

By combining [B.43] and [B.44] expressions for Y_1 and Y_2 in relation to Y_3 are obtained:

$$Y_1 = \frac{T_0+1}{T_1} - Y_3 \qquad \text{[B.45]}$$

$$Y_2 = \tfrac{1}{2}T_1Y_3^2 - Y_3 \qquad \text{[B.46]}$$

The equation obtained from T_2 will not yield any new information since it is a function of T_1 and T_0. Due to the symmetry of the problem, each measurement yields at most two independent equations.

$$T_2 = \frac{T_0^2-1}{T_1} \qquad \text{[B.47]}$$

Using these relations the ABCD matrix of the pad structure can be rewritten to a function of Y_3:

$$\left[A_{pad}\right] = \frac{1}{Y_3}\begin{bmatrix} \tfrac{1}{2}T_1Y_3^2 & 1 \\ \tfrac{1}{2}(T_0-1)Y_3^2 & \dfrac{T_0+1}{T_1} \end{bmatrix} \qquad \text{[B.48]}$$

By combining [B.39] with [B.40] one can eliminate [A_{pad}] from the remaining equations.

$$\left[M_{delay}\right] = \left[A_{pad}\right]\left[A_{line}\right]\left[A_{pad}\right]^{-1}\cdot\left[M_{through}\right] \qquad \text{[B.49]}$$

$$\left[M_{dt}\right]\left[A_{pad}\right] = \left[A_{pad}\right]\left[A_{line}\right] \qquad \text{[B.50]}$$

with

$$\left[M_{dt}\right] = \left[M_{delay}\right]\left[M_{through}\right]^{-1} = \begin{bmatrix} D_{11} & D_{12} \\ D_{21} & D_{22} \end{bmatrix} \qquad \text{[B.51]}$$

The next step is to write [B.50] in to its separate term so the final relations can be exposed. The additional line length, next to the zero-length through line, yields one independent equation for Y_3 as a function of Z_0.

$$\gamma = \frac{\operatorname{acosh}(G_0)}{l_{delay}}$$

[B.52]

$$Z_0 = \frac{\frac{1}{2}T_1 D_{11} + \frac{1}{2}(T_0 - 1)D_{21} - \frac{1}{2}T_1 G_0}{\sqrt{G_0^2 - 1}} Y_3^2$$

[B.53]

with

$$G_0 = \cosh(\gamma\, l_{delay}) = \frac{1}{2}(T_0 + 1)D_{11} - \frac{1}{2}(T_0 - 1)D_{22} + \frac{1}{2}D_{12}T_2 - D_{21}T_1$$

[B.54]

$$\sinh(\operatorname{acosh}(x)) = \sqrt{x-1}\sqrt{x+1} = \sqrt{x^2 - 1}$$

[B.55]

Again one unknown has been solved and one unknown has been expressed in Y_3, this means we either need an estimate for one of the unknowns or a measurement, which yields independent equations.

At this point the main advantage of this method becomes apparent, all methods using S-matrices or T-matrices are able to solve S_{11}, S_{12}, S_{21} and S_{22} of the pad structure. Although this seems to solve the problem one major issue can easily be forgotten. The extracted S-parameters are referenced to the 50 Ω impedance of the measurement system, while the reference impedance at the new reference-plane should have been the impedance of the transmission line in-between. Since this impedance has not and cannot be solved from the S-parameter measurements the solution is not complete and an alternative approach has to be used to solve the line impedance so the extracted S-parameters can be adjusted. The BCL algorithm suggested here includes the line impedance in the calculation, so no error can be made on that part.

It is important to realise that including a perfect short-circuit wouldn't yield new independent equations since an ideal short-circuit, in combination with [B.46], should yield:

$$Y_{short} = Y_3 + Y_1 = \frac{T_0 + 1}{T_1}$$

[B.56]

A perfect open-circuit wouldn't yield any new independent relation either since it again can be derived from the measured S-parameter data:

$$Y_{open} = \frac{(Y_1 + Y_3)(Y_2 + Y_3) - Y_3^2}{Y_2 + Y_3} = \frac{T_0 - 1}{T_1}$$

[B.57]

Another line length would yield an equation resembling [B.50] and will not yield independent equations, since the only change should be the length, l_{delay},, which is a known factor. This means we're not able to extract the missing unknown element directly from the measurement and Z_0 still needs to be determined.

B.2.2 Optimisation of the computational efficiency

Again the algorithm was implemented directly into MATLAB and then the expressions were rewritten into functions of the measured scattering parameters, the output of this technique is shown below.
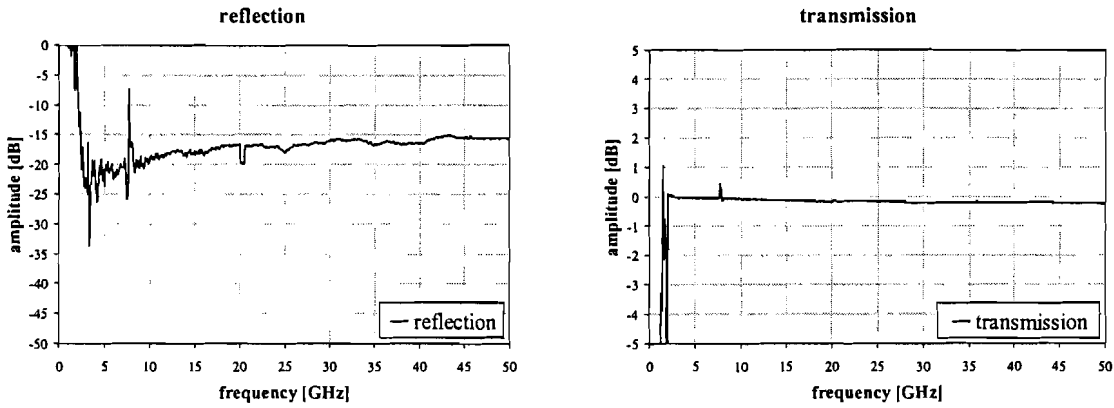

Figure B.8 Pad structure extracted using the BCL algorithm.

It is important to notice that this basic routine produces accurate data for the transmission coefficients but the reflection coefficients show behaviour that cannot be used for de-embedding purposes. The graphs below present the numerical stability of the original algorithm (BCLo).
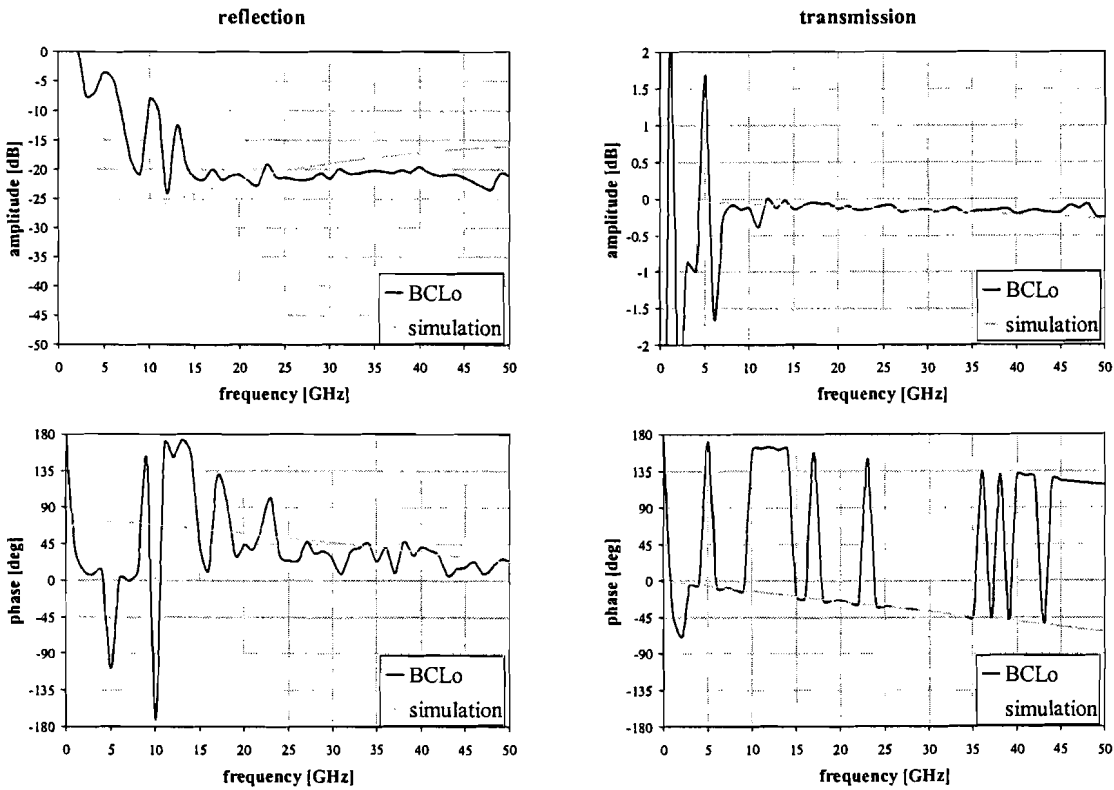
Figure B.9 Error propagation through the BCL algorithm.

The pictures shows how a distortion of 5 percent on the input signal result in a much larger distortion on the output signal, indicating that this algorithm would probably not result in reliable output data.

The first formula that will be optimised is [B.55] this results in the formula shown below:

$$G_0 = \frac{1}{2}\left(\frac{S_{Tt}}{S_{Dt}} + \frac{S_{Dt}}{S_{Tt}} - \frac{C_{sub}}{S_{Tt}S_{Dt}}\right)$$

[B.58]

The phase of G_0 needs to be adjusted such that the γ extracted from G_0 shows smooth behaviour, no further optimisation has been done for γ since the original method already shows acceptable performance.

Next Y_3 is optimised from [B.53] using a 50 Ohms characteristic impedance, this is done so that compatibility with the LRL routine that was previously discussed is preserved.

$$Y_3 = 2\sqrt{\frac{S_{Dt}S_{Tt}\sqrt{G_0^2 - 1}}{(T_{sub} + 1)(T_{add} - D_{add}D_{sub} + S_{Dr}(T_{add} - 1)) - S_{Dt}G_0(1 + 2S_{Tr} - T_{add}T_{sub})}}$$

[B.59]

Next optimised equations for Y2 and Y1 can be derived from [B.45] and [B.46] resulting in:

$$Y_1 = \frac{1 + 2S_{Tt} - T_{add}T_{sub}}{1 + 2S_{Tr} + T_{add}T_{sub}} - Y_3$$

[B.60]

$$Y_2 = \frac{1 + 2S_{Tr} + T_{add}T_{sub}}{4S_{Tt}}Y_3^2 - Y_3$$

[B.61]

Now all admittance parameters have been extracted, the admittance parameters need to be transformed to scattering parameters so they can be compared with the adapted LRL method, or they have to be transformed to wave cascading parameters so they can be used to de-embed a measurement.

The transformation between Y-parameters and S-parameters can be optimised using:

$$S_{11} = \frac{T_a(1 + T_s)^2 Y_3^2 + 4S_{Tt}T_s}{(1 + T_s)^2 Y_3^2 + 4S_{Tt}}$$

[B.62]

$$S_{22} = -\frac{(1 + 2T_s + T_s^2)Y_3^2 - 4S_{Tt}}{(1 + 2T_s + T_s^2)Y_3^2 + 4S_{Tt}}$$

[B.63]

$$S_{12} = S_{21} = \frac{4S_{Tt}(1 + T_s)Y_3}{(1 + T_s)^2 Y_3^2 + 4S_{Tt}}$$

[B.64]

No direct improvement can be achieved from this point, the resulting output still causes instabilities for certain structures as can be seen in the figures below.
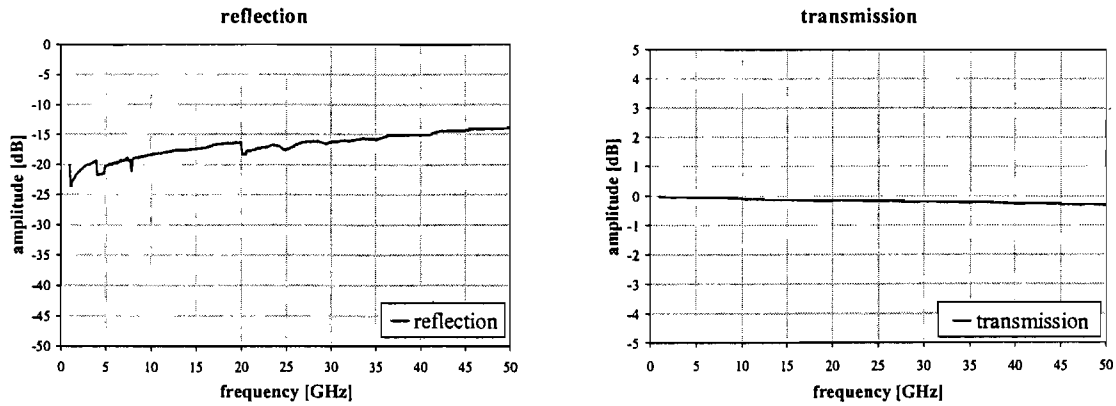
Figure B.10 Pad structure extracted using the optimised BCL algorithm.

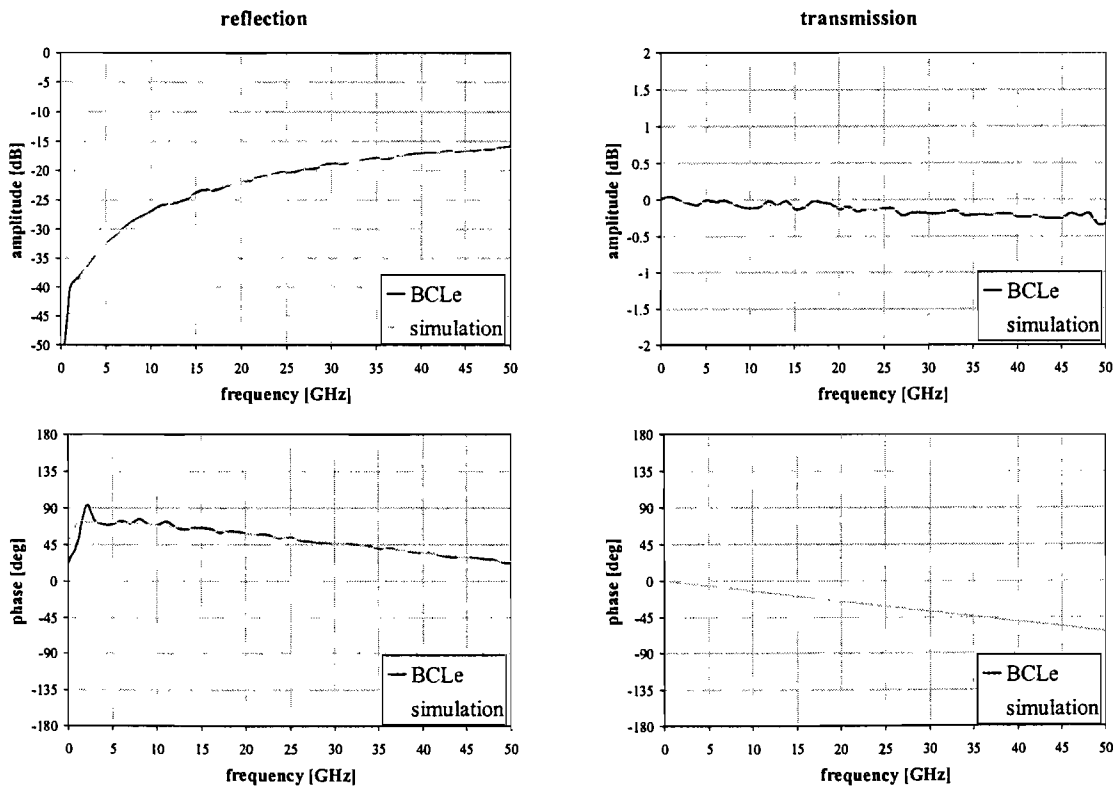The curves of the optimised BCL algorithm (BCLe) are presented below:

Figure B.11 Error propagation through the optimised BCL algorithm.

The pictures shows how a distortion of 5 percent on the input signal result in a distortion on the output signal, however the distortion is significantly lower than that produced by the original LRL algorithm.

B.2.3 Correctness verification

Again the correctness of the algorithm needs to checked, this has been done using the same method as was used to verify the BCL algorithm, the results are shown below:
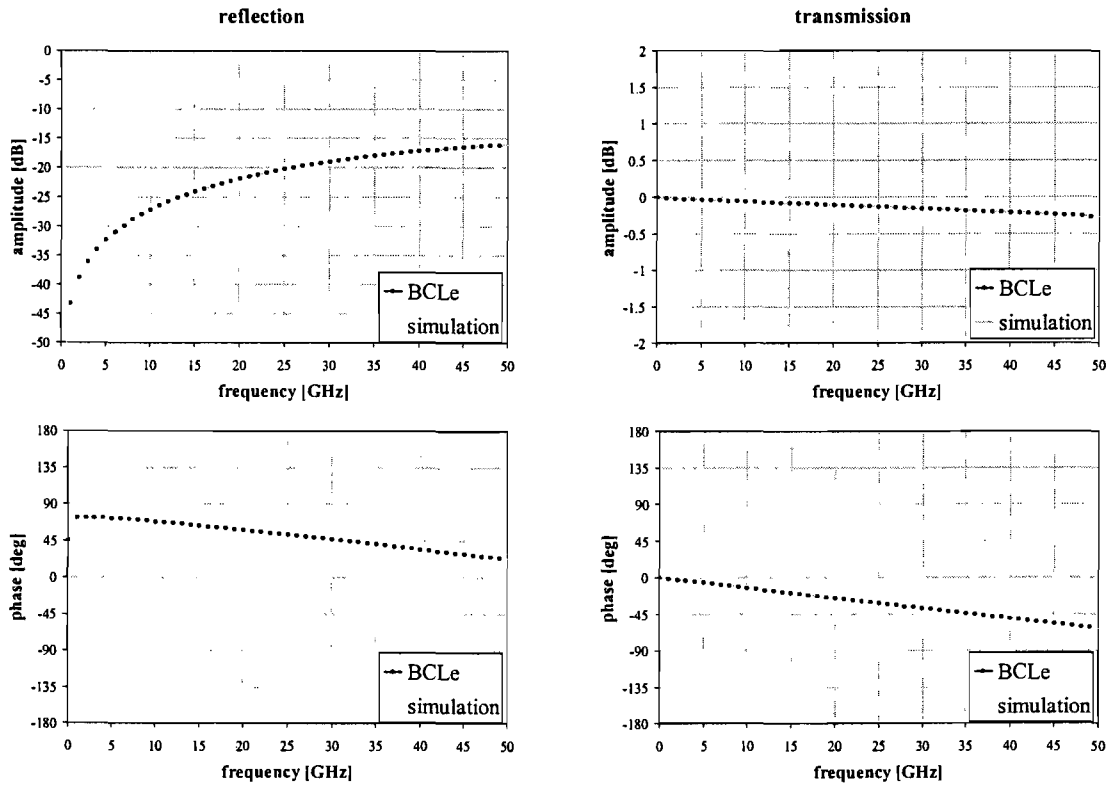
Figure B.12 Input and output of the BCL algorithm used to test the implementation.

The figures above show that the extracted pad structure tightly resembles the original pad structure, which indicates that the BCL algorithm was implemented correctly.

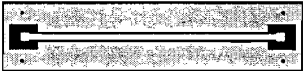Again the analyses of measurement uncertainty versus error propagation have been performed:
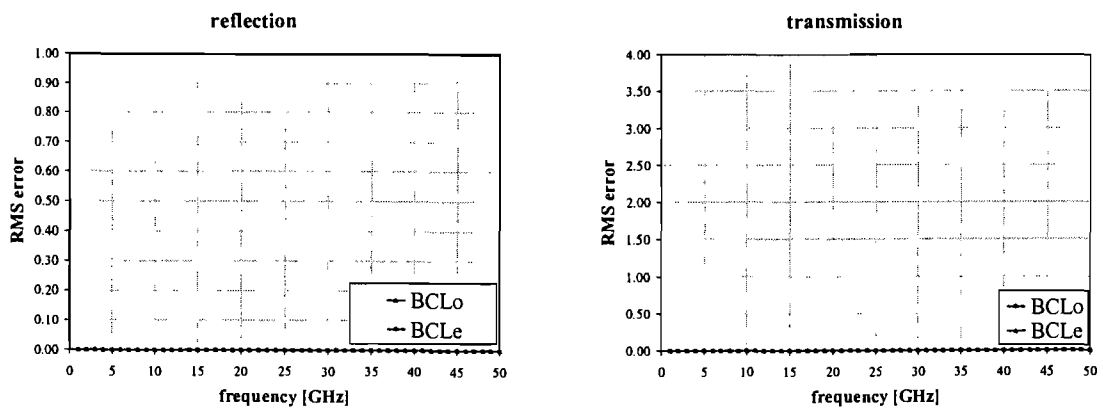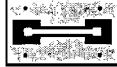
Figure B.13 Error propagation through the original and optimised BCL algorithm.

B.3 TSD extraction routine

B.3.1 TSD algorithm

The third method that was tested is the TSD method, it uses the same set of standards as were defined for the LRL method. The only significant difference between the two methods is the mathematical approach towards the problem. It should be noted that the TSD method is known to have stability problems.

Structure   scheme   Measurement   Theoretical matrix

Through

$$\begin{bmatrix} S_{T11} & S_{T12} \\ S_{T21} & S_{T22} \end{bmatrix}$$

$$\left[M_{through} \right] = \left[T_{pad} \right] \left[T_{pad} \right]$$ [B.65]

line A

$$\begin{bmatrix} S_{D11} & S_{D12} \\ S_{D21} & S_{D22} \end{bmatrix}$$

$$\left[M_{line} \right] = \left[T_{pad} \right] \left[T_{lineA} \right] \left[T_{pad} \right]$$ [B.66]

Reflect

$$\begin{bmatrix} S_{RA} & 0 \\ 0 & S_{RB} \end{bmatrix}$$

$$S_{Rx} = S_{11} - \frac{S_{12} S_{21}}{1 + S_{22}}$$ [B.67]

The routine start by defining two supporting matrices:

$$H = M_{through} M_{line}^{-1}$$ [B.68]

$$K = M_{line}^{-1} M_{through}$$ [B.69]

Where H eliminates the right pad structure and K eliminates the left pad structure, In the remainder of this chapter only the mathematics for the left pad structure will be presented since the left and right pad should be practically identical. Next an additional set of equations is derived from these matrices:

$$R = \frac{1}{\sqrt{(H_{11} + H_{22})^2 - 4}}$$ [B.70]

$$H_1 = \tfrac{1}{2}\left(R(H_{22} - H_{11}) + 1\right)$$ [B.71]

$$H_2 = \tfrac{1}{2}\left(R(H_{22} - H_{11}) - 1\right)$$ [B.72]

$$H_3 = RH_{12}$$ [B.73]

$$H_4 = -RH_{21}$$ [B.74]

where

$$R = \frac{1}{\sqrt{\left(e^{\gamma l} - e^{-\gamma l}\right)^2}}$$ [B.75]

From this set of equations two pad structure scattering parameters can be derived. The first solution is obtained using the equations presented below:

$$S_{11} = \frac{H_2}{H_4} = \frac{H_3}{H_1}$$ [B.76]

$$S_{22} = \frac{S_{11} - S_{RA}}{S_{RA} - \frac{H_1}{H_4}}$$ [B.77]

$$S_{12} = S_{21} = \pm \sqrt{-\frac{1}{H_4} S_{22}}$$ [B.78]

$$\det(S) = \frac{H_1}{H_4} S_{22}$$ [B.79]

While the second uses the set of equations

$$S_{11} = \frac{H_1}{H_4} = \frac{H_3}{H_2}$$ [B.80]

$$S_{22} = \frac{S_{RA} - S_{11}}{\frac{H_1}{H_4} - S_{RA}}$$ [B.81]

$$S_{12} = S_{21} = \pm \sqrt{\frac{1}{H_4} S_{22}}$$ [B.82]

$$\det(S) = \frac{H_2}{H_4} S_{22}$$ [B.83]

After this the through structure is calculated using both solutions, using the equations below:

$$T_{11} = \frac{1}{S_{12}^2 S_{T21}} \left(S_{11} S_{T22} - \det(S_T) + (S_{T11} - S_{11}) S_{22} \right)$$ [B.84]

$$T_{22} = -\frac{1}{S_{12}^2 S_{T21}} \left(S_{11} \left(S_{T22} \det(S) - S_{22} \det(S_T) \right) - \det(S_T)(S_{T11} S_{22} - \det(S)) \right)$$ [B.85]

Since the through will be very short, the imaginary part of T_{22}/T_{11}, which equals $e^{2\gamma l}$, should always be positive, this test will rule out one of the two solutions.

B.3.2 Optimisation of the computational efficiency

Again the numerical stability was optimised by implementing the basic algorithm directly into MATLAB and then rewriting the expressions into functions of the measured scattering parameters. The output of this technique prior to optimisation is shown below.
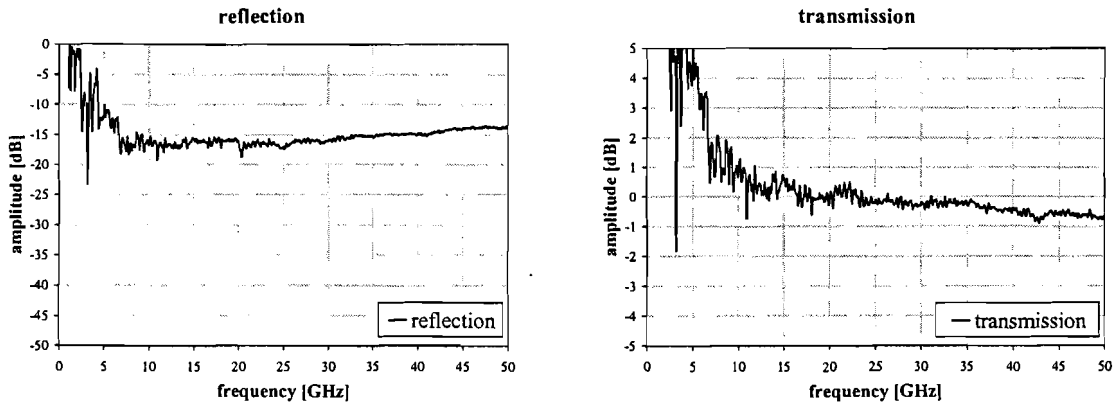

Figure B.14 Pad structure extracted using the TSD algorithm.

As the plot clearly illustrates, the results produced by the original TSD algorithm has a serious problem with calculation accuracy. The results are not useful for de-embedding purposes. The graphs below present the numerical stability of the original algorithm (TSDo).
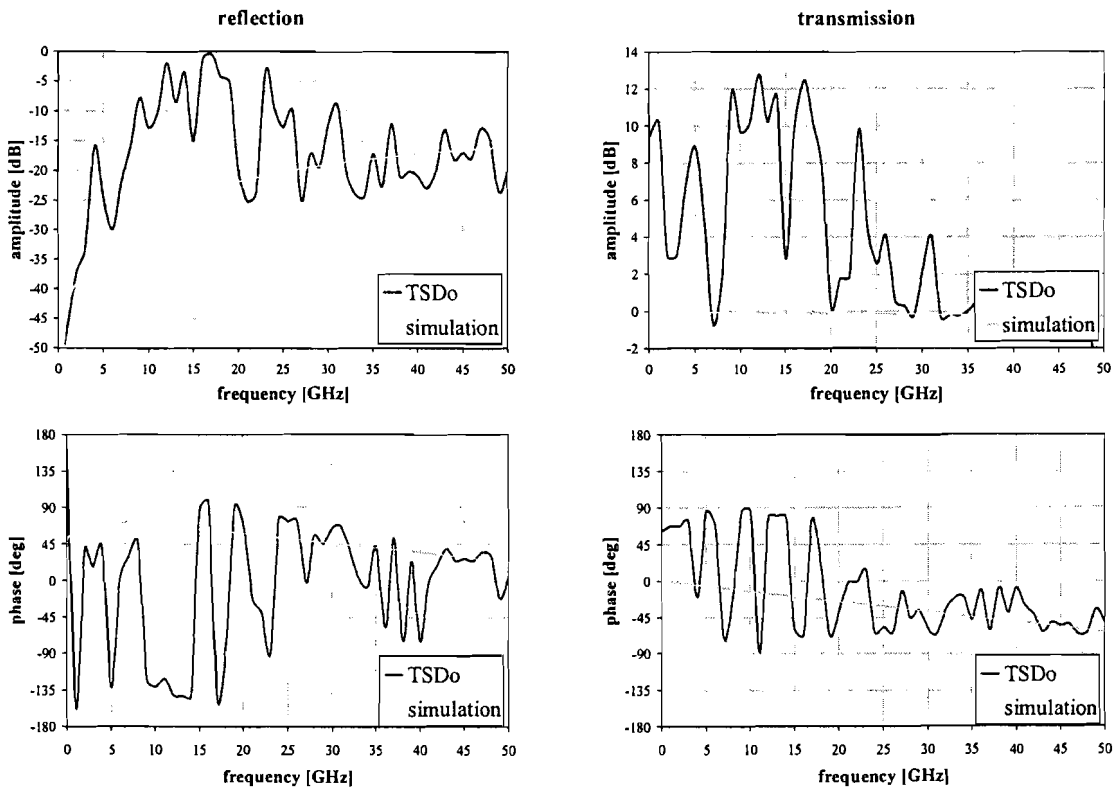

Figure B.15 Error propagation through the TSD algorithm.

The pictures shows how a distortion of 5 percent on the input signal result in a much larger distortion on the output signal, indicating that this algorithm would probably not result in reliable output data.

Relatively few alterations have been made to the original routine, it has to be noted that the optimisation of S_{22} results in exactly the same formula, since the same assumptions have been made.

The only optimisations are done in the definition of the variables H1, H2 and H4.

$$H_1 = \frac{S_{Tt}^2 - S_{Dt}^2 + S_{Dr}^2 - S_{Tr}^2}{2\sqrt{\left(2 * S_{Tr}S_{Dr} + S_{Tt}^2 - S_{Tr}^2 + S_{Dt}^2 - S_{Dr}^2\right)^2 - 4S_{Tt}^2 S_{Dt}^2}} + \frac{1}{2}$$ [B.86]

$$H_2 = \frac{S_{Tt}^2 - S_{Dt}^2 + S_{Dr}^2 - S_{Tr}^2}{2\sqrt{\left(2 * S_{Tr}S_{Dr} + S_{Tt}^2 - S_{Tr}^2 + S_{Dt}^2 - S_{Dr}^2\right)^2 - 4S_{Tt}^2 S_{Dt}^2}} - \frac{1}{2}$$ [B.87]

$$H_4 = \frac{S_{Dr} - S_{Tr}}{\sqrt{\left(2 * S_{Tr}S_{Dr} + S_{Tt}^2 - S_{Tr}^2 + S_{Dt}^2 - S_{Dr}^2\right)^2 - 4S_{Tt}^2 S_{Dt}^2}}$$ [B.88]

Next to this set of optimisations the assumption that the left and right pad structures are identical results in the simple formula for S_{22} as was presented for the LRL method. After these modifications the TSD (TSDe) algorithm produces the curves on this page. The extracted pad structure curves tightly resemble the curves extracted using the LRL algorithm.
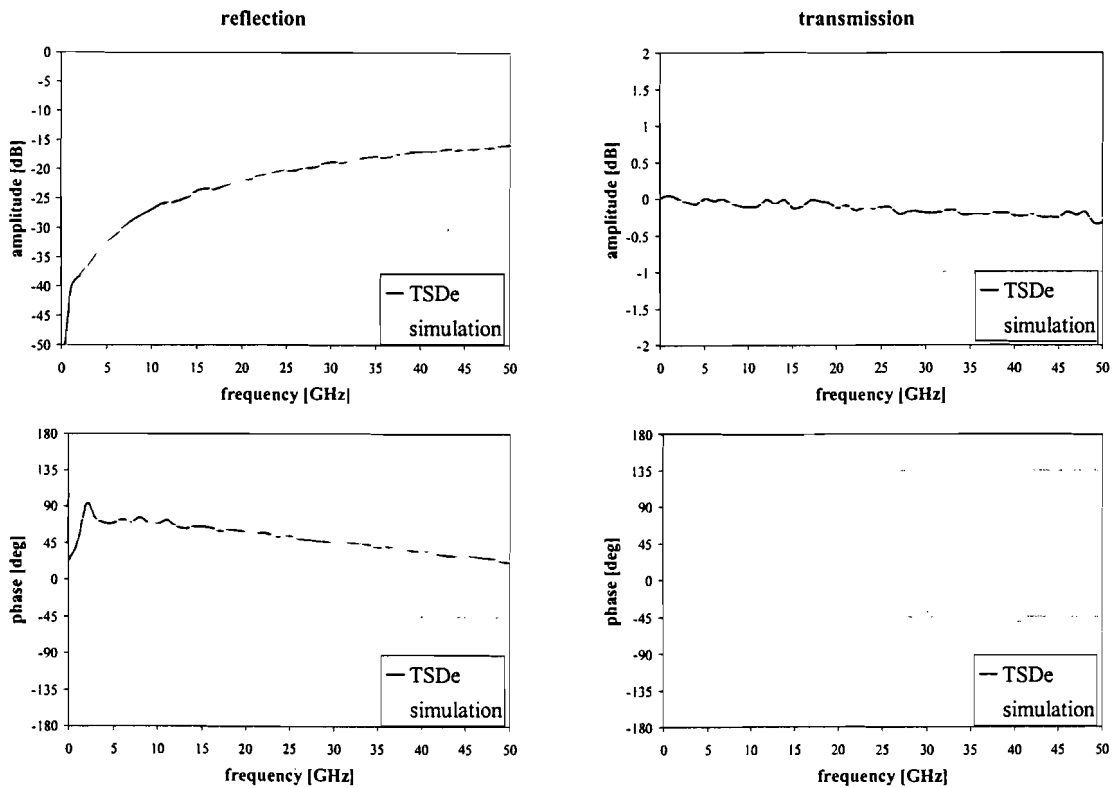

Figure B.16 Error propagation through the optimised TSD algorithm..

Again the results from the numerical accuracy routine described in is presented below the extracted pad structure S-parameter data, the curves show the optimised routine out-performs the original routine. Also the curves show the same behaviour as was obtained using the previously described algorithms.

B.3.3 Correctness verification

Again the correctness of the algorithm needs to checked, this has been done using the same method as was used to verify the optimised TSD algorithm, the results are shown below:
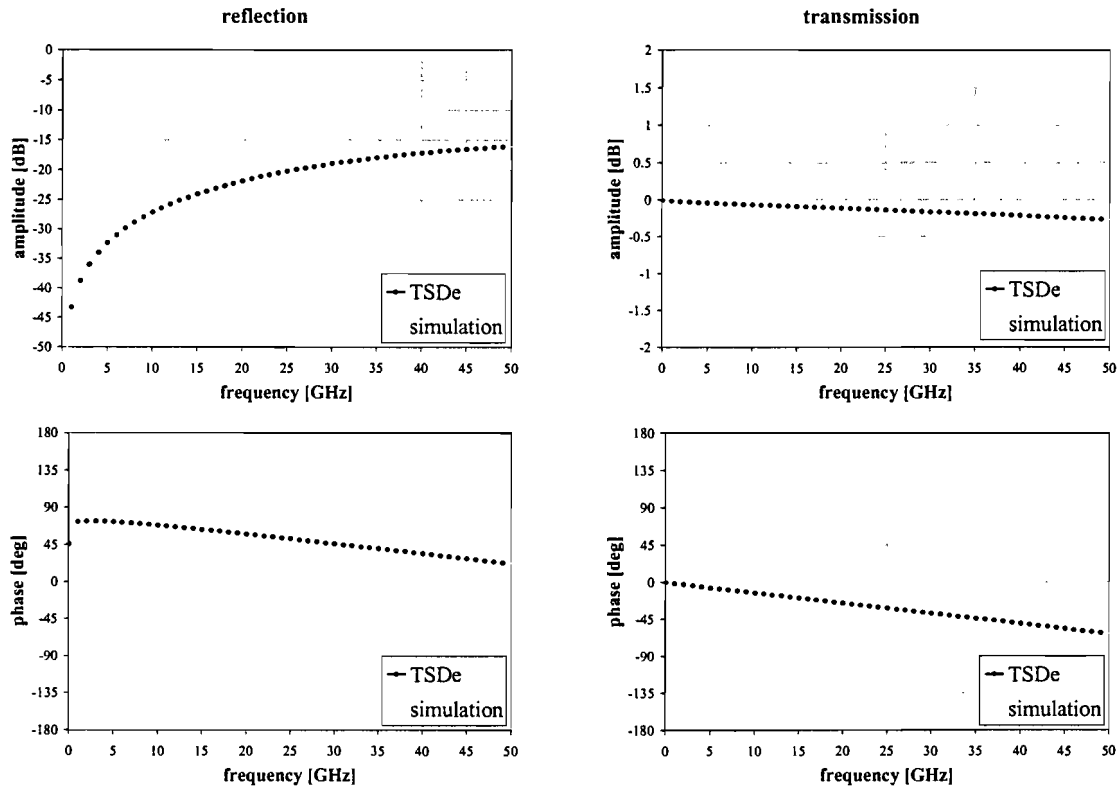

Figure B.17 Input and output of the TSD algorithm used to test the implementation.

The figures above show that the extracted pad structure tightly resembles the original pad structure, which indicates that the optimised TSD algorithm was implemented correctly. Again the analyses of measurement uncertainty versus error propagation have been performed, the error introduced by averaging ports one and two is subtracted from the simulation results:
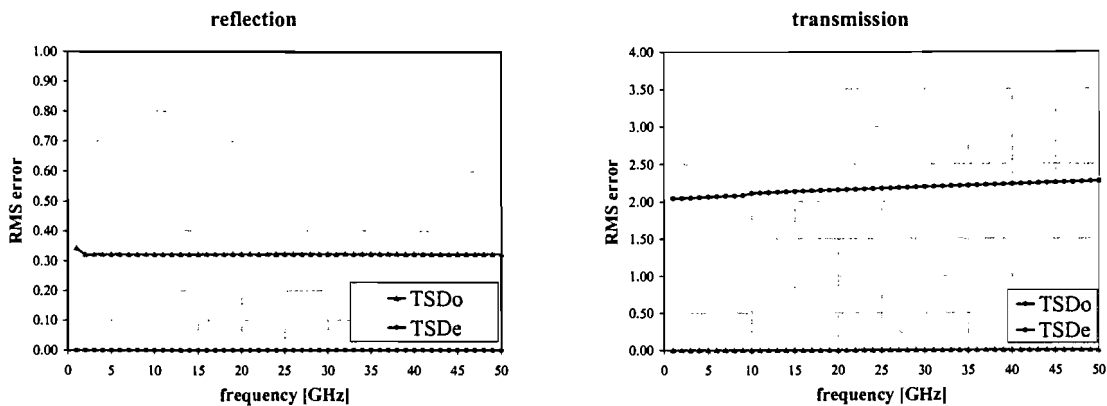

Figure B.18 Error propagation through the original and optimised TSD algorithm.